

Azimuthal Angular Description of Jet Quenching at High p_T

Master's Thesis
by
Vytautas Vislavičius

Supervisor:
Peter Christiansen



LUND
UNIVERSITY

DEPARTMENT OF PHYSICS
LUND, 2013

Populärvetenskaplig sammanfattning

Vanligen beskrivs universums ursprung genom den så kallade Big Bang-teorin. Man skall emellertid inte förstå detta som en stor, kraftig explosion i rymden, eftersom varken rum eller tid existerade innan Big Bang. Även om frågan om vad som orsakade Big Bang inte har besvarats, pekar observation på att allt inkluderande galaxer, stjärnor och planeter, ja även rumtiden själv har sitt ursprung i en enda punkt. Denna punkt var mindre än en atomkärna, men ändå oändligt het och tät. Av okänd anledning började denna lilla punkt expandera: rummet sträcktes ut snabbare än ljushastigheten och tog materien med sig. Expansionen var så kraftig att volymen fördubblades var 10^{-24} sekund innan expansionen bromsades in till vad som kan observeras idag.

Det nyfödda universum var så hett och tätt att ingen normal materia varken atomkärnor eller nukleoner kunde existera. Istället var materiens beståndsdelar kvarkar och gluoner och detta materietillstånd kallas ett kvark-gluon plasma (QGP). Materien fortsatte att expandera samtidigt som den avkyldes. Det är fortfarande bara en filosofisk fråga huruvida den fundamentala växelverkan i denna materia - vilket i huvudsak är den starka kraften av en ren slump råkar ha precis de egenskaper som den har. Emellertid blev kraften mellan plasmans beståndsdelar större i takt med avkyllningen och till sist bildades de första nukleonerna, dvs. protoner och neutroner.

Så småningom slogs nukleonerna ihop och bildade atomer som i sin tur bildade ännu större strukturer och slutligen bildades stjärnor och planeter. Den första stjärnan bildades ungefär 380000 år efter Big Bang. Vad har hänt sedan dess? Ungefär 13,7 miljarder år av slump och evolution, både på universellt och biologiskt plan, har lett fram till en varm och skön planet som vi kallar Jorden, med bakterier, dinosaurier och slutligen mänskiskor.

Idag har utvecklingen inom både teknologi och metodologi gjort det möjligt för oss att se allt längre tillbaks i tiden och därmed tillbaka i universums historia. Kosmologiska observationer är begränsade bakåt till den tid då den första strålningen uppstod, men teoretiska modeller går mycket längre tillbaka än så. I själva verket visar upptäckter under de senaste 50 åren att ett QGP kan skapas i laboratoriet genom att låta tunga atomkärnor kollidera med varandra vid mycket höga kollisionsenergier. Med andra ord, med de verktyg vi har till vårt förfogande idag kan man återskapa den materia som fanns i universum bråkdelar av en sekund efter Big Bang.

Att skapa ett QGP är en sak. Att förstå hur universum utvecklades är en annan och för att förstå detta måste denna återskapade materien analyseras noggrant. Detta är lättare sagt än gjort expansionen och avkyllningen av det skapade QGP sker så snabbt, att det inte finns något sätt att observera vad som händer under det korta ögonblick QGP existerar. Den enda möjlighet man har att studera processen är genom att mäta på den materia som finns i slutstadiet, dvs. de producerade partiklarna och deras energier. Dessutom finns det inget trivialt sätt att från topologin hos en kollision få information om egenskaperna hos det ursprungligen skapade materietillståndet. Därför räcker det inte ett rekonstruera kollisionen utan man måste dessutom använda en del av dessa partiklar som testpartiklar som undersökt plasmat.

I min avhandling kommer jag att visa att det finns ett enkelt, men också effektivt, sätt att, genom att relatera två mikroskopiska kvantiteter med varandra, få ett begrepp om hur QGP expanderar. Jag kommer också att呈现出 en ganska naiv uppskattning av det troligtvis dominerande sätt på vilket partiklarna förlorar energi genom gluon-strålning vid passagen genom plasmat. Detta bör, om inte annat, kunna vara en god grund för vidare forskning inom detta område.

Acknowledgements

First of all, I would like to thank my supervisor Peter Christiansen for proposing the idea and guiding me through all the work I have done. I would also like to thank Konrad Tywoniuk for crucial theoretical discussions, Anders Oskarsson and Evert Stenlund for their excellent feedback.

I am very grateful to my dearest colleagues Tuva Richert, Martin Ljunggren and Carsten Søgaard not only for helping me with the technical difficulties, but also for being the most amazing people I have ever worked with.

Last, but not the least, I would like to say a big thank you to all the people in Lund Physics department for making my stay here a remarkable experience never to be forgotten. There are no words to express how much I appreciate you all!

Vytautas

Contents

1	Introduction	2
1.1	Aim of the Study	2
1.2	Layout of the Thesis	2
2	Standard Model and Quantum Chromodynamics	4
2.1	Lepton sector	4
2.2	Quark sector	6
2.3	Gauge bosons	7
2.4	Quantum Chromodynamics	8
3	Detectors	10
3.1	ATLAS	10
3.2	ALICE	13
4	Heavy Ion Collisions	16
4.1	Quark Gluon Plasma	16
4.2	Nuclear Modification Factor R_{AA}	17
4.3	Flow	18
4.4	Jet Quenching	24
4.5	In- and out-of-plane nuclear modification factors	24
4.6	Energy loss	25
4.7	QGP density	28
5	Glauber Model	30
6	Analysis	32
6.1	Glauber Monte Carlo	32
6.2	Combining v_2 and R_{AA}	38
6.3	Density Effects	38
6.4	From R_{AA} to energy-loss and back	42
6.5	Rescaling to Gold-Gold collisions at RHIC	43
7	Results	45
8	Discussion	57
9	Conclusions	58
A	Summary of Terms and Acronyms	62
B	Impact parameter, $\langle N_{part} \rangle$ and $\langle N_{bin} \rangle$ results from my Glauber Monte Carlo simulation	63
C	p_T and R_{AA} data used in analysis	64

1 Introduction

1.1 Aim of the Study

It is well established that partons from hard partonic scattering suffer a large energy loss as they propagate through the medium formed in heavy ion collisions. However, while qualitative features of this energy loss are well established, the quantitative picture is far from clear. Recently significant changes to the paradigm of radiative losses have been proposed and we are still far from the situation where hard partons can actually be used to study the medium.

So far, there has been a number of models of partonic energy loss in the nuclear matter. They all, however, require various assumptions (for overview, see [1]). The perturbative quantum chromodynamical calculations for these models are very sensitive to the initial parameters, which, unfortunately, cannot be determined with certainty. Estimating them leads to a rather nice agreement among different models, but not with the data: tuning the parameters to match the observed nuclear modification factor R_{AA} (ch. 4.2) results in an underestimated asymmetry (elliptic flow) coefficient v_2 (ch. 4.3), and vice versa.

In this analysis I want to compare the in-plane and out-of-plane nuclear modification factors, $R_{AA,in/out}$, for different centrality bins¹ to see if there is a way to characterize radiative energy losses and the effect of the expanding medium. The idea is based on a Glauber model to select two centrality samples, where the (more central) participant profile in-plane has a similar shape as the (less central) out-of-plane. In the most general way, for radiative energy losses one can write:

$$\frac{dE}{dx} \propto \rho^\kappa L^\lambda \quad (1)$$

The centrality sets mentioned above are chosen such that the L^λ part of the energy loss should be of the same magnitude, unless there are significant effects of the flowing medium. The in-plane sample should have a higher flow effect than the out-of-plane one.

Having the centrality sets selected, I will move on to comparing $R_{AAin/out}$ samples ignoring density effects to study if the $R_{AA,in/out}$ show any similarities. Next, I will attempt to correct the R_{AA} 's for density differences. I will allow myself to vary the density contribution to energy loss, i.e. κ in eq. 1 to see if it is possible to get a better $R_{AA,in/out}$ match. I will continue by drawing a naive picture to estimate the radiative energy loss for partons in an expectedly stationary QCD matter and use it to evaluate the characteristic quantities for heavy ion collisions, R_{AA} and v_2 . Finally, I will extrapolate the energy loss from LHC $\sqrt{s} = 2.76\text{TeV}$ lead-lead data to RHIC scales and estimate R_{AA} and v_2 for gold-gold collisions at center-of-mass energy $\sqrt{s} = 200\text{GeV}$.

1.2 Layout of the Thesis

To begin with, in chapter 2, I will briefly discuss the current theory of particle interactions, the Standard Model, and its ingredients for describing the strong interaction – the quantum chromodynamics. I will then continue with a short introduction to the detectors relevant for my analysis in

¹Centrality describes how central a collision is. Low centrality means a collision is central and high centrality means a collision is peripheral.

chapter 3. Next, I will take a deeper look into heavy ion collisions and discuss the theory behind my analysis in chapter 4. A general overview of Glauber model will be provided in chapter 5, followed by a detailed description of my analysis steps in chapter 6. I will present the results in chapter 7, and discuss them in chapter 8. Finally, I will draw the conclusions from my analysis in chapter 9.

The relevant terms and acronyms will be introduced on-the-fly and their summary can be found in Appendix A

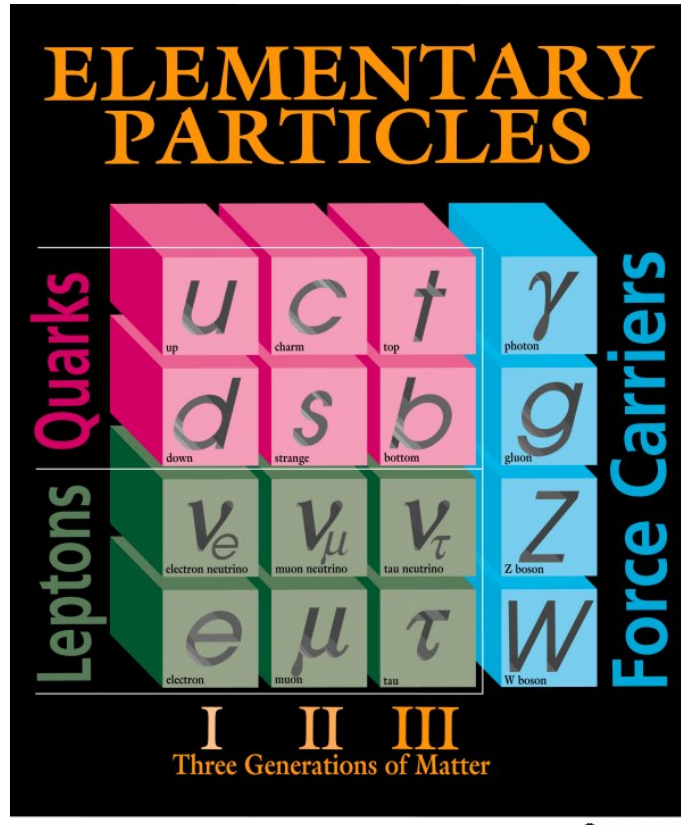


Figure 1: Elementary particles the in Standard Model [2]

2 Standard Model and Quantum Chromodynamics

One of the most remarkable achievements in both theoretical and experimental particle physics is the Standard Model (SM). Though being incomplete, it is able to describe three fundamental forces - *strong*, *weak* and *electromagnetic*. Moreover, as Steven Weinberg, Sheldon Glashow (collaboration) and Abdus Salam (independently) showed in 1967, in the framework of the SM it is possible to unify the latter two into one – *electroweak* theory. Though attempts to further unify electroweak and strong theory have not been successful (there is no experimental evidence that they work), the SM still gives a very fine starting point for further theories.

The fundamental building blocks of matter are classified into three groups in SM: quarks, leptons and gauge bosons (force carriers), see fig. 1. The ordinary matter consists of spin- $\frac{1}{2}$ particles, namely quarks and leptons, which together are called fermions. The gauge bosons are spin-1 particles that mediate interactions: some of them interact only with fermions, while others can also couple to other gauge bosons.

2.1 Lepton sector

Historically, leptons were the first discovered particles that are *actually* elementary. The leptonic sector consists of three generations, each with two leptons:

$$\begin{pmatrix} \nu_e \\ e \end{pmatrix} \quad \begin{pmatrix} \nu_\mu \\ \mu \end{pmatrix} \quad \begin{pmatrix} \nu_\tau \\ \tau \end{pmatrix}$$

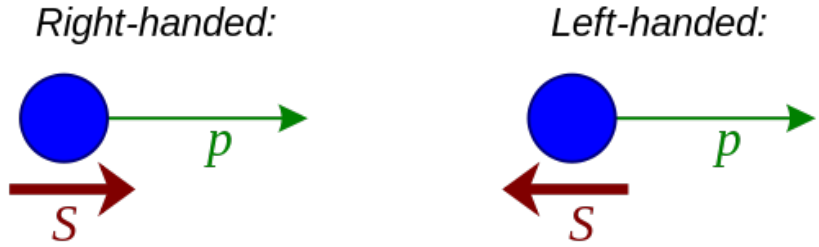


Figure 2: Helicity of a fermion: if the spin and momentum of a fermion are co-directed, the particle is right-handed; if the spin and momentum of a fermion are counter-directed, the particle is left-handed [4]

and their antiparticles. Electrons (e), muons (μ) and tau leptons (τ) have an elementary electric charge $-e$, while neutrinos are neutral.

A lepton number can be defined for each family and is experimentally observed to be conserved in weak interactions; on the other hand, the fundamental reasons why it should be conserved are unknown. While the electron, muon and tauon masses follow a remarkable hierarchy, neutrino masses are not measured yet. They were consistent with zero until 1967, when the first indications of oscillations of solar neutrinos were observed [3]. The neutrino mixing between different families imply that the observed ν_e , ν_μ and ν_τ are the eigenstates of three other neutrinos, ν_1 , ν_2 and ν_3 , and have a non-zero mass as well. In fact, all the three neutrinos are massless in the SM and their oscillations is a topic beyond the Standard Model, thus it will not be covered here.

All the fermions in SM are assigned a *helicity*: a particle is left-handed, if the spin projection on the particle's momentum vector is negative and right-handed, if the projection is positive, see fig. 2 [4]. The Standard Model treats different helicity particles differently. In fact, the left-handed fermions form an $SU(2)$ doublet, while right-handed fermions are singlets. Moreover, as neutrinos have zero mass in the SM, they are moving at the speed of light and thus are always left-handed. Therefore, for the first generation (same for all the generations) there are two $SU(2)$ doublets:

$$\begin{pmatrix} \nu_e \\ e \end{pmatrix}_L \quad \begin{pmatrix} \bar{\nu}_e \\ \bar{e} \end{pmatrix}_R$$

and two singlets:

$$e_R \quad \bar{e}_L$$

where indices L and R denote left- and right-handedness. Note that, as mathematically an antiparticle is equivalent to a particle traveling backward in time, the handedness of an antifermion doublet/singlet is opposite to that of a fermion.

Because of its nature, the weak force only acts on $SU(2)$ doublets, which means that only the left-handed fermions and right-handed antifermions can interact weakly. However, the most important thing about the leptons is that they can only interact *electroweakly* and do not participate in *strong* interactions, as will be explained in the next section.

2.2 Quark sector

Similarly to the leptons, there are six distinct quark flavours: up (u), down (d), strange (s), charm (c), bottom (b) and top (t). They are also divided into three generations:

$$\begin{pmatrix} u \\ d \end{pmatrix} \quad \begin{pmatrix} c \\ s \end{pmatrix} \quad \begin{pmatrix} t \\ b \end{pmatrix}$$

Moreover, depending on their handedness, they can form either singlets or doublets under $SU(2)$:

$$\begin{pmatrix} u \\ d \end{pmatrix}_L \quad \begin{pmatrix} \bar{u} \\ \bar{d} \end{pmatrix}_R \quad u_R \quad d_R \quad \bar{u}_L \quad \bar{d}_L$$

and the electroweak forces will act differently on left- and right-handed groups. There is a remarkable mass hierarchy in the quark sector, which cannot be explained, and contrary to the leptons, quarks carry a fractional number of elementary charge e . As it will be shown later, quarks are always bound to each other and there is no model-independent way to measure their mass. Hence it is common to provide two masses for each quark: "free" quark (mass if the quark was free)² and constituent quark (bound quark mass). Electric charge and the two masses for all six quarks are given in table 1 [5, 6]

Table 1: Electric charge, "free" quark and constituent quark masses [5, 6]

Quark	El. charge (in e)	"free" quark mass	constituent quark mass
u	2/3	2 - 8 MeV/ c^2	336 MeV/ c^2
d	-1/2	5 - 15 MeV/ c^2	340 MeV/ c^2
s	-1/2	0.1 - 0.3 GeV/ c^2	486 MeV/ c^2
c	2/3	1.0 - 1.6 GeV/ c^2	1.55 GeV/ c^2
b	-1/2	4.1 - 4.5 GeV/ c^2	4.73 MeV/ c^2
t	2/3	168 - 192 GeV/ c^2	No bound states

In general, electroweak interactions conserve the total quark number (i.e. total number of quarks minus total number of antiquarks), but not explicitly for each generation. That is, an s quark can turn into a d quark, see fig. 3.

The most important feature of quarks is that they carry the *color charge*. Just as the electrically charged particles interact with each other electromagnetically, the color charge gives rise to *strong* interactions. The strong force is described by the $SU(3)$ group and hence has three distinct charges (which have nothing to do with actual colors): red (r), green (g), blue (b) and their anti-colors. All the hadronic matter (i.e. matter made of quarks) occurring in nature is colorless. There are several ways to combine these colors into colorless states: $|r, g, b\rangle$, $|\bar{r}, \bar{g}, \bar{b}\rangle$, $|r, \bar{r}\rangle$, $|g, \bar{g}\rangle$ or $|b, \bar{b}\rangle$ where the color order is irrelevant. Therefore, each hadron consists of either three (anti)quarks (baryons and antibaryons) or a quark-antiquark pair (mesons).

²Since free quarks have not been observed, masses are calculated and hence are model-dependent.

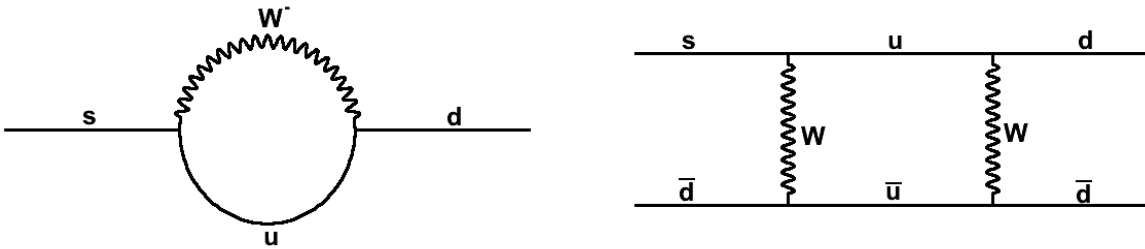


Figure 3: s quark decaying into d quark in a penguin process (left) and 2W exchange (right)

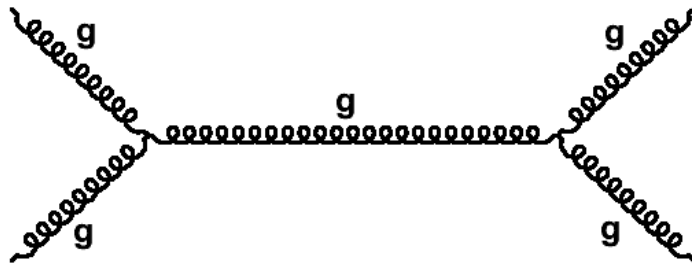


Figure 4: Gluon-gluon scattering via interchange of a gluon

2.3 Gauge bosons

Gauge bosons are the force carriers in the Standard Model. Each of the forces is mediated via different bosons: gluons (g) for the strong force, photons (γ), Z^0 and W^\pm bosons for the electroweak force. Mathematically, they are described by field equations for massless particles, thus at a naive level, one would expect them to have zero masses. In reality, that is not the case – while some of them are indeed massless (e.g. a photon), W^\pm and Z^0 have considerable masses that have been observed experimentally. The masses obtained by W/Z are explained by the Higgs mechanism [7], which has recently been confirmed by the discovery of a Higgs boson [8].

A very important implication in the SM is the requirement for all the forces in the SM to be gauge invariant. As a result, the strong force group becomes non-abelian (i.e. it has at least two non-commuting elements a and b so that $a \cdot b \neq b \cdot a$), which allows the force propagators – gluons – to interact with each other (e.g. gluon-gluon scattering, see fig. 4).

Contrary to other gauge bosons, gluons are *colored* particles; combining all the possible colors, there are 8 different gluons. The color charge is conserved in strong interactions for each color explicitly, see fig. 5.

Finally, the strong force does not fall towards zero with increasing distance, as compared to e.g. the electromagnetic force. Hence, the potential of the strong interaction grows as two color charges get separated from each other. One can imagine two interacting color charges as connected by a rubber band (*Lund String Model*), see fig. 6. As the charges get more and more separated, the potential energy between the quark-antiquark pair increases until eventually it becomes energetically favorable to produce a new $q\bar{q}$ pair from vacuum. At this point the "string" breaks into two $q\bar{q}$

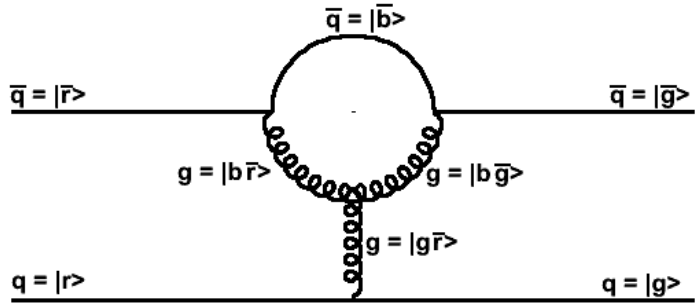


Figure 5: Gluon exchange between a quark and virtual gluon. Color charge is conserved in each vertex.

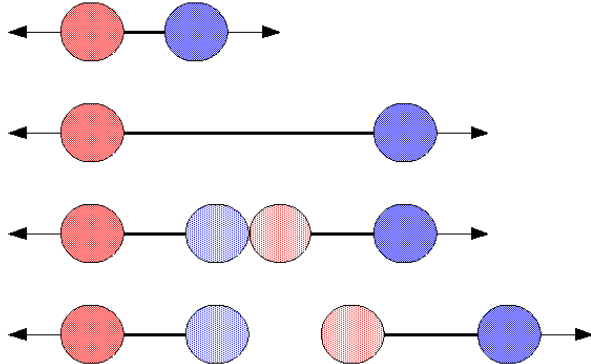


Figure 6: A quark-antiquark pair interacting strongly. Potential energy grows as the distance between $q\bar{q}$ increases until eventually it becomes energetically favorable to create a new $q\bar{q}$ pair from vacuum

systems.

2.4 Quantum Chromodynamics

A key ingredient in the Standard Model is the quantum field theory of the strong force – Quantum Chromodynamics (QCD). At high momentum transfers, the scattering of quarks and gluons can be calculated perturbatively, thus it is essentially a theory of "free" partons [9]. On the other hand, at low momentum transfers, a projectile parton cannot resolve all the constituents of a target and hence scatters from a compound of its constituents. The problem with the latter case is that every quark is surrounded by a virtual field of gluons and sea quarks that screen the constituent quark color charge. The effective scattering charge is then a superposition of all the virtual and real colors and in the large systems is impossible to be calculated analytically.

As mentioned in the previous section, due to the nature of strong force, quarks are always *confined*. The coupling strength between two quarks can be described by the strong coupling constant

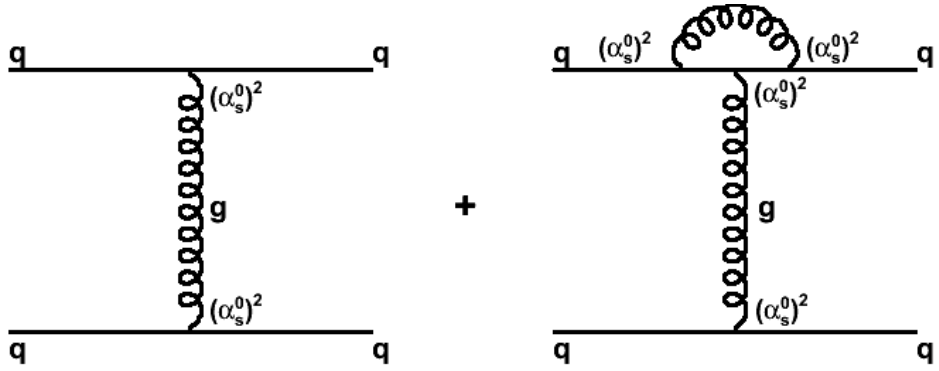


Figure 7: $q\bar{q}$ scattering at lowest order (left) and with one gluon radiation correction (right)

α_s . Ironically, the observed α_s^{obs} is not actually a constant and depends on the energy scale (i.e. momentum transfer) at which it is measured.

Consider a simple $q\bar{q}$ scattering, fig. 7. To the lowest order, it is just one gluon exchange. Such a process has two vertices and thus the amplitude of it will be proportional to $T \propto (\alpha_s^0)^4$. On the other hand, there exist higher order diagrams which include more vertices, e.g. one virtual gluon emission and reabsorption. An amplitude for such a process will be proportional to $T \propto (\alpha_s^0)^8$. All of these processes will contribute to the measured coupling strength³ α_s^{obs} . The observed α_s^{obs} will thus be a function of a scale μ^2 , at which it has been observed, and some reference $\alpha_s^0 = \alpha_s(\mu_0^2)$. In general, it can be expressed as:

$$\alpha(\mu^2) = \frac{\alpha(\mu_0^2)}{1 + \beta_0 \alpha(\mu_0^2) \ln\left(\frac{\mu^2}{\mu_0^2}\right)} \quad (2)$$

where β_0 accounts for degrees of freedom for possible corrections.

The coupling strength dependence on the measurement scale is called the *running coupling* and is present for all the interactions in SM, however, it is of particular importance in QCD. The β_0 in QCD is given by

$$\beta_0 = \frac{1}{12\pi} (33 - 2n_f) \quad (3)$$

where $n_f \leq 6$ is the number of quark flavours with masses up to the momentum scale. Substituting eq. 3 to eq. 2 one can see that, as the momentum transfer $\mu^2 \rightarrow \infty$, the strong coupling constant $\alpha_s(\mu^2 \rightarrow \infty) = 0$ and the quarks finally become free. The effect is called *asymptotic freedom*⁴, and the state of matter, consisting of asymptotically free quarks – the Quark Gluon Plasma (QGP) – will be described in sec. 4.1

³Note that as the emitted and reabsorbed gluon is virtual, the diagram with one gluon correction is divergent.

⁴David Gross, Frank Wilczek and David Politzer were awarded the Nobel Prize for the discovery of asymptotic freedom in year 2004.

3 Detectors

The Large Hadron Collider, LHC, is the largest particle accelerator in the World, built at the European Organisation for Nuclear Research (CERN), Geneva, Switzerland. It is situated in the former Large Electron Positron Collider (LEP) tunnel and features a 27 km circumference ring to produce collisions of both protons and nuclei – so far, extreme energies have been reached for all variations of systems: 8 TeV for proton-proton (pp), 2.76 TeV for lead-lead (PbPb) and 5.02 TeV for proton-lead (pPb) collisions.

One might ask: what is the purpose of smashing these tiny particles? The answer is simple: by looking into the products of collisions under the unprecedented energy scales we are also looking into the smallest chunks of matter and the processes they undergo. Not only this gives information about the fundamental laws of the nature, but also provides an insight into a very distant history of the Universe.

Needless to say, accelerating particles up to such scales is not an easy task – extraordinary machinery is needed to get them to collide at those energies. Hence, a number of pre-accelerators are used before injecting particles into LHC. A schematic view of all the major accelerators at LHC is given in fig. 8 [11].

To detect the products of the collisions, four different detector systems are used:

- ATLAS – A Toroidal LHC Apparatus
- ALICE – A Large Ion Collider Experiment
- CMS – Compact Muon Solenoid
- LHCb – LHC Beauty Experiment

3.1 ATLAS

ATLAS is a general purpose detector at LHC, aiming at a wide range of physics topics from discovering the Higgs boson to searching for extra dimensions and dark matter. It is the largest LHC detector – 45 m length, 25 m height with a weight of roughly 7000 t[12]. A schematic view of the detector with its subdetectors is shown in fig. 9.

Though it features a number of subdetector systems, this report will only cover the ones that are relevant for its subject: the *inner detector* (ID) and the *forward calorimeter* (FCal). The ID is located closest to the collision point and contained in 2 T magnetic field, induced by a superconducting solenoid magnet. The Lorentz force on a charged particle moving in a magnetic field can be written as [10]:

$$\frac{d\vec{p}}{dt} = q\vec{v} \times \vec{B} \quad (4)$$

For the transverse component (perpendicular to magnetic field) eq. 4 reads:

$$p_T = qrB \quad (5)$$

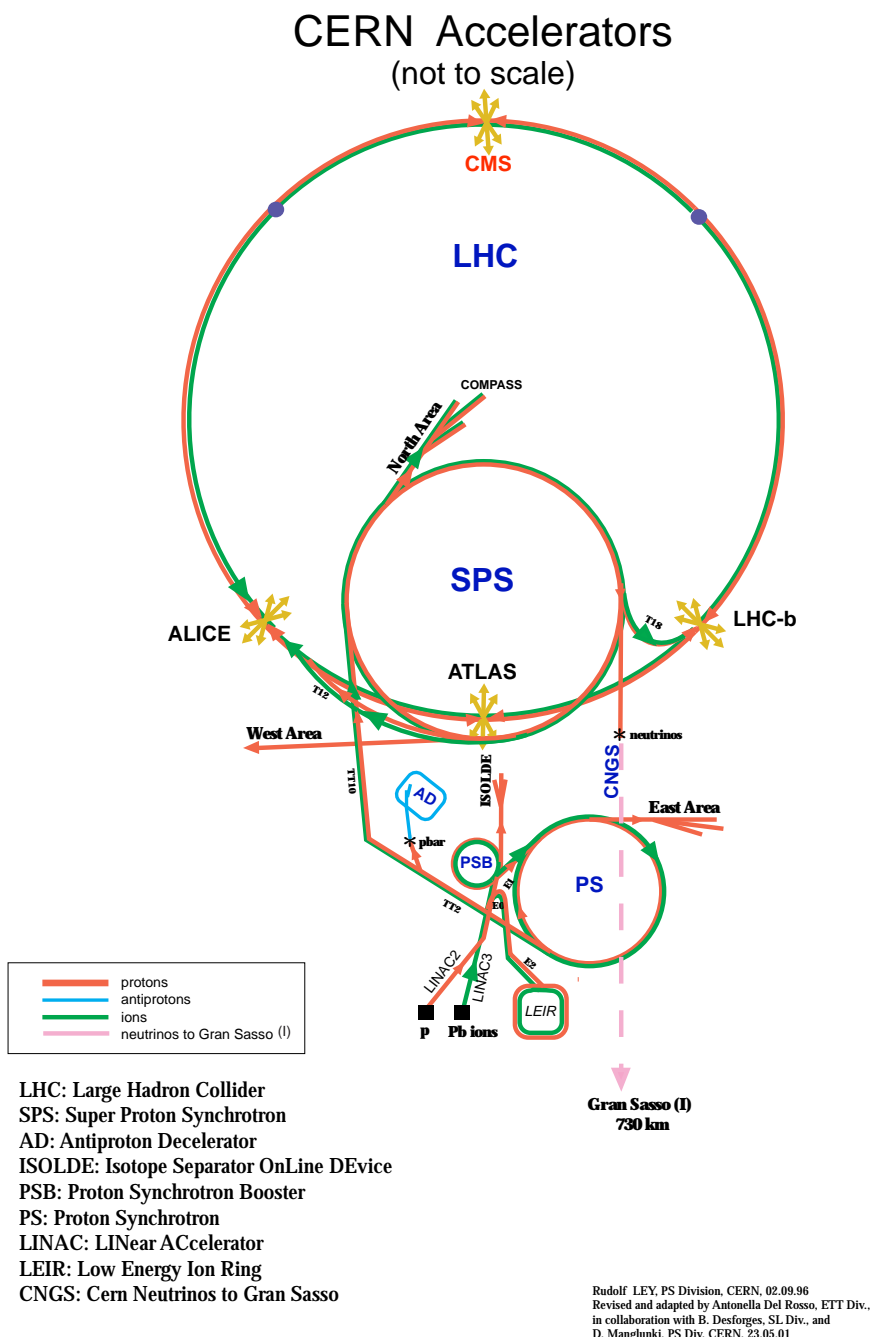


Figure 8: Schematic view of LHC and its pre-accelerators [11]

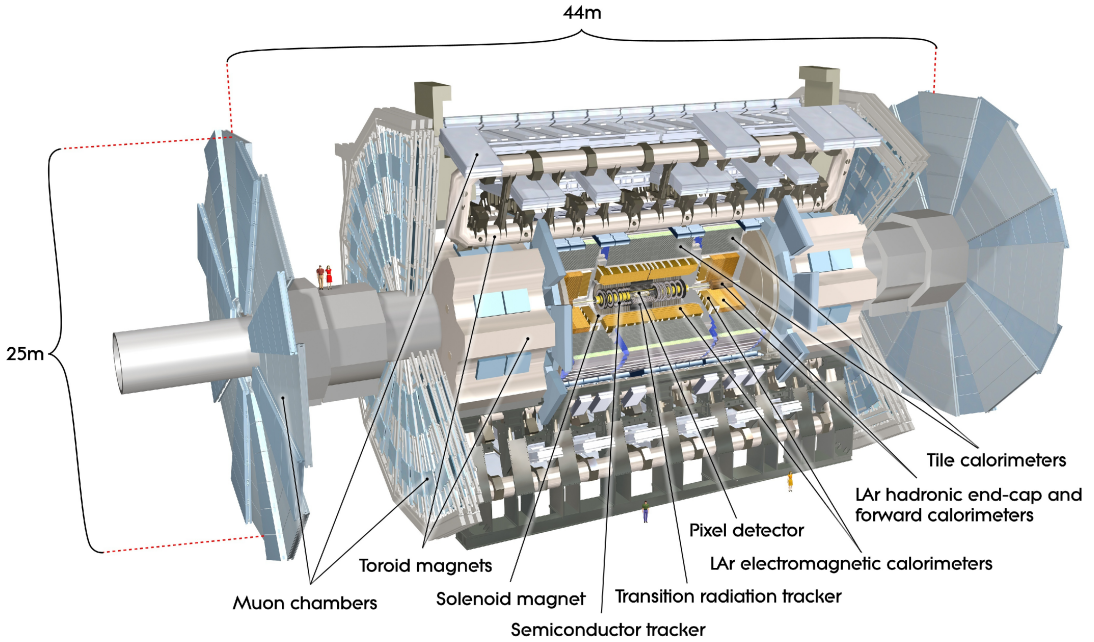


Figure 9: Schematic view of the ATLAS detector [12]

where q is the charge of the particle. Therefore, by measuring the bending radius, r , of a particle, its transverse momentum p_T can be estimated.

ID consists of a number of layers of silicon pixel detectors (Pixel) and semiconductor microstrip trackers (SCT). Usually, a charged particle traverses three layers of Pixel detector and four double-sided SCT layers [13].

One should also keep in mind that during a collision, particles are emitted in all the directions. To detect all the particles produced, the detector should cover 4π surface area around the collision. This usually is impossible to achieve experimentally; common parameters characterizing the coverage area of detector are azimuthal acceptance ϕ and pseudorapidity interval η . The former one is simply the covered azimuthal angle (perpendicular to beam direction); the latter can be expressed as:

$$\eta = -\ln \left[\tan \left(\frac{\theta}{2} \right) \right] \quad (6)$$

where θ is w.r.t. the beam axis. Relating it to the momentum of a particle:

$$\eta = \frac{1}{2} \ln \left(\frac{|\vec{p}| + p_L}{|\vec{p}| - p_L} \right) \quad (7)$$

where p_L is the longitudinal component of \vec{p} , i.e. \vec{p} projection on the beam axis. Particles with no longitudinal momentum will be emitted perpendicular to the beam axis ($\Theta = 90^\circ$) and thus $\eta = 0$, see fig. 10 [14]. The inner detector has a full azimuthal angular acceptance and detects particles emitted in pseudorapidity region $|\eta| < 2.5$.

The forward calorimeter consists of tungsten and copper absorbers and uses liquid argon as active medium. The total thickness of FCal is roughly 10 interaction lengths and it covers the pseudorapidity interval of $3.2 < |\eta| < 4.9$. To measure the centrality (see chapter 4) of the collision, all the energy

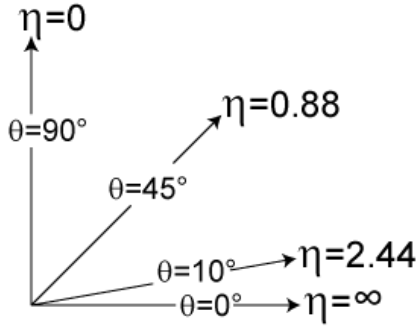


Figure 10: Pseudorapidity values for various emitted particle angles θ w.r.t. beam axis ($\theta = 0$). Particles with $\theta = 0^\circ$ and $\theta = 90^\circ$ respectively have longitudinal and transverse momentum components only.

deposited in the calorimeter is used, while the reaction plane is determined using only the first layer of FCal⁵.

3.2 ALICE

The *ALICE* detector is the only detector at LHC dedicated particularly for heavy ion experiments. Being 26 m in length, 16 m in height and weighting roughly 10000 t [15], it is designed to detect and identify individual hadrons, leptons and photons in mid-rapidity range and muons at large rapidities under extreme conditions – with charged particle multiplicities, $\frac{dN_{ch}}{d\eta}$, of up to 8000 per η unit. To perform particle identification (PID), the momentum of a particle p , time of flight information, transition and Cherenkov radiation, and the specific energy loss $\frac{dE}{dx}$ are measured track-by-track in most of the cases [16]. Combining all the information, charged hadrons with transverse momentum $0.1\text{GeV}/c < p_T < 20\text{GeV}/c$ can be identified.

The *Inner Tracking System* (ITS) is located closest to the collision point in the so-called central barrel. It consists of six cylindrical layers of silicon detectors and is able to reconstruct the position of the primary vertex with a resolution of $\sim 100\mu\text{m}$ [15]. The role of this detector is of high importance: the low momentum particles ($p_T \lesssim 200\text{MeV}/c$) and large momentum heavy hadrons do not travel far from the collision point and decay (or are bent by the magnetic field) before reaching the outer detectors; therefore, a detector system close to the interaction point is needed. Moreover, the detector has to be extremely sensitive, as a very high resolution is needed to determine the position of origin for the particle detected.

A crucial detector of ALICE is the *Time Projection Chamber* (TPC). Covering the azimuthal angle of 2π and pseudorapidity region $|\eta| < 0.9$, it is able to track the trajectory of a traversing particle in three dimensions, measure its momentum and energy loss and hence identify the particle in $0.1\text{GeV}/c < p_T < 20\text{GeV}/c$ range. The layout of the ALICE TPC is shown in fig. 12 [16]. The cylinder of 5.1 m length and 5.56 m diameter is filled with $Ne - CO_2 - N_2$ gas and divided into two symmetric halves by the central cathode membrane. A uniform electric field of up to 400 V/cm along the beam axis is created by the central electrode; a parallel magnetic field is applied by a solenoid magnet, surrounding the whole compartment. A charged particle passing the detector will

⁵Using only Layer 1 on FCal was found to minimize the fluctuations of reaction plane measurement [13].

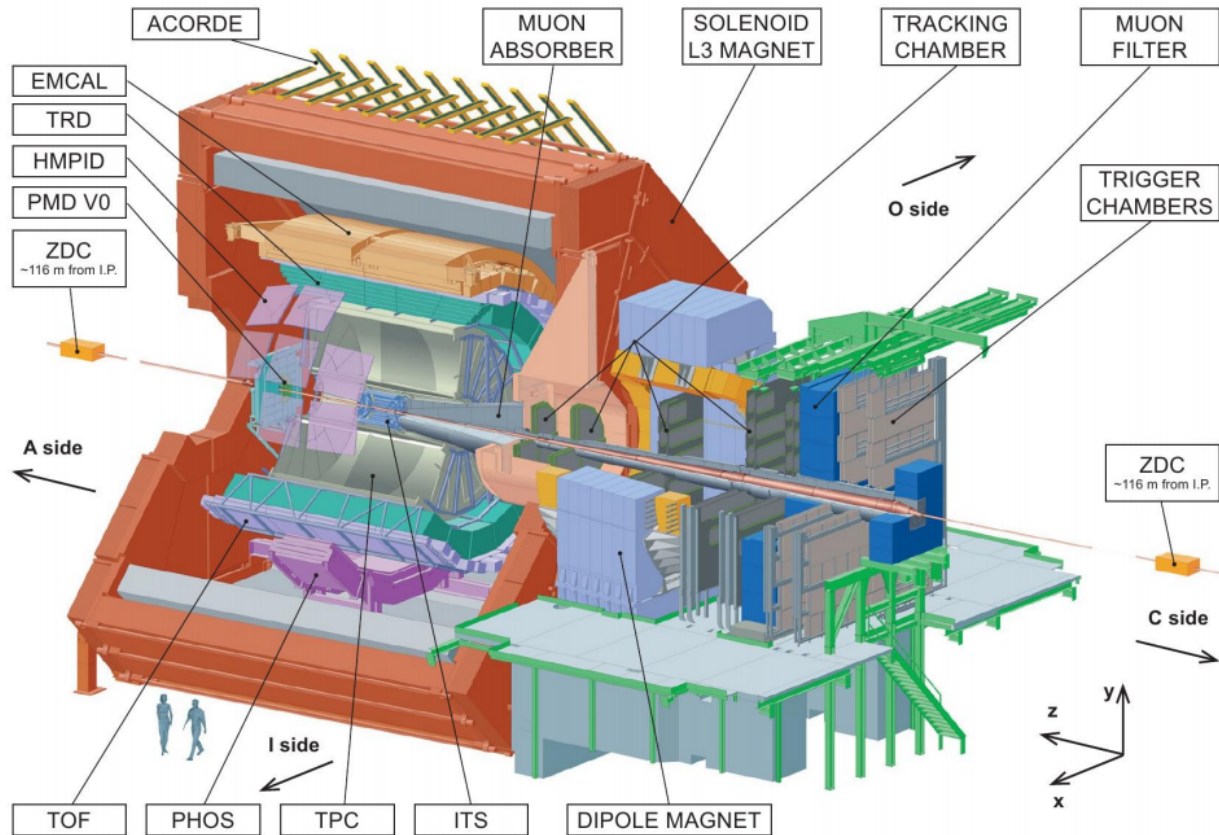


Figure 11: Schematic view of the ALICE detector [16]

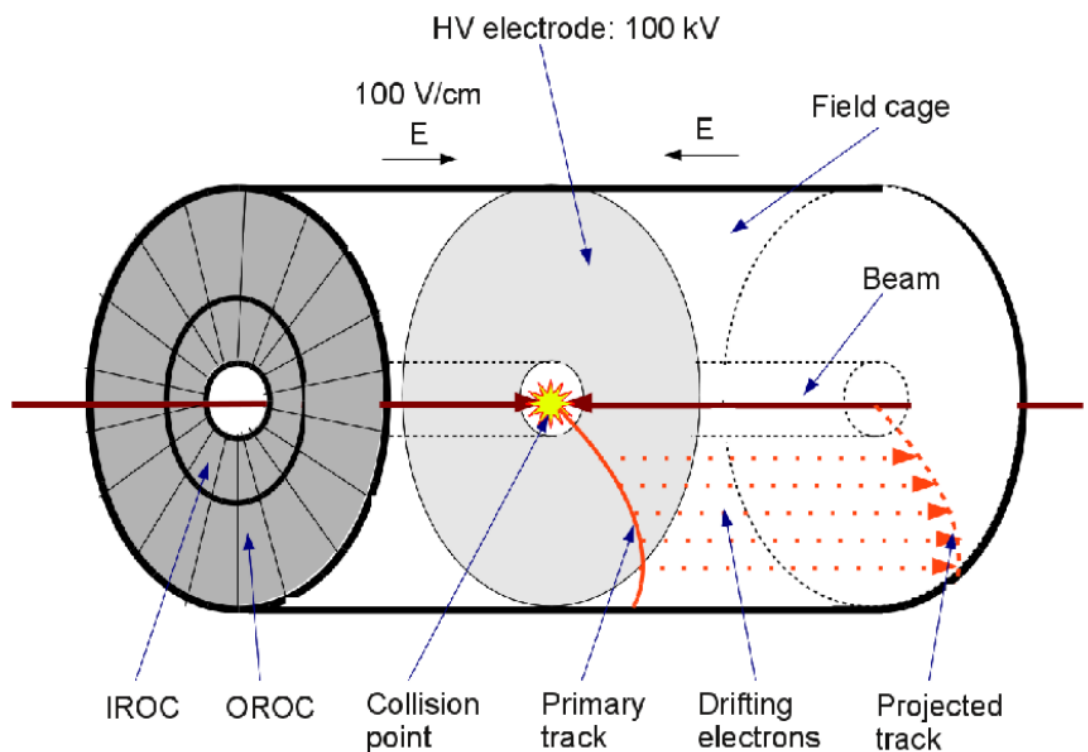


Figure 12: Schematical layout of the ALICE Time Projection Chamber [16]

lose energy and ionize the gas along its trajectory, which is bent due to the presence of the magnetic field. The created free electrons will drift towards the endcaps of the TPC, projecting the initial particle track on two read-out chambers (inner and outer, IROC and OROC). IROC and OROC are Multi Wire Proportional Chambers (MWPC) with segmented cathode pads for read-out: the MWPC is used to cause an avalanche of the drifting charges close to the endcaps; the multiplied charge then induces a signal on the cathode pads. Knowing the location of the pads and measuring the charge collected on each of them, it is possible to determine the 2-dimensional trajectory of the initial particle and its energy loss. The third spatial component is then reconstructed by measuring the time it takes for the electron to drift from the track to the anode wires.

Furthermore, there are several global detectors used for triggering purposes [16]:

- Forward Multiplicity Detector – FMD – consists of several arrays of silicon strip detectors to measure charged particle multiplicity $\frac{dN_{ch}}{d\eta}$;
- VZERO – two scintillating hodoscopes on each side of the collision point. Used for triggering, centrality, luminosity estimations and beam-gas interaction background removal;
- TZERO – used to measure the vertex position and the time of the collision.

The last sub-detector system relevant to this analysis is the *Zero Degree Calorimeter*, ZDC. Placed around 116 m away from the collision point along the beam axis (hence "zero degree") on both sides, it is composed of overall four calorimeters: two to detect protons (ZP) and two to detect neutrons (ZN) [17]. Each calorimeter is made of metal plates – brass for ZP and tungsten alloy for ZN – grooved to hold a number of quartz fiber matrices which, in turn, are coupled to photomultipliers. ZDCs aim is to measure the energy of the nucleons that did not participate in the collision⁶. When such a nucleon hits a metal plate, it creates a cascade of secondary particles. If some of these particles enter the quartz fiber and are fast enough, they will radiate light (Cherenkov radiation). Some of the radiated photons will not escape the quartz due to internal reflection and thus will propagate through the fiber and create a signal in a photomultiplier. The number of detected photons can then be related to the energy carried away from collision, yielding indirect information on how central the collision is.

The results used in this analysis, namely, the nuclear modification factor R_{AA} (see sec. 4.2), were obtained using ITS and TPC for track reconstruction and vertex position determination. Events were triggered by a combined signal from VZERO and two innermost layers of ITS – Silicon Pixel Detectors (SPD). VZERO and ZDC were also used to determine centralities of collisions and remove the beam-gas interaction products.

⁶If a PbPb collision is not central, there will be a number of nucleons that do not collide and hence continue with their original momentum. These nucleons are called *spectators*.

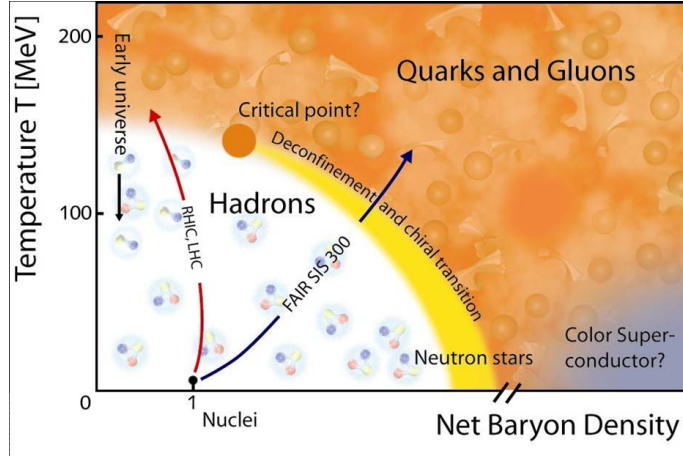


Figure 13: QCD phase diagram. At low temperatures and net baryon densities, the matter is hadronic, i.e. quarks are confined inside nucleons. With increasing density and/or temperature, we gradually approach a transition point, where the strong force, binding the constituents together, asymptotically goes to zero and thus quarks and gluons become (asymptotically) free.

4 Heavy Ion Collisions

The first 'heavy' ion experiment dates back to 1909, when H. Geiger and E. Marsden observed a reflection of α -particles from a thin gold foil. The results indicated that the most of the atom's mass was concentrated in a volume much smaller than the size of an atom. It suggested the failure of Thompson's model⁷ and led to the discovery of the nucleus (Ernest Rutherford, 1911), the neutron (James Chadwick, 1932) and eventually the nuclear model as we have it today.

4.1 Quark Gluon Plasma

The modern heavy ion experiments have evolved a lot ever since. At first, nuclear experiments were conducted with radioactive nuclei (energy scales of up to tens of MeV), which was sufficient to observe all the three decays – α , β and γ . The first heavy ion collisions at modestly *relativistic* energies were conducted at Lawrence Berkley National Laboratory, LBNL, in Berkley, USA, and the Joint Institute for Nuclear Research, JINR, in Dubna, Russia. The energies achieved were up to 2GeV per nucleon and were already hundreds of times larger than the ones resulting from radioactive decays [19].

Discoveries at LBNL and JINR motivated further development of accelerators in Brookhaven National Laboratory (BNL) and European Organization for Nuclear Research (CERN) with ever-increasing energy scales and nuclear sizes. More than a decade ago, first gold-gold collisions at center-of-mass energy $\sqrt{s_{NN}} = 200\text{GeV}$ took place in the Relativistic Heavy Ion Collider (RHIC) at BNL; since then, the energy was increased even further by an order of magnitude: in year 2010, first lead-lead collisions at unprecedented scales, $\sqrt{s_{NN}} = 2.76\text{TeV}$, were observed at LHC, CERN.

Collisions under such high energies are expected to result in two QCD phase transitions: *decon-*

⁷Thompson's model – also known as *plum pudding model* – assumes an atom, composed of electrons (plums) immersed in a cloud of positive charge (pudding) [18]

finement and chiral symmetry restoration. At baryonic densities⁸ higher than the critical point, the transition is expected to be of the first order, i.e. hadronic matter is gradually deconfined into quark and gluon matter, see fig. 13. On the other hand, at lower densities the transition is expected to be of the second order, and no clear phase boundary exist.

In general, the deconfined medium – the so-called Quark Gluon Plasma – does not exist in nature at present day, other than possibly in the cores of heavy neutron stars. However, it is believed that just moments after the Big Bang all the matter was in this particular state. Most importantly, modern experiments enable us to reproduce the QGP in the laboratory. The theory behind these experiments is that in a very hot and dense matter, the strong coupling constant becomes extremely small; moreover, as the energy is pumped into the system, a large number of $q\bar{q}$ pairs will be created. Although the produced pairs will be colorless (so the whole system remains colorless), each of the quarks individually will carry a color charge. Consider some initial quark q_1 with color c_1 . If another quark q_2 with color c_2 is created close to q_1 , it will screen the color charge c_1 . The potential of color field created by q_1 can be written as

$$V_{q_1}(r > r_{Debye}) = \frac{e^{-\frac{r}{r_{Debye}}}}{r} \quad (8)$$

where r_{Debye} is *Debye radius* (similar to electrons in a conductor). Eq. 8 means that after some distance r_{Debye} , the interaction strength will decrease exponentially [16].

There are two ways of achieving the deconfined phase of matter: either increasing the net baryonic density or the temperature of the system. The former is considered to be the case for the cores of neutron stars, where the densities reach up to $8 \cdot 10^{17} \frac{\text{kg}}{\text{m}^3}$ [20]. In this scenario, few $q\bar{q}$ pairs are produced; however, the existing quarks are compressed so much that the distances between them essentially become $r < r_{Debye}$, color charges are screened and hence quarks and gluons act as if they were free.

In practice, QGP is created by smashing heavy nuclei into each other at very high energies. Though in this scenario the net baryonic density is still rather low, the QCD phase transition is achieved due to extreme temperatures of the system⁹: colliding nucleons at $\sqrt{s} = 2.76 \text{ TeV}$, a very large number of $q\bar{q}$ pairs is created in the colliding volume. Though these (anti)quarks will not contribute to the net baryonic density, they will be created close to the existing quarks and eventually will participate in the screening effect, as it is the density of q and \bar{q} which is the most relevant quantity. In other words, a color charge can just as well be screened by a newly created quark as it can be screened by compressing (i.e. moving closer together) the pre-existing quarks.

4.2 Nuclear Modification Factor R_{AA}

In general, QGP properties are expected to be extracted from a comparison of some observable, Ψ , measured in nucleus-nucleus (AA for short) collisions (QCD medium) and pp collisions (QCD vacuum). The resulting ratio can be a function of the center-of-mass energy \sqrt{s} , centrality, (pseudo)rapidity

⁸Usually referred to as chemical potential μ

⁹This is how the Universe is believed to have evolved after the Big Bang, see fig. 13

y (η), emerging particle mass m and its transverse momentum p_T [21]:

$$R_{AA}(\sqrt{s}, b, y, m, p_T) = \frac{\Psi_{AA}(\sqrt{s}, b, y, m, p_T)}{\Psi_{pp}(\sqrt{s}, b, y, m, p_T)} \quad (9)$$

where Ψ_{AA} is the observable from nucleus-nucleus collision. One should also note, that in absence of a QCD medium or other collective effects, a heavy ion collision can be considered as a *scaled up* sum of pp collisions. Therefore, to avoid biasing the ratio by this trivial scaling, R_{AA} should also be normalized to pp scales. For *hard* partons (large transverse momentum), every binary collision results in an *inelastic* process and can hence be seen as a pp collision; thus, for high p_T particle production, the number of binary collisions N_{bin} is the expected scaling factor in R_{AA} . On the contrary, *soft* partons (low p_T) are created in *string fragmentation*, i.e. when two quarks get separated from each other and a $q\bar{q}$ pair is created between them, see chapter 2.3. Hence the number of soft partons emerging from AA collision are expected to scale as the number of participating nucleons, N_{part} . This is a very naive and simplified picture; however, as this thesis focuses on $p_T \gtrsim 10$ GeV region, partons will be considered as *hard* and it will always be assumed that R_{AA} scales with $\langle N_{bin} \rangle$, if no significant collective effects are present.

In reality, the actual measured quantity is the particle multiplicity, $\frac{dN^{sc}}{dp_T}(\sqrt{s}, b, m, p_T)$, where the superscript *sc* denotes particle specie and charge. The ratio is then:

$$R_{AA}^{sc}(\sqrt{s}, b, \eta, m, p_T) = \frac{(\frac{dN^{sc}}{d\eta}(\sqrt{s}, b, m, p_T))_{AA}}{\langle N_{bin} \rangle (\frac{dN^{sc}}{d\eta}(\sqrt{s}, b, m, p_T))_{pp}} \quad (10)$$

and represents the particle production ratio in nucleus-nucleus collisions compared to proton-proton systems, scaled by $\langle N_{bin} \rangle$.

There are three possible scenarios for the observed R_{AA} :

- $R_{AA} > 1$ – particle production per binary collision is *enhanced* in AA collisions
- $R_{AA} = 1$ – particle production per binary collision in AA collisions is the *same* as in pp collisions
- $R_{AA} < 1$ – particle production per binary collision is *suppressed* in AA collisions

The deviations from $R_{AA} = 1$ can then be linked to strongly interacting medium effects.

4.3 Flow

In late 1970's, indications of a dense and expanding medium, produced in heavy ion collisions, were reported by J. Gosset *et al.* [22] and several other authors [23]. This was a very strong support for ideas describing nuclear collisions macroscopically in terms of relativistic fluid dynamics. Later observations of transverse (perpendicular to the beam axis) particle production angular anisotropy [24] led to various numerical solutions of relativistic fluid dynamics equations, which qualitatively reproduced the angular momentum distribution features of low momentum hadron production in AA collisions.

At present day, the azimuthal angular distribution of particle production in heavy ion collisions is usually expressed in Fourier expansion [25]:

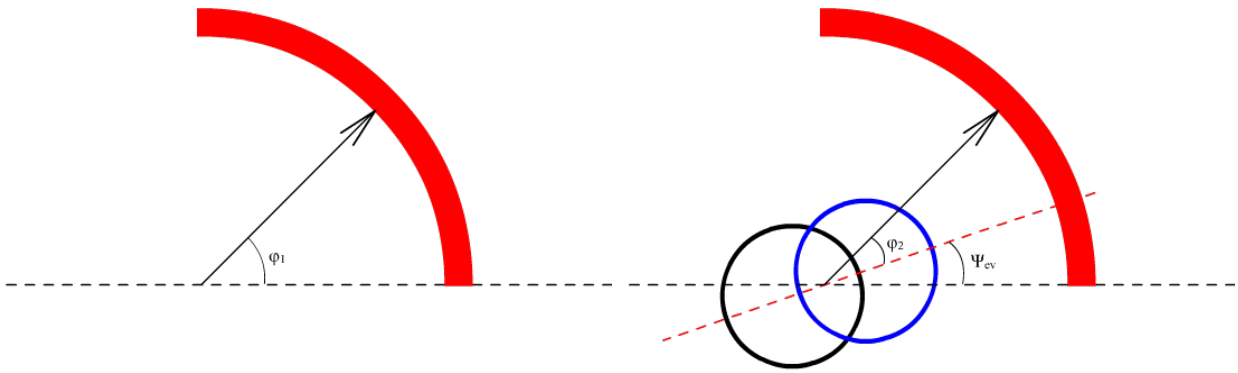


Figure 14: A particle, detected at some angle φ_1 in detectors reference system (left panel), can be emitted at any angle φ_2 w.r.t. event plane (right panel)

$$\frac{dN}{d\eta d^2p_T}(\varphi) = \frac{dN}{2\pi p_T dp_T d\eta} [1 + \sum_{k=1} 2v_k \cos(k(\varphi - \Psi_{RP}))] \quad (11)$$

where $d\eta$ is the pseudorapidity interval, v_k is the k -th Fourier coefficient and Ψ_{RP} denotes the reaction plane (see next chapter) angle relative to the horizontal plane.

Reaction Plane

Consider two colliding nuclei with their centres defining a plane, which represents a symmetry plane w.r.t. the nuclear geometry. A particle is emitted from the colliding region at some unknown angle φ w.r.t. this plane. The detector then detects the particle at angle φ_1 relative to its own reference system, see left panel of fig. 14. As the colliding system plane is different from collision to collision, the *detected* particle angular distribution is not equivalent event-by-event, unless related to the collision plane of the system, see right panel of fig. 14. Therefore, to relate the particle emission angles with the detected spectrum, this common reference plane has to be deduced for each collision.

In theory, the reference plane of the system is called the *event plane* and is a plane where the centers of two colliding nuclei reside (red dashed line in right panel of fig. 14). However, in the experiment that means one would have to determine the exact position of each nucleus, which is rather impossible. Instead, a quantity called *reaction plane* is used. The idea behind this parameter is to find a plane that maximizes the participating nucleon spread perpendicular to the plane, or minimizes $\sum |p_T \cos(\phi - \Psi_{RP})|$, event by event. In an ideal case, the reaction plane should coincide with the event plane, however, in reality, due to finite number of nucleons and their density fluctuations, there will be a spread of Ψ_{RP} relative to the event plane.

A number of different methods are available to determine the reaction plane experimentally, for a detailed description one can refer to [25]. The method used in this analysis will be described in sec. 6.1.

Fourier coefficients

Each of the Fourier coefficients v_k in eq. 11 correspond to a different component of flow. It was first believed that k -odd components should be zero, as any asymmetric flow would violate the momentum

conservation ($k = 1$) or symmetries ($k \geq 3$); recently it has been shown that this is not the case and due to local nucleon density fluctuations, a small asymmetric flow is also observed, while the momentum maintains conserved [26, 27].

Direct flow, described by v_1 , is the first order flow. There are two effects contributing to the observed v_1 :

Local nucleon fluctuations. Though the theoretical nucleon density distribution in a nucleus is spherically symmetric, in reality there will be local density fluctuations. The resulting colliding region will thus not be symmetric in the individual collision. The spatial asymmetries of the colliding region will result in different angular expansions in momentum space, hence giving rise not only to direct flow, but to higher odd-components as well. One of the cases where the spatial asymmetry is well seen is shown in the left panel of fig. 15 (simulation with Glauber Monte Carlo, see ch. 5 and 6.1) – here the colliding nucleon (*participant*) distribution shows a clear triangular contour, which will result in *triangular flow*, v_3 .

Tilt of the colliding system [26]. Consider a non-central collision of two spherical nuclei. The initial pressure in the produced QCD matter is shown in fig. 16. For non-central collisions in 3-dimensional space, the collision plane is not perpendicular to the beam axis, but rather tilted. At small pseudorapidities ($\eta_s \approx 0$) there will be no preferred direction as the pressure is symmetric, $p(\eta_s, x) = p(\eta_s, -x)$, see fig. 16 [26]. However, at high $|\eta|$, $p(\eta_h, x) \neq p(\eta_h, -x)$ and partons moving to opposite x directions will be boosted by different amounts of p_T . In the ideal case (completely spherical nuclei) one would expect

$$p(-\eta, -x) = p(\eta, x) \quad (12)$$

and the effect should be cancelled out once a symmetric $|\eta| < a$ window is chosen. However, as discussed above, due to the presence of local nucleon fluctuations and nuclei not being completely spherical, eq. 12 does not hold and thus a directional movement of the colliding system is observed.

For the *elliptic flow*, defined by v_2 , a non-central (impact parameter $b \neq 0$) nucleus-nucleus collision is considered, see fig. 17 [28]. The colliding nucleons (participants) form an ellipsoid-like region, whereas the remnant nucleons (spectators) are not interacting. The participant distribution gradient in the reaction plane direction is lower than that in out-of-plane (perpendicular to the reaction plane). This spatial anisotropy will then be transferred to momentum anisotropy, enhancing the p_T of hadrons produced in-plane. In other words, as the concentration of participants falls off faster in the in-plane direction, the medium will expand faster in in-plane, thus the partons moving in this direction will gain more p_T . As this expansion will cause an elliptic hadron p_T angular distribution, the second order flow contribution is called *elliptic flow*. A simulated event where the spatial participant distribution shows a clear elliptic countour is shown in fig. 18.

The measured v_2 for PbPb collisions at $\sqrt{s_{NN}} = 2.76\text{GeV}$ by the ATLAS detector for several p_T bins is given in fig. 19 and will be discussed later.

In general, as the k -odd components (see eq. 11) are caused by fluctuations, they will be somewhat smaller than k -even. Furthermore, while v_2 is affected by both flow (at low p_T) and the quenching (at high p_T), v_3 will only result from flow (hence, observed only at low p_T). Overall, $v_2 \gg v_{k>2}$ and die out for high p_T ; therefore, they will not be addressed in this analysis.

Collision of two Pb nuclei

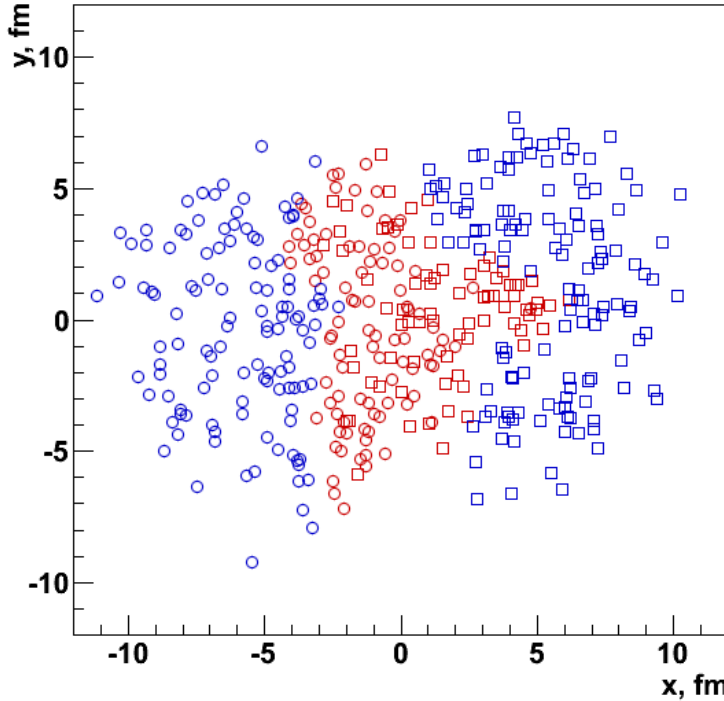


Figure 15: Two colliding Pb nuclei. Different shapes denote nucleons from different nuclei, red and blue colors – participating and non-participating nucleons. Due to local density fluctuations, the colliding region will not be symmetric. The spatial anisotropy will result in different angular expansion in momentum space, giving rise to odd components of flow. Picture taken from the Glauber Monte Carlo simulation, described in sec. 6.1.

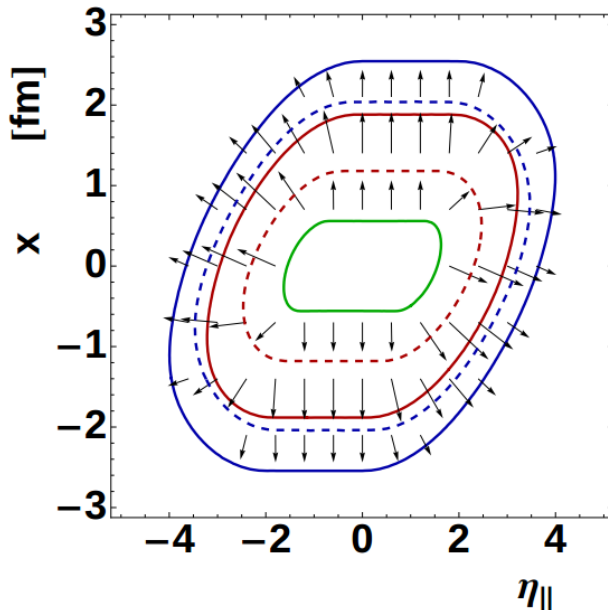


Figure 16: Contour plot of initial pressure created in non-central ($b = 11 \text{ fm}$) AuAu collisions (solid curves) and CuCu collisions (dashed curves). Green, red and blue lines correspond to 9, 3 and 1 GeV/fm^2 pressure respectively. The black lines represent the pressure gradient (in arbitrary units) for AuAu collisions [26].

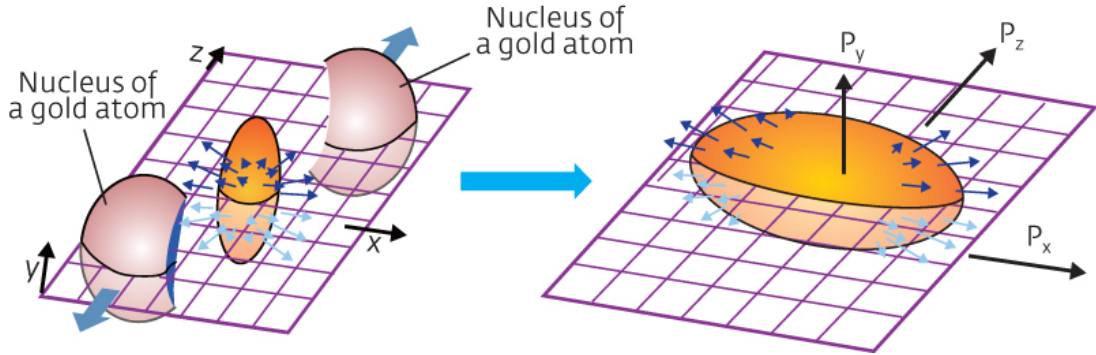


Figure 17: Non-central gold-gold collision. The overlapping (colliding) region exhibits a much higher participant distribution gradient in reaction plane, compared to that of out-of-plane. The spatial anisotropy is then transferred to momentum space, enhancing the p_T of in-plane hadrons [28].

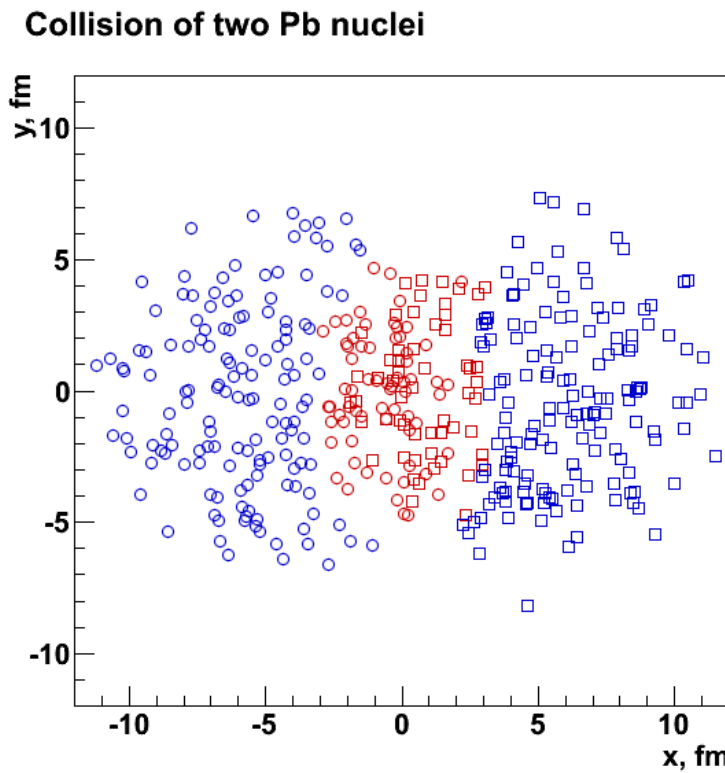


Figure 18: Two colliding Pb nuclei. Different shapes denote nucleons from different nuclei, red and blue colors – participating and non-participating nucleons. In this figure, elliptic shape of participant distribution is seen. Picture taken from the Glauber Monte Carlo simulation, described in sec. 6.1.

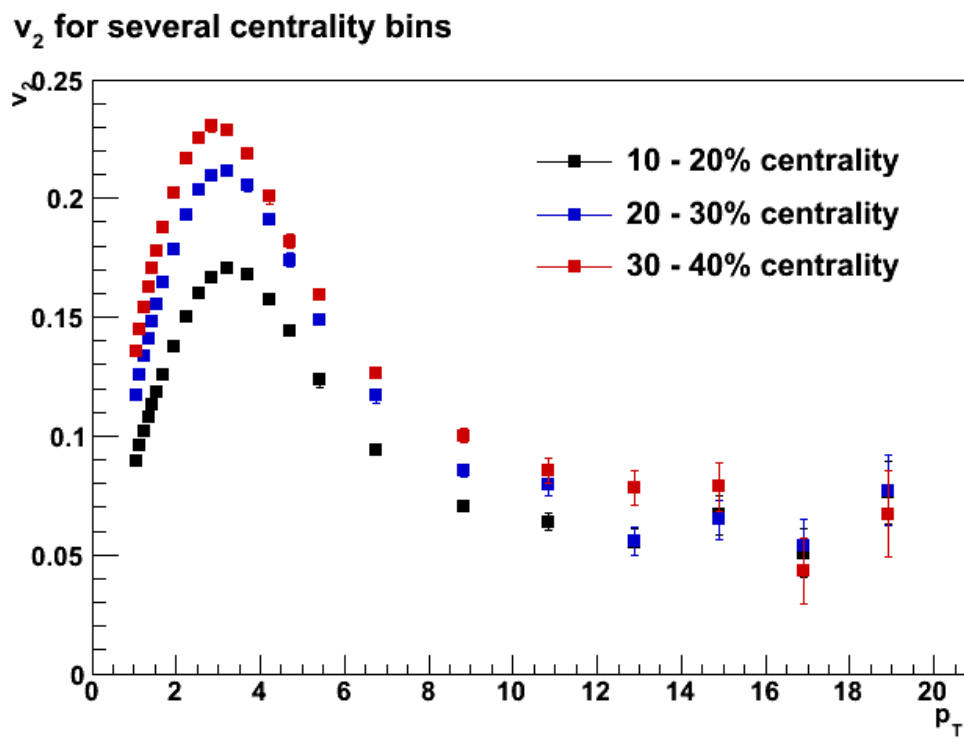


Figure 19: Measured v_2 vs. p_T for PbPb by the ATLAS detector at $\sqrt{s_{NN}} = 2.76\text{GeV}$ for three different centrality bins.

4.4 Jet Quenching

Fig. 20 shows the nuclear modification factor for a p_T range of up to 20 GeV, measured for PbPb collisions at LHC and AuAu collisions at RHIC. It is obvious that R_{AA} is far from 1 in the observed p_T range. The suppression of particle production is usually associated with *quenching* effects.

To put it simple, quenching is a general term used for *colored medium induced energy loss* (as opposed to *flow* which boosts the partons). If a parton is created in a QCD vacuum, e.g. in pp collisions, there is no medium for it to interact with and thus the detected $p_{T,d}$ will be the same as initial $p_{T,i}$ at which it is created.

However, in heavy ion collisions, partons are created in a strongly interacting medium that they have to escape before being detected as particles. As they pass through, they will interact with the surrounding color charge. The parton-medium momentum transfer \vec{q} can be considerably large, thus resulting in a significant fraction of p_T being lost to the medium. The momentum loss will be reflected in the observed particle yield as a shift towards lower p_T values.

There is yet one more feature to be mentioned before moving on. As discussed above, the expanding medium effect will boost the partons towards higher p_T values, while quenching will suppress it. Both of these effects are sensitive to the p_T of a parton: the lowest p_T partons will constitute the medium and will not be effected by quenching, whereas hard (high p_T) partons will be mostly quenched and the flow effects will be significantly lower, if any. Moreover, it should also be noted that at really low p_T one would expect $\langle N_{part} \rangle$ rather than N_{bin} scaling. While the origin of R_{AA} peak around $p_T \approx 3\text{GeV}/c$ in fig. 20 [29] is not completely understood, it is considered to be a result of interplay between flow and quenching.

4.5 In- and out-of-plane nuclear modification factors

Having R_{AA} and v_k defined, one can combine them to produce *in- and out-of-plane nuclear modification factors*, $R_{AA,in/out}$. These quantities are in particular interesting, as the particle production suppression in- and out-of-plane should have the largest asymmetry. Considering only the elliptic flow, from eq. 11 one finds:

$$R_{AA}(\Delta\varphi) = R_{AA}(1 + 2v_2 \cos(2\Delta\varphi)) \quad (13)$$

where $\Delta\varphi = \varphi - \Psi_{RP}$ is the parton emission angle w.r.t. the reaction plane. Clearly, as $\Delta\varphi = 0$, the parton is emitted in the reaction plane. The modification factor then reads:

$$R_{AA,in} = R_{AA}(1 + 2v_2) \quad (14)$$

Similarly, $\Delta\varphi = \frac{\pi}{2}$ is the nuclear modification factor for particles emitted perpendicular to the reaction plane:

$$R_{AA,out} = R_{AA}(1 - 2v_2) \quad (15)$$

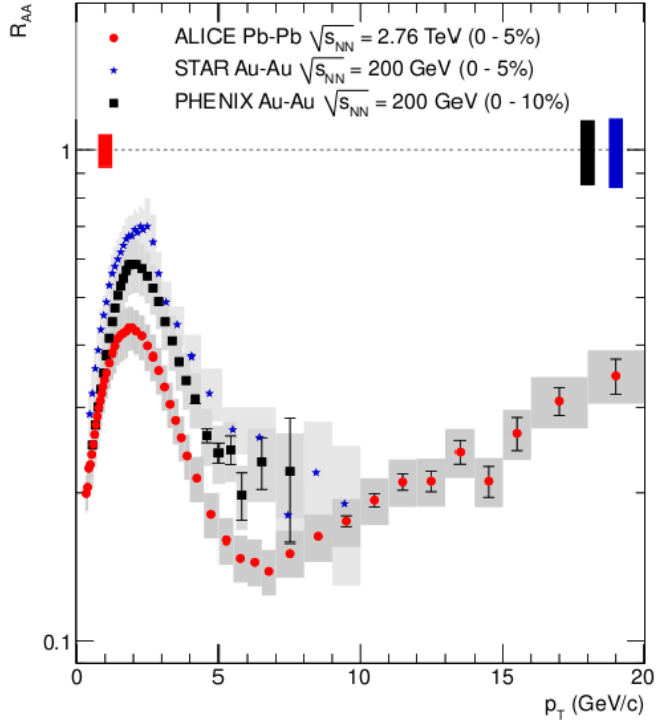


Figure 20: Nuclear modification factor R_{AA} for 5% most central PbPb collisions at $\sqrt{s_{NN}} = 2.76\text{TeV}$ measured by the ALICE detector with comparison to $\sqrt{s_{NN}} = 200\text{GeV}$ AuAu collisions measured at RHIC [29].

Note, that from equations 14 and 15, $R_{AA,in}$ and $R_{AA,out}$ are trivially given by R_{AA} and v_2 and vice versa, therefore, the calculation of quantities $R_{AA,in/out}$ is equivalent to the calculation of observables R_{AA} and v_2 .

As discussed in the previous section, the emerging high p_T particles are expected to see the medium as stationary. On one hand, this would imply that the flow coefficients for these particles should be 0. However, it is not the case: in reality, coefficients v_k describe the angular yield deviations from isotropic emission. At low p_T these deviations are dominated by flow components; on the other hand, due to the fact that the colliding region for non-central collisions is not spherical, the amount of matter an emerging high- p_T parton traverses is also angle-dependent. It is reasonable to assume that the more matter a parton sees, the more quenched it will be. The sensitivity of flow on p_T is clearly reflected in fig. 19: lower p_T particles are greatly affected by the flow, while at higher p_T , flow effects become minute and only (considerably larger) geometrical effects remain. In other words, it is very important to understand that even though v_2 measures the asymmetry of in-plane particle production with respect to out-of-plane, the physics behind this asymmetry for low- and high- p_T particles is very different.

4.6 Energy loss

The main differences between QCD and QED energy losses are caused by the *non-Abelian* nature of QCD [21]. While in electroweak theory the gauge bosons (photons, W and Z) couple only to charged fermions, strong field carriers (gluons) are able to interact with each other as well. Gauge

Table 2: Relative coupling strengths for three QCD vertices [31]

Vertex	Relative coupling strength
$q \leftrightarrow qg$	$\alpha_s C_F = \alpha_s (N_c^2 - 1)/2N_c = 4\alpha_s/3$
$g \leftrightarrow gg$	$\alpha_s C_A = \alpha_s N_c = 3\alpha_s$
$g \leftrightarrow q\bar{q}$	$\alpha_s T_F = \alpha_s/2$

boson interactions give rise to a number of additional loops that have to be accounted for; in fact, for QED, the coefficient $\beta_0 < 0$ in eq. 2 and α_e will *increase* with increasing μ^2 , as compared to the strong coupling constant α_s that will *decrease*. Usually when working with energy losses in QCD, the scale Q , at which α_s is evaluated, has to be considered explicitly [30]. Moreover, there will be three different vertices of quarks and gluons coupling to medium. The relative coupling strengths for all of them are given in table 2 [30, 31]. If one neglects the gluon splitting into quark-antiquark pairs and assumes that the radiated gluon carries a small fraction of the original parton momentum, one finds that the average number of gluons radiated by gluons is higher than that radiated by quarks, i.e. $C_A/C_F = 9/4$.

Radiative energy loss in QCD

Quarks are point-like particles surrounded by a proper field coating – a coherent virtual cloud, consisting of *sea quarks* and gluons. When a hard probe hits the coat, its coherence is broken – constituents are then released from the cloud and observed as the particles accompanying the hard interaction. The harder the hit (larger momentum transfer Q^2), the higher the intensity of radiation [32].

After one large Q^2 scattering, a parton loses a fraction of its coating; before the next irradiation (*bremsstrahlung*), the proper field has to be rebuilt. The typical *formation length* in vacuum, i.e. the length a parton travels while restoring the proper field before the next scattering, can be estimated as the length a virtual particle with momentum $p + k$ travels, see fig. 21. From the uncertainty relation, l_f in the laboratory system is given by [33]:

$$l_f(\omega, \Theta) \sim t_f \sim \frac{\gamma}{M_{virtual}} = \frac{E}{(p+k)^2} \approx \frac{1}{\omega\Theta^2} \approx \frac{k}{k_\perp^2} \quad (16)$$

since $(p+k)^2 \approx 2E\omega(1 - \cos\Theta) \approx E\omega\Theta^2$ for small emission angles Θ , $\omega(k)$ is the radiated gluon energy (momentum) and $E(p)$ is the partons energy (momentum).

For hard partonic scatterings, the typical momentum transfers are given by the Debye screening mass $\mu \propto T$ [33], thus the typical emission angles in eq. 16 are $\Theta^2 = \frac{\mu^2}{\omega^2}$. However, in a medium, not every scattering will result in bremsstrahlung; the average number of radiationless scatterings a parton experiences while coating up is given by $N_s = \frac{l_f}{\lambda}$, where $\lambda \propto T^{-1}$ is the mean free path of a parton in a medium between two scatterings.

The emission angle *in medium* Θ_m^2 then becomes

$$\Theta_m^2 = N_s \Theta^2 = N_s \frac{\mu^2}{\omega^2} \quad (17)$$

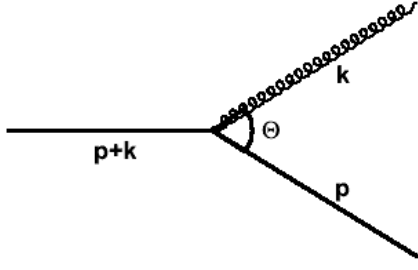


Figure 21: One gluon emission. The formation time of gluon with momentum k can be evaluated as the life-time of a virtual particle with momentum $p + k$.

and substituting it to eq. 16, one gets a formation length in medium:

$$l_f^{med}(\omega) \sim \frac{1}{\omega \Theta_m^2} = \frac{\omega}{N_s \mu^2} = \sqrt{\frac{\omega \lambda}{\mu^2}} \quad (18)$$

and a lower emitted gluon energy limit, $\omega > \lambda \mu^2$, as otherwise the formation length will be shorter than the mean free path and hence the medium will not induce any radiation.

From the expression above, one can obtain the radiated gluon energy spectrum. For a medium of thickness L , the number of emitted gluons of some energy ω is given by:

$$N_e = \frac{L}{l_f^{med}} \sim L \sqrt{\frac{\mu^2}{\lambda \omega}} \quad (19)$$

Differentiating it by ω , one obtains:

$$\frac{dN_e}{d\omega} \propto L \sqrt{\frac{\mu^2}{\lambda}} \omega^{-\frac{3}{2}} \quad (20)$$

and then multiplying by ω yields

$$\omega \frac{dN_e}{d\omega} \propto L \sqrt{\frac{\mu^2}{\lambda \omega}} \quad (21)$$

The *average momentum-transfer per unit length* is defined as:

$$\hat{q} = \frac{\mu^2}{\lambda} \quad (22)$$

which, as the name suggests, denotes the average momentum (squared) transferred from parton to medium per unit length. The highest energy a gluon can obtain is given by eq. 19, assuming that a single gluon is radiated and carries away all the energy available. The upper limit for the ω is then

$$\omega \leq \omega_c = \hat{q} L^2 \quad (23)$$

The average energy lost by a parton traversing the matter is then obtained by integrating eq. 21:

$$\Delta E_{rad} = \int_{\lambda \mu^2}^{\omega_c} (\omega \frac{dN_e}{d\omega}) d\omega \propto \int_{\lambda \mu^2}^{\omega_c} \sqrt{\frac{\omega_c}{\omega}} d\omega = 2(\omega_c - \sqrt{\lambda \mu^2 \omega_c}) \quad (24)$$

Moreover, as $\omega_c \propto L^2$ and for a thick medium $L \gg \lambda$, the second term in the parenthesis of eq. 24 can be dropped to obtain [33]:

$$\Delta E_{rad} \propto \omega_c = \hat{q}L^2 \quad (25)$$

For this analysis it is convenient to rewrite eq. 25 in a slightly different way. As mentioned already, the Debye screening mass is $\mu \propto T$, where T is the temperature of medium. On the other hand, the mean free path $\lambda \propto T^{-1}$. Then using 22:

$$\hat{q} = \frac{\mu^2}{\lambda} \propto T^3 \quad (26)$$

and combining it with eq. 25, one finally arrives at:

$$\Delta E_{rad} \propto T^3 L^2 \quad (27)$$

4.7 QGP density

For analysis purposes, heavy ion collisions are usually classified into centrality bins. Theoretically, centrality is directly related to the impact parameter b and shows how central the collision is: the most central collision is the one with $b = 0$ (centrality = 0%) and yields the highest particle production rate, while the most peripheral one (large b , centrality $\lesssim 100\%$) might result in no particles produced at all. In practice, however, there is no way to measure b , and the centrality is determined by comparing $\frac{dN}{d\eta}$ of all the events: 10% of all the events resulting in highest particle yield will be attributed a 0%-10% centrality bin, the next 10% will be attributed a 10%-20% centrality bin, etc.

Clearly, the most central collisions will have the highest number of participating nucleons and binary collisions. As will be discussed later, the density of QCD matter will also decrease when going from central to peripheral collisions and this will have an effect on the observed R_{AA} . Therefore, if one wants a proper comparison between different centrality bins, one should account for different matter densities as well.

There is yet one more question to answer: which density should one be concerned about: energy, quark, gluon?

Shortly after the production of the QCD medium, gluons come into equilibrium – much faster than quarks do. Therefore, at very short time scales, one can think of QGP as an ideal relativistic gluon gas and neglect the quark contribution¹⁰ [34]. It means that the differences in R_{AA} between centrality bins will be (mostly) induced by the different *gluon* densities n_g . However, there is no way to experimentally measure n_g and thus one has to relate it to an observable $\frac{dN_{ch}}{d\eta}$.

From Maxwell Boltzmann statistics, one has the equation of thermalized QGP state [35, 36]:

$$n_g = \frac{1}{V} \sum_{\vec{p}} e^{-E_{\vec{p}}/T} \quad (28)$$

$$\epsilon = \frac{1}{V} \sum_{\vec{p}} E_{\vec{p}} e^{-E_{\vec{p}}/T} \quad (29)$$

¹⁰See table 2. Also, note that it is a very naive approximation, and in reality one might have a considerable contribution from quarks as well.

$$P = \frac{1}{V} \sum_{\vec{p}} p_x v_x e^{-E_{\vec{p}}/T} \quad (30)$$

Integrating eq.28 - 30, one finds:

$$n_g = \frac{g}{\pi^2 \hbar^3} T^3 \quad (31)$$

$$\epsilon = 3P = 3n_g T = \frac{3g}{\pi^2 \hbar^3} T^4 \quad (32)$$

From eq. 31 and 32 one can see, that

$$n_g \propto \epsilon^{\frac{3}{4}} \quad (33)$$

Now one has to find how to relate ϵ to $\frac{dN_{ch}}{d\eta}$. For that, let us consider a pp collision with particle yield $\frac{dN_{ch}}{d\eta}|_{pp}$ and the average energy a produced particle carries away, $\langle E \rangle$. The total energy radiated per small pseudorapidity window $d\eta$ is then

$$\frac{dE}{d\eta}|_{pp} = \langle E \rangle \frac{dN_{ch}}{d\eta}|_{pp} (1 + K) = \langle E \rangle \frac{dN_{ch}}{d\eta}|_{pp} \left(1 + \frac{N_n}{N_{ch}}\right) \quad (34)$$

where the term in parenthesis of eq. 34 accounts for both neutral (N_n) and charged (N_{ch}) particle production.

If one now considers a heavy ion collision as N subsequent pp collisions, the total energy radiated for some pseudorapidity window $\Delta\eta$ is:

$$E = N \frac{dN_{ch}}{d\eta} \Delta\eta \propto \left(\frac{dN_{ch}}{d\eta} \right)_{AA} \quad (35)$$

The energy density ϵ is then:

$$\epsilon = \frac{E}{S} \propto \frac{1}{S} \left(\frac{dN_{ch}}{d\eta} \right)_{AA} \quad (36)$$

where A is the collision area in the transverse plane of the collision. This was first shown by J. D. Bjorken in [37]. Combining eq. 33 with eq. 36, one can find:

$$n_g \propto \left[\frac{1}{S} \left(\frac{dN_{ch}}{d\eta} \right)_{AA} \right]^{\frac{3}{4}} \quad (37)$$

5 Glauber Model

In reality, it is rather complicated to make a clear distinction between the participating nucleons and spectators. While a pp collision could be described in QFT to some extent, an attempt to do the same for a heavy ion collision would eventually lead to rigorous equations. There is, however, an easy work-around to reproduce the initial state of AA collision, the Glauber model, named after Roy Glauber, who pioneered the quantum mechanical scattering theory for composite systems.

In the Glauber model for inelastic collisions, one assumes two nuclei with number of nucleons A and B positioned according to the Wood-Saxon distribution [38]:

$$\rho_{WS}(r) = \rho_0 \frac{1 + (r/R)^2 \omega}{1 + \exp(\frac{r-R}{a})} \quad (38)$$

where R is the nuclear radius, a is the skin thickness and ω characterizes deviations from a spherical shape. The nucleon density in the center of nucleus, ρ_0 , is basically a normalization constant and thus is not important. The angular part of the distribution is purely flat.

As it will be explained later, nucleons generated for inelastic interactions have their size and position in space well-defined. Hence, there is a small probability for the nucleons, that are in our point of view rigid bodies, to be overlapping. Clearly, one wishes to avoid this situation, therefore, an additional parameter, the *minimum nucleon separation distance* d_{min} , is added. As the name suggests, it is a requirement for all the nucleons in a nucleus to have their centers separated from each other by a distance $d \geq d_{min}$

Two generated nuclei are then assumed to be moving in straight parallel lines, separated by a random impact parameter b . Since inelastic processes are of interest, each of the nucleons is assumed to be a hard sphere with a radius of $R_N = \sqrt{\sigma_{NN}^{inel}/\pi}$, where σ_{NN}^{inel} is the inelastic scattering nucleon-nucleon cross-section. It cannot be calculated from perturbative QCD, however, it can be measured in pp collisions. Moreover, it is assumed that σ_{NN}^{inel} is independent of the number of collisions a nucleon underwent before. Practically, the generated nuclei are projected on a plane, perpendicular to the beam axis, and the nucleons from *different* nuclei are assumed to be interacting if their centres are separated by less than $2r_{NN}$, where

$$r_{NN} = \sqrt{\frac{\sigma_{NN}^{inel}}{\pi}} \quad (39)$$

Two colliding Pb nuclei with impact parameter $b = 8$ and $\sigma_{NN}^{inel} = 64\text{mb}$ are shown in fig. 22. One should also note that σ_{NN}^{inel} is the only non-trivial parameter, relating the simulation to the measured data.

Using the simple logics described above, it is possible to extract event-by-event quantities, like N_{part} , N_{bin} , etc. These will not be discussed here, but rather in chapter 6.1, where the particular Glauber Monte Carlo simulation written for this analysis will be discussed.

PbPb collision with $b = 8\text{fm}$

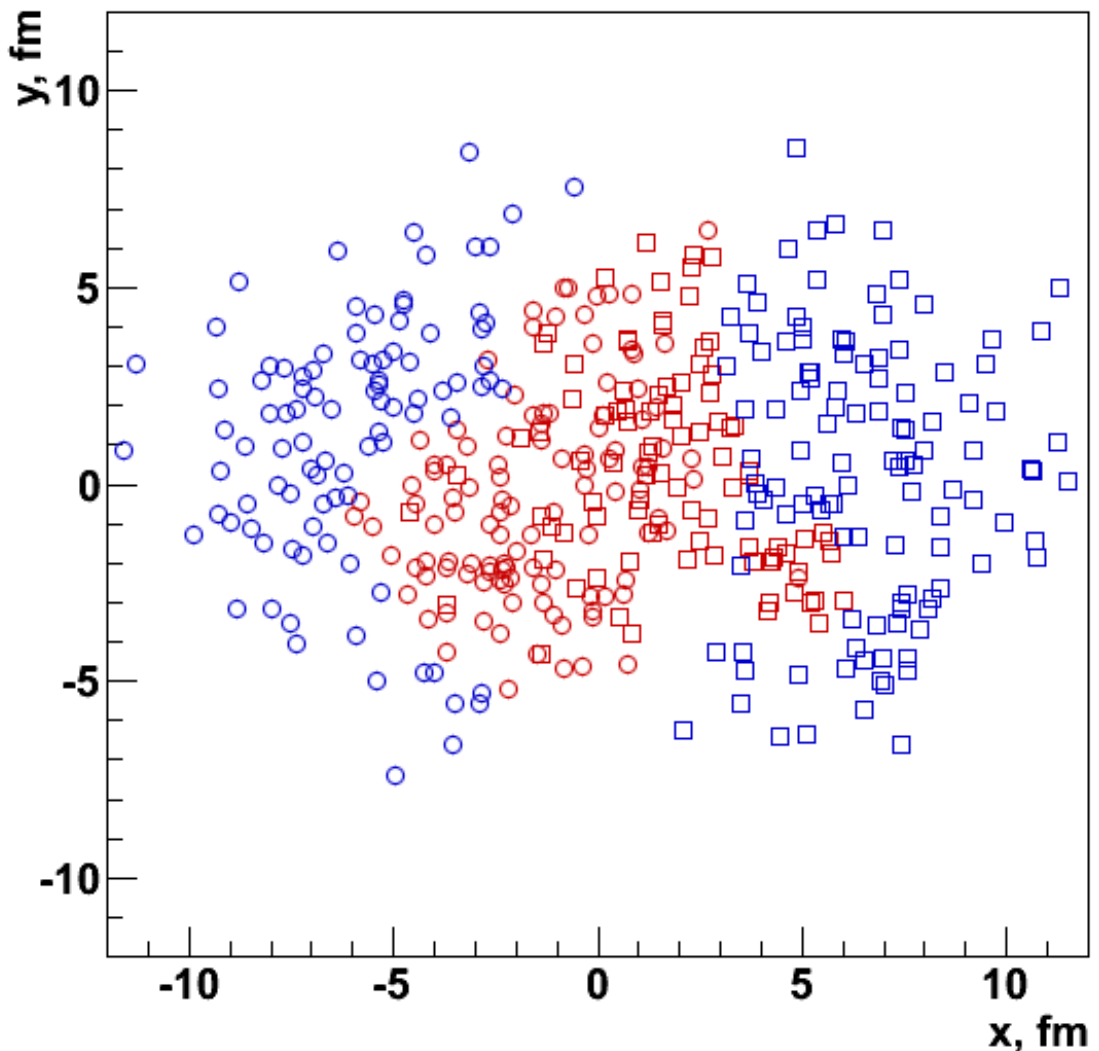


Figure 22: Two colliding Pb nuclei with $b = 8\text{fm}$. Circles and squares represent nucleons from different nuclei, while red and blue colors represent participating and non-participating nucleons respectively. Picture taken from the Glauber Monte Carlo simulation, described in sec. 6.1.

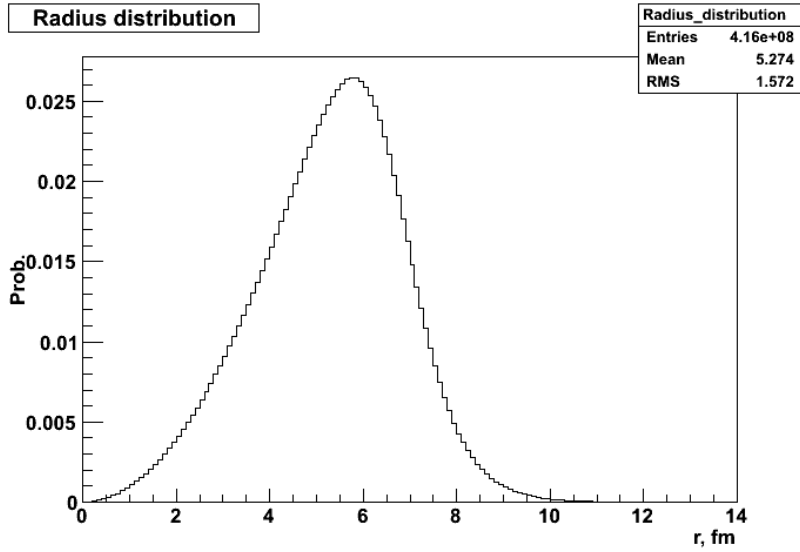


Figure 23: Nucleon radial distribution in a generated Pb nucleus, normalized to 1. Note that as $r \rightarrow 0$, $P(r) \rightarrow 0$ (see the text)

6 Analysis

6.1 Glauber Monte Carlo

As a part of this study, a Glauber Monte Carlo simulation program was written. The input parameters used in this simulation are given in table 3 [39].

The nucleon radial distribution is shown in fig. 23. From eq. 38 for small r one would expect $P(r) \simeq \text{const} \neq 0$, but as it is seen in fig. 23, $P(r) \rightarrow 0$ as $r \rightarrow 0$. This is because the surface on which the nucleon can be placed, $S(r \rightarrow 0) = 4\pi r^2 \rightarrow 0$ and hence it is very improbable to have a nucleon at the center of nucleus.

Overall, 1 000 000 PbPb collisions were generated with a random impact parameter b following the distribution

$$\frac{dP(b)}{db} = C_1 b \quad (40)$$

which can be integrated to find the probability of having b in small window Δb , i.e. $P(b, b + \Delta b)$:

$$P(b, b + \Delta b) = C_1((b + \Delta b)^2 - b^2) \simeq C_2 b \quad (41)$$

Table 3: Glauber model input parameters for PbPb collisions at $\sqrt{s} = 2.76$ TeV, taken from [39]

Input parameter	Value
Atomic number A	208
Nuclear radius R	6.62 fm
Skin thickness a	0.546 fm
Inter-nucleon distance d_{min}	0.4 fm
Non-sphericity ω	0 (Spherical)
Inelastic cross-section σ_{NN}^{inel}	64 mb

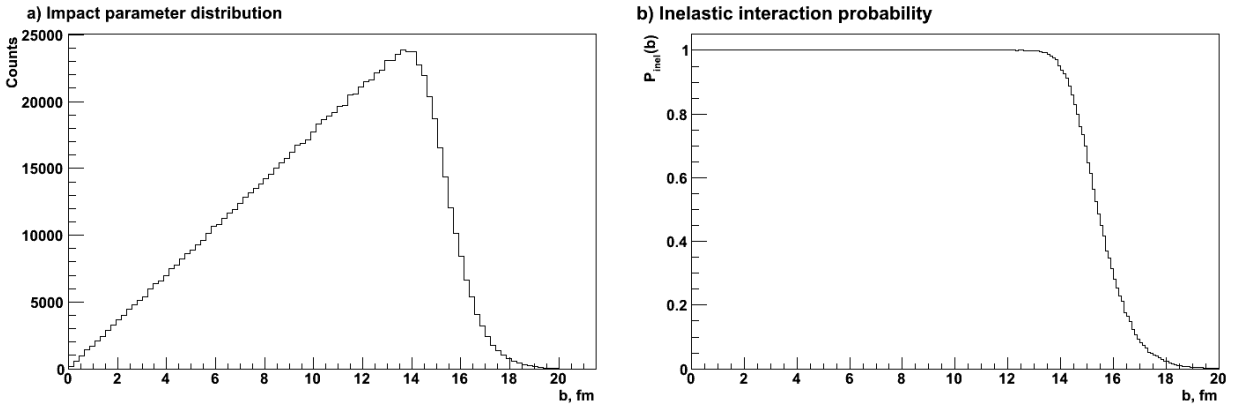


Figure 24: Impact parameter distribution for inelastically colliding events (a) and inelastic interaction probability versus impact parameter (b)

where C_1 and C_2 are normalization constants and thus not important. Distribution of impact parameter of colliding events from the simulation is shown in fig. 24a. Note that from eq. 41, the probability $P(b)$ should increase linearly with b ; however, one sees that at $b \gtrsim 14\text{fm}$, the probability falls down. This is because the inelastic interaction probability falls down for peripheral collisions, see fig. 24b. In this sense, fig. 24a actually represents the *convolution* of *impact parameter distribution* and *inelastic nucleus-nucleus scattering* probability.

Two generated nuclei are displaced by the impact parameter b and then projected on the collision plane, perpendicular to the beam axis z . The resulting collision configuration is then moved into the participant center-of-gravity coordinate system, i.e. $\langle x_N \rangle = \langle y_N \rangle = 0$, where

$$\langle x \rangle = \frac{1}{N_{part}} \sum_i^{N_{part}} x_i \quad (42a)$$

$$\langle y \rangle = \frac{1}{N_{part}} \sum_i^{N_{part}} y_i \quad (42b)$$

are the average coordinates of all the participating nucleons in the collision plane. The reaction plane¹¹ angle is then deduced as:

$$\Psi = \frac{1}{2} \text{atan2}(\langle \sin(2\varphi_p) \rangle, \langle \cos(2\varphi_p) \rangle) + \frac{\pi}{2} \quad (43)$$

where

$$\varphi_p = \text{atan2}(y_p, x_p) \quad (44)$$

and x_p, y_p are the new coordinates in the participant center-of-gravity system.

The colliding system is then rotated by angle Ψ , so that the reaction plane coincides with x axis of coordinate system and the out-of-plane direction coincides with y . The nucleon hitmaps before and after the rotation are shown in fig. 25a and b respectively, the black line in fig. 25a represents the reaction plane.

¹¹From simulation it is also possible to deduce the *event plane*; one could have used it instead of reaction plane, but as it is not an experimentally measurable quantity, it would not result in an equivalent comparison with the real data.

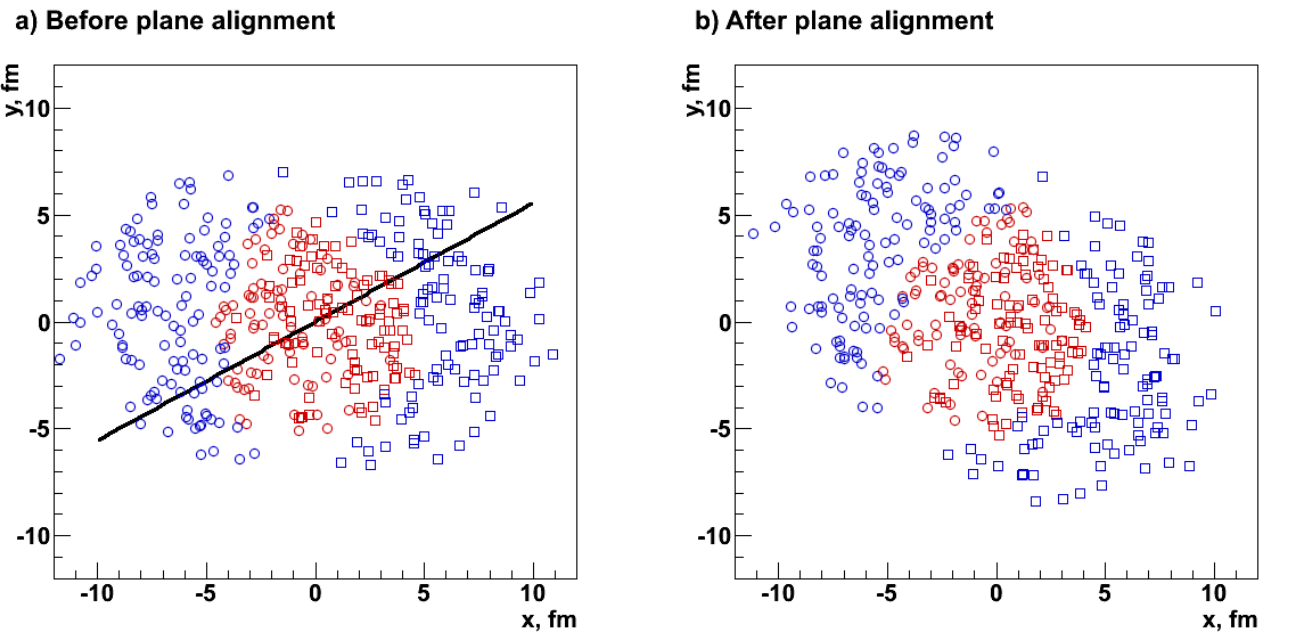


Figure 25: Two colliding Pb nuclei with $b = 8\text{fm}$ before the reaction plane alignment (a) and after (b). Circles and squares represent nucleons from different nuclei, while red and blue colors represent participating and non-participating nucleons respectively. The black line in (a) shows the reaction plane angle.

From each event, quantities N_{part} , N_{bin} , $\langle x_{part}^2 \rangle$, $\langle y_{part}^2 \rangle$, Ψ , b and several others are recorded into a file for further analysis. In this case, however, only $\langle x_{part}^2 \rangle$ and $\langle y_{part}^2 \rangle$ will be of interest, since (as will be shown in just a moment) these quantities represent, or rather are proportional to the lengths a created parton travels in a QCD matter.

For simplicity, let us consider partons moving completely in-plane. Nucleon in-plane (x) distribution for events with $130 < N_{part} < 140$ is given in fig. 26. If a pair of back-to-back partons is created at some arbitrary x_c , one of them will be moving to positive x direction and escaping the QCD matter after having traveled length L_{x+} , while the other one will be traveling length L_{x-} towards negative x direction. The total distance the two partons pass, $L_{coll} = L_{x+} + L_{x-}$, will be the same no matter where the pair is created. This length L_{coll} corresponds to the width of the colliding region in-plane and is characterized by the spread of distribution:

$$L_{coll} \propto \sigma_x = \sqrt{\langle x^2 \rangle - \langle x \rangle^2} \quad (45)$$

However, recall that the colliding system is moved to its participant center-of-gravity coordinates, thus $\langle x \rangle = 0$ and the length a parton has to travel in-plane before escaping the colliding region is:

$$L_{in} \propto L_{in}^{characteristic} = \sigma_x = \sqrt{\langle x^2 \rangle} \quad (46)$$

Applying the same logics for partons created in out-of-plane direction, one finds:

$$L_{out} \propto L_{out}^{characteristic} = \sigma_y = \sqrt{\langle y^2 \rangle} \quad (47)$$

Note that L_{in} and L_{out} are event-by-event quantities, hence to combine with the data segmentation¹², they have to be averaged over all the events under a specific centrality bin (see below). From

¹²The measured data is averaged over a number of events and classified into centrality bins

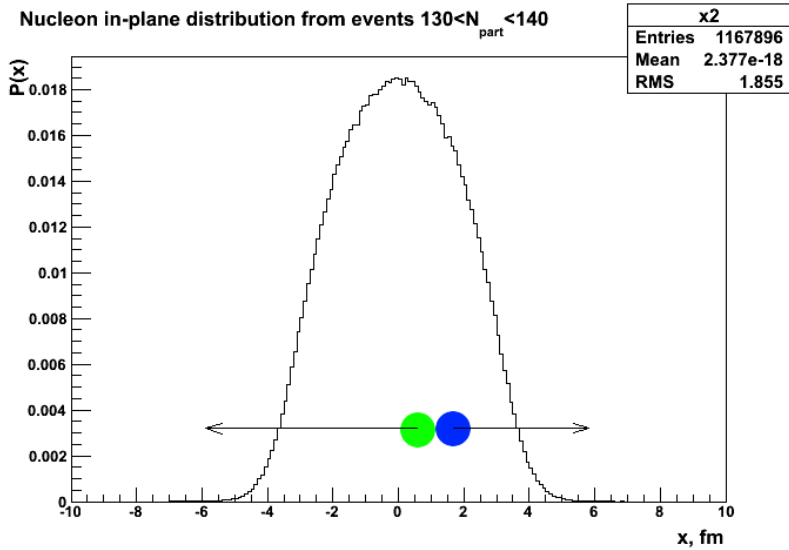


Figure 26: Nucleon in-plane distribution for events with $130 < N_{part} < 140$, normalized to 1

now on, only *bin-averaged characteristic lengths* will be discussed and thus the upper index and the averaging sign will be dropped.

Next step is to classify all the events into 10% centrality bins starting from the most central (0%) up to 80%. This particular binning is chosen to match the binning of the experimental data. For reference, quantities $\langle N_{part} \rangle$, $\langle N_{bin} \rangle$, and impact parameter b range for each centrality bin are given in Appendix B. The nucleon distributions in collision plane are then plotted for all the bins. Interestingly enough, one can notice, that in some centrality bins, the characteristic length in-plane, L_{in} , is rather similar to L_{out} in some other centrality bins. One of these cases is shown in fig. 27. L_{in} in 10%-20% centrality bin (fig. 27b) is rather similar to L_{out} in 30%-40% cent. bin (fig. 27d). To show this explicitly, participant distribution in-plane for 10%-20% and out-of-plane for 30%-40% are plotted in fig. 28. Clearly, the shapes of these distributions are very similar. Therefore, one would expect that the QGP effects on the partons traveling in these directions should be roughly the same, that is, $R_{AA,in}^{10\%-20\%} \approx R_{AA,out}^{30\%-40\%}$. This is a very naive expectation, however, as the different matter densities are not yet accounted for; moreover, it should only be applicable for high- p_T partons, where the flow effects should be negligible.

Next, one can try to find if there are more cases where L_{in} under one centrality bin would be similar to L_{out} under some other bin. For this, L_{in} and L_{out} are plotted vs. centrality, see fig. 29. Eventually one finds five sets of centrality bins that have $L_{in}^{low} \approx L_{out}^{high}$. Table 4 summarizes centrality sets with similar characteristic lengths. Later these particular sets will be used to compare the in- and out-of-plane nuclear modification factors.

Finally, as a cross-check with experimental data, one can directly calculate the inelastic interaction cross-section for PbPb collisions at $\sqrt{s_{NN}} = 2.76\text{GeV}$ from the simulation. An arbitrary large upper limit is set for impact parameter, $b_{max} > R_1 + R_2$ (where R_1 , R_2 are the radii of colliding nuclei), that draws a disk with area

$$S_{max} = \pi^2 b_{max} \quad (48)$$

around one (*target*) nucleus, see fig. 30. The second nucleus (*projectile*) is placed on this disk following

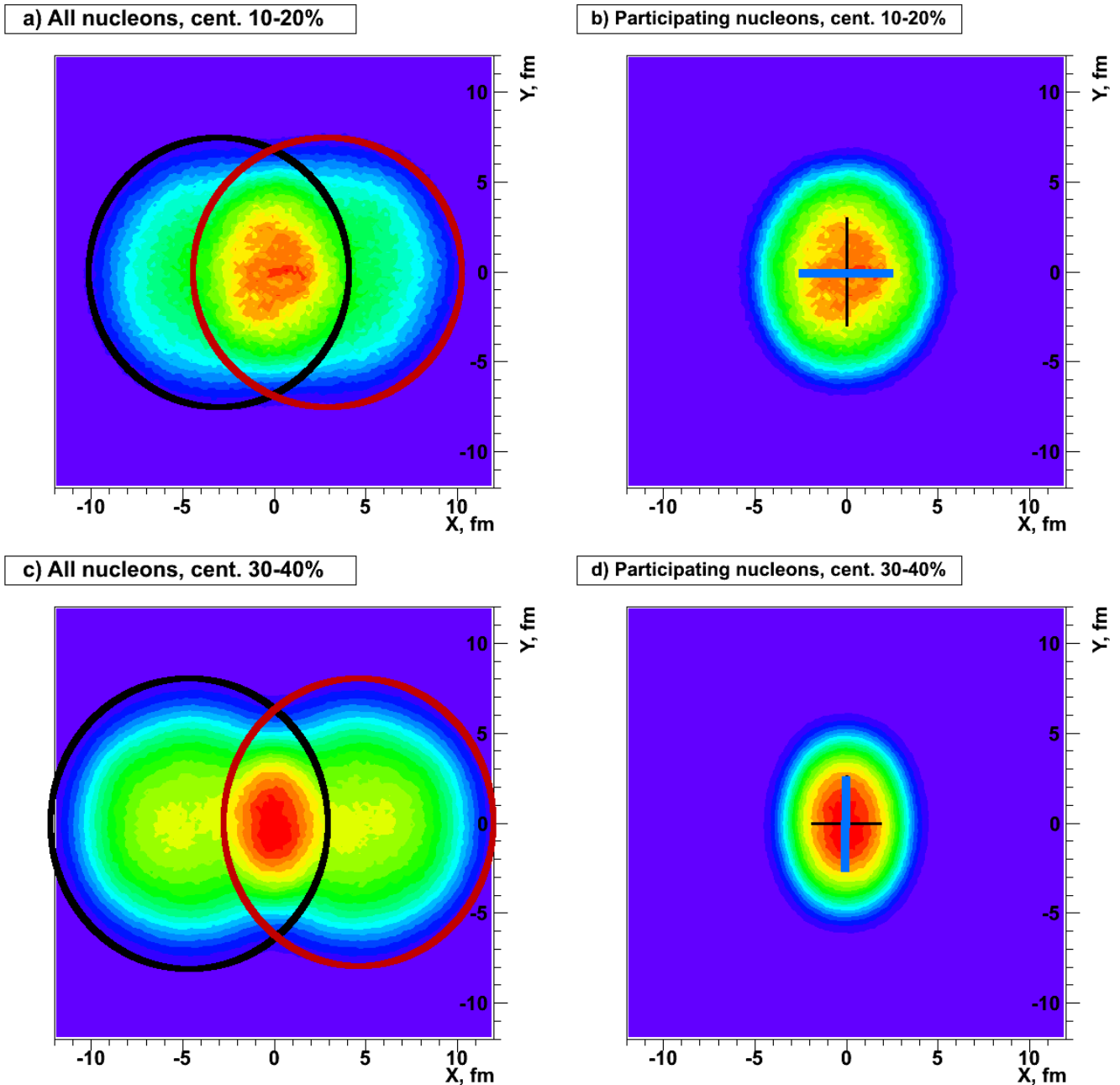


Figure 27: All nucleon distributions in 10%-20% and 30%-40% centrality bins (a, c) and participant-only (b, d). Thick blue lines in c and d are the characteristic lengths (L_{in} in c and L_{out} in d), that are rather similar.

Table 4: Sets of centrality bins with $L_{in}^{low} \approx L_{out}^{high}$

Lower cent. bin	L_{in}^{low} , fm	Higher cent. bin	L_{out}^{high} , fm
0% - 10%	2.84	10% - 20%	2.93
10% - 20%	2.46	30% - 40%	2.58
20% - 30%	2.11	50% - 60%	2.12
30% - 40%	1.82	60% - 70%	2.04
40% - 50%	1.56	70% - 80%	1.79

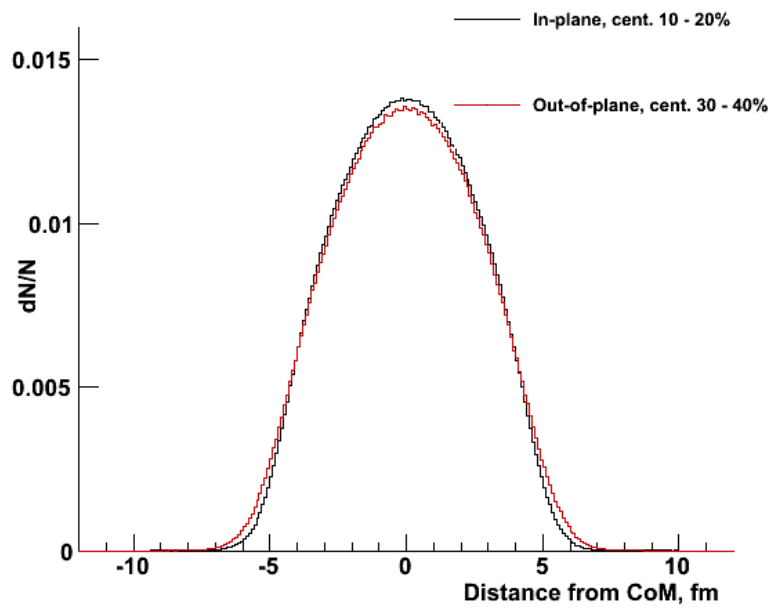


Figure 28: Participant distribution in-plane for 10%-20% cent. bin (black line) and out-of-plane for 30%-40% cent. bin (red line), both normalized to 1.

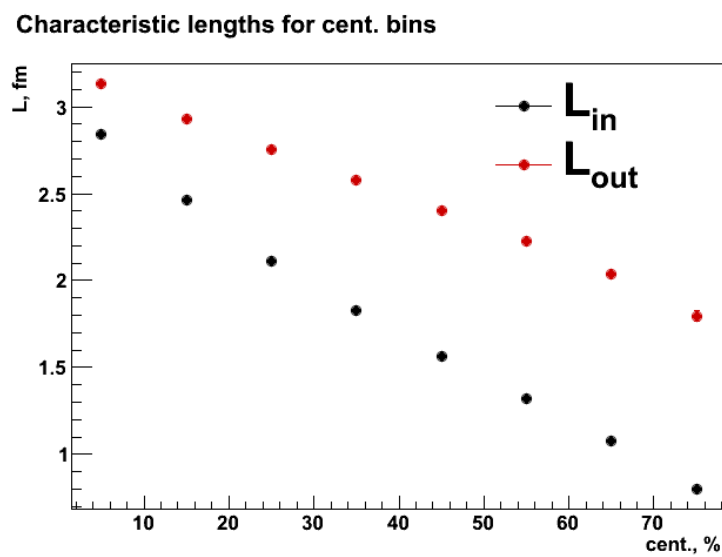


Figure 29: Characteristic in- and out-of-plane lengths, L_{in} and L_{out} , vs. centrality.

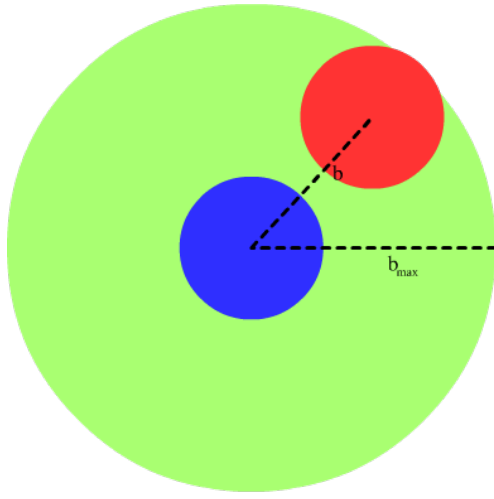


Figure 30: The upper limit of impact parameter, b_{max} draws a disc (green) around target nucleus (blue), on which the projectile nucleus (red) is placed.

the distribution, given by eq. 40. Depending on the actual impact parameter in each event, the projectile might either hit the target ($N_{part} > 0$) or miss it ($N_{part} = 0$). There are N_t events, out of which N_h result in a hit, the inelastic interaction cross-section can be calculated as

$$\frac{N_h}{N_t} = \frac{\sigma_{inel}}{\pi^2 b_{max}} \quad \Rightarrow \quad \sigma_{inel} = \frac{N_h}{N_t} \pi^2 b_{max} \quad (49)$$

6.2 Combining v_2 and R_{AA}

To produce the in- and out-of-plane nuclear modification factors, ATLAS v_2 [13] and ALICE R_{AA} [40] data are combined. CMS data could have been used instead, as they have measured both observables, however, the segmentation of their data is much coarser in both centrality and p_T .

The first step to combine ALICE and ATLAS data is to find a corresponding R_{AA} for each v_2 . ALICE and ATLAS data have different p_T binning as well, but the differences between the bins are rather small. Therefore, to combine the data, for each v_2 , R_{AA} with closest p_T to that of v_2 was matched. The p_T mismatch, i.e. $p_{T,ALICE} - p_{T,ATLAS}$ vs. $p_{T,ATLAS}$ is shown in fig. 31. Apparently, the highest mismatch is $|\Delta p_T(p_{T,ATLAS} \approx 15\text{GeV}/c)| \approx 0.4\text{GeV}/c$, which is still reasonably small, given that the curves are rather smooth and slowly varying.

Eq. 14 and 15 are then used to calculate $R_{AA,in/out}$. All the values of p_T , R_{AA} , v_2 used to calculate $R_{AA,in}$ and $R_{AA,out}$ are given in Appendix C. At this point one should keep in mind that though the lengths are (approximately) the same, the absolute matter densities a parton sees along its way are not. A higher density of matter could result in a parton being quenched more, which would be observed as a suppression of particle production at high- p_T .

6.3 Density Effects

The different densities ρ of created QCD matter might influence the observed $R_{AA,in}$ and $R_{AA,out}$: even though $L_{in}^{\rho_1} \approx L_{out}^{\rho_2}$ (with $\rho_1 > \rho_2$), one might still have $R_{AA,in}(\rho_1) \not\approx R_{AA,out}(\rho_2)$. Hence

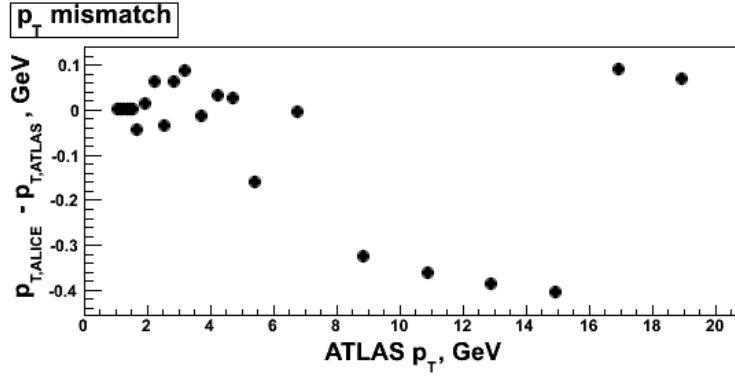


Figure 31: $\Delta p_T = p_{T,ALICE} - p_{T,ATLAS}$ vs. $p_{T,ATLAS}$. The highest mismatch is for ATLAS $p_T \approx 15\text{GeV}/c$ and is around $0.4\text{GeV}/c$, which is still reasonably small.

to make a more proper comparison, one of the R_{AA} has to be *rescaled* to the other's density, i.e. $R_{AA,in}^{rescaled} = R_{AA,in}(\rho_1 \rightarrow \rho_2)$. How can this be done?

As discussed in section 4.7, one can think of QGP as an ideal relativistic gluon gas. The area in eq. 37 can be written as:

$$S = KL_{in}L_{out} \quad (50)$$

where the proportionality constant K is the same for all the centrality bins, and thus gluon density (for i -th cent. bin) reads:

$$n_g^{(i)} \propto \left[\frac{1}{L_{in}^{(i)} L_{out}^{(i)}} \left(\frac{dN_{ch}}{d\eta} \right)_{AA}^{(i)} \right]^{\frac{3}{4}} \quad (51)$$

For each of $R_{AA,in/out}$ sets the gluon density of more central bin, $n_{g,c}$, is normalized to that of more peripheral, $n_{g,p}$. The ratio of the densities is:

$$C = \frac{n_{g,c}}{n_{g,p}} = \left[\frac{(L_{in}L_{out})_p}{(L_{in}L_{out})_c} \left(\frac{dN_{ch}}{d\eta} \right)_c \right]^{\frac{3}{4}} \approx \left[\frac{L_{in,p}}{L_{out,c}} \frac{\left(\frac{dN_{ch}}{d\eta} \right)_c}{\left(\frac{dN_{ch}}{d\eta} \right)_p} \right]^{\frac{3}{4}} \quad (52)$$

since $L_{out,p} \approx L_{in,c}$. How should this ratio be included in R_{AA} ?

Let us first consider the invariant charged particle yield in pp collisions, see fig. 32 [41]. With a good agreement, it can be parametrized as a power law:

$$y_{pp}(p_T) = ap_T^\chi \quad (53)$$

Parametrization powers χ obtained from LHC [41] and RHIC [42] data are:

$$\chi_{LHC} = -6.54 \quad (54a)$$

$$\chi_{RHIC} = -8.13 \quad (54b)$$

In heavy ion collisions, for some $p_{T,1}$ the measured invariant yield is:

$$y_{AA}(p_{T,1}) = R_{AA}y_{pp}(p_{T,1}) = y_{pp}(p_{T,0}) \quad (55)$$

It is now assumed that in AA collisions, a parton is created with some initial transverse momentum $p_{T,0}$. It then travels through matter losing a fraction of its momentum, $\Delta p_T = p_{T,0} - p_{T,1}$ until

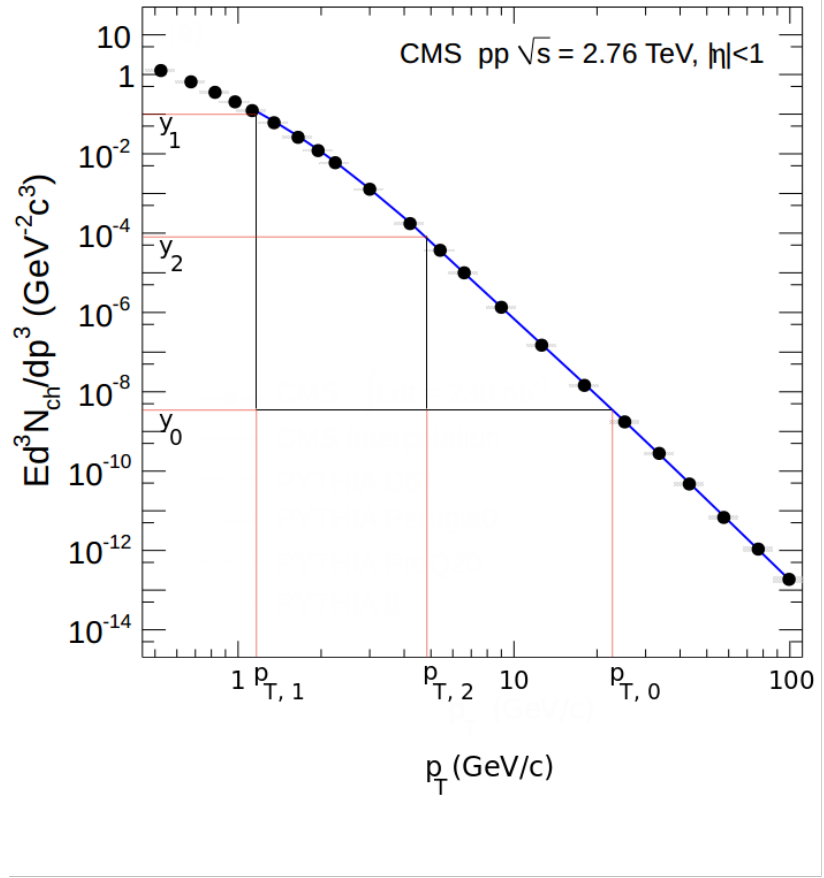


Figure 32: Invariant charged particle yield in pp collisions vs. transverse momentum [41]. The plot is purely explanatory, thus arbitrary scaling factors for Δp_T as well as for AA yield were used.

eventually it is detected with $p_{T,1}$. From equations 27 and 31, one can see that $\Delta p_T \propto n_g L^2$. To calculate the expected energy loss for some other density $n_{g,new}$, n_g is simply replaced with $n_{g,new} = \frac{n_g}{C}$, where $C = \frac{n_g}{n_{g,new}}$ can be calculated using eq. 52. Since

$$\Delta p_T = p_{T,0} - p_{T,1} \propto n_g = C n_{g,new} \quad (56)$$

one finds

$$\Delta p_{T,new} = p_{T,0} - p_{T,2} = \frac{\Delta p_T}{C} \propto n_{g,new} \quad (57)$$

Using eq. 53 - 57, it can be summarized:

$$y_1 = ap_{T,1}^\chi \quad (58a)$$

$$y_0 = ap_{T,0}^\chi = R_{AA} y_1 = R_{AA} ap_{T,1}^\chi \quad (58b)$$

$$p_{T,0} = R_{AA}^{\frac{1}{\chi}} p_{T,1} \quad (58c)$$

$$y_2 = ap_{T,2}^\chi \quad (58d)$$

Next, one can use eq. 57 to write:

$$p_{T,2} = p_{T,0} - \Delta p_{T,new} = p_{T,0} - \frac{p_{T,0} - p_{T,1}}{C} \quad (59)$$

Substituting eq. 58c yields:

$$p_{T,2} = p_{T,1} \left(R_{AA}^{\frac{1}{\chi}} - \frac{R_{AA}^{\frac{1}{\chi}} - 1}{C} \right) \quad (60)$$

and thus by definition

$$R_{AA,new} = \frac{y_0}{y_2} = \frac{R_{AA} ap_{T,1}^\chi}{ap_{T,2}^\chi} = \frac{C^\chi R_{AA}}{\left(1 + R_{AA}^{\frac{1}{\chi}} (C - 1) \right)^\chi} \quad (61)$$

The density ratios are calculated using eq. 52, they are presented in table 5.

An important thing to remember is that so far it was assumed that a parton of transverse momentum p_T always loses some mean energy Δp_T . In reality, the energy loss is not a constant, but

Table 5: Correction factor C for centrality sets with $L_{in,c} \approx L_{out,p}$

More central bin	More peripheral bin	Ratio C
0% - 10%	10% - 20%	1.11
10% - 20%	30% - 40%	1.18
20% - 30%	50% - 60%	1.43
30% - 40%	60% - 70%	1.50
40% - 50%	70% - 80%	1.58

rather a random quantity; hence, one should also take into account Δp_T distribution and fluctuations. On the other hand, as the aim is a simple picture, this effect will not be taken into account in this thesis.

In general, one does not have to limit oneself to eq. 33. Instead, the power κ in eq. 62 will be tuned to see if a better agreement for $R_{AA,in/out}$ can be obtained.

$$\rho \propto \epsilon^\kappa \quad (62)$$

If one finds that $\kappa \not\approx \frac{3}{4}$, that could suggest either that the radiative energy losses do not scale with n_g ($\rho \Rightarrow n_g$ for $\kappa = \frac{3}{4}$), or that the contribution of gluon density is reduced due to the flow.

Once a proper scaling relation (eq. 62) is established, one can scale down all the centrality bins to one particular density ρ_k using eq. 61 with density-ratio

$$C_i = \frac{\rho_i}{\rho_k} \quad (63)$$

In such a framework one would expect to eliminate $R_{AA,in/out}$ variations caused by both flow and density. Then the resulting $R_{AA,in/out}$ could be trivially defined as some arbitrary function of L .

6.4 From R_{AA} to energy-loss and back

Following the same idea explained in the previous chapter, one can find a general expression for the relative radiational energy loss:

$$\frac{\Delta p_T}{p_{T,0}} = \frac{p_{T,0} - p_{T,1}}{p_{T,0}} = 1 - R_{AA}^{-\frac{1}{\chi}} \quad (64)$$

where initial and final p_T in the numerator are swapped to get a positive sign, and eq. 58c is used for the second equality. Note that for density-scaled energy loss, R_{AA} is replaced with $R_{AA,sca}$:

$$\frac{(\Delta p_T)_{sca}}{p_{T,0}} = \frac{p_{T,0} - p_{T,2}}{p_{T,0}} = 1 - R_{AA,sca}^{-\frac{1}{\chi}} \quad (65)$$

Parametrizing the energy loss curve as

$$\frac{(\Delta p_T)_{sca}}{p_{T,0}} = f(L) \quad (66)$$

one can solve eq. 65 to find $R_{AA,sca}$ for some arbitrary L :

$$R_{AA,sca} = (1 - f(L))^{-\chi} \quad (67)$$

To get back to density-unscaled R_{AA} , one can either use eq. 61 or modify eq. 67 slightly:

$$f(L) = \frac{p_{T,0} - p_{T,2}}{p_{T,0}} = \frac{1}{p_{T,0}} \frac{p_{T,0} - p_{T,1}}{C} \Rightarrow \frac{p_{T,0} - p_{T,1}}{p_{T,0}} = Cf(L) \quad (68)$$

and therefore:

$$R_{AA} = (1 - Cf(L))^{-\chi} \quad (69)$$

Note that once (if) the $f(L)$ curve is established, the R_{AA} is given just by L :

$$R_{AA,in} = (1 - Cf(L_{in}))^{-\chi} \quad (70a)$$

$$R_{AA,out} = (1 - Cf(L_{out}))^{-\chi} \quad (70b)$$

Eventually, one can work out the experimentally measurable quantities, v_2 and R_{AA} . From equations 14 and 15:

$$k = \frac{R_{AA,in}}{R_{AA,out}} = \frac{1 + 2v_2}{1 - 2v_2} \quad (71)$$

and thus

$$v_2 = \frac{k - 1}{2(k + 1)} \quad (72a)$$

$$R_{AA} = R_{AA,in} \frac{k + 1}{2k} = R_{AA,out} \frac{k + 1}{2} \quad (72b)$$

Several remarks at this point: first of all, it is not known how ΔE , prescribed by eq. 27, scales with partons' p_T . In general, the parametrization $f(L)$ in eq. 66 should then also be a function of p_T . On the other hand, the charged particle yield $y(p_T)$ is a steeply falling function (see fig. 32), hence for any given transverse momentum bin, observed R_{AA} and v_2 will be biased by the lowest p_T available.

Also, note that it is (presumably) the parton that loses energy while traversing the matter, while the measurable quantity, $\frac{dN_{ch}}{d\eta}$, results from its fragments.

6.5 Rescaling to Gold-Gold collisions at RHIC

Finally, there is no reason why energy loss scaling should fail when going to a different system. That is, eq. 66 is *unique* for density ρ_f . If one can scale any system to $\rho \rightarrow \rho_f$, one expects the very same energy loss parametrization curve $f(L)$. To check if this scaling works, R_{AA} and v_2 for AuAu collisions at $\sqrt{s_{NN}} = 200\text{GeV}$ are calculated and compared with measured PHENIX data [43].

First, a Glauber Monte Carlo simulation is performed for AuAu collisions with parameters given in table 6 [44]. As for the PbPb case, 1 000 000 collision events are generated, and characteristic lengths $L_{in/out}$ extracted. Charged particle multiplicity $\left(\frac{dN_{ch}}{d\eta}\right)_{AuAu}$ is calculated combining LHC data [45] with $\langle N_{part} \rangle$, extracted from MC simulation. N_{part} , N_{bin} and impact parameter values are given in Appendix B. Density ratios C_i are then calculated using eq. 63 w.r.t. ρ_k , for which $\frac{\Delta\rho_T}{p_T} = f(L)$ has been parametrized. Finally, equations 70 and 72 are used to work out the expected values for observables R_{AA} and v_2 .

All the characteristic lengths $L_{in/out}$ and $\frac{dN_{ch}}{d\eta}$ data used for this analysis for both PbPb and AuAu collisions are given in table 7.

Table 6: Glauber model input parameters for AuAu collisions at $\sqrt{s_{NN}} = 200\text{GeV}$ [44]

Input parameter	Value
Atomic number A	197
Nuclear radius R	6.38 fm
Skin thickness a	0.535 fm
Inter-nucleon distance d_{min}	0.4 fm
Non-sphericity ω	0 (Spherical)
Inelastic cross-section σ_{NN}^{inel}	42 mb

Table 7: Characteristic lengths and charged particle multiplicity data [45] used in the analysis

Cent. bin	PbPb			AuAu		
	L_{in}, fm	L_{out}, fm	$dN_{ch}/d\eta$	L_{in}, fm	L_{out}, fm	$dN_{ch}/d\eta$
0%-10%	2.84	3.13	1522	2.67	2.97	685
10%-20%	2.46	2.93	971	2.27	2.77	428
20%-30%	2.11	2.76	658	1.94	2.60	287
30%-40%	1.82	2.58	432	1.66	2.43	187
40%-50%	1.56	2.40	265	1.43	2.26	114
50%-60%	1.32	2.22	155	1.20	2.10	66
60%-70%	1.08	2.04	80	0.97	1.93	34
70%-80%	0.80	1.80	36	0.71	1.70	16

7 Results

To begin with, the validity of our Glauber Monte Carlo simulation is checked. The inelastic scattering cross-section for PbPb at $\sqrt{s_{NN}} = 2.76\text{TeV}$ and AuAu at $\sqrt{s_{NN}} = 200\text{GeV}$ is calculated using eq. 49. The resulting cross-sections are:

$$\sigma_{inel}^{PbPb} = 7625 \pm 8\text{mb}$$

$$\sigma_{inel}^{AuAu} = 6812 \pm 10\text{mb}$$

where the errors are purely statistical. The results are in a good agreement with calculations by other authors [46, 47].

Next, $R_{AA,in/out}$ is compared for centrality bins given in table 4. It is not known *a priori* how big the QCD matter density effects are, hence at first they are not accounted for. The resulting plots are given in fig. 33.

Apparently, in all the centrality bin sets the $R_{AA,in}$ is somewhat lower than $R_{AA,out}$. This suggests that the different parton quenching strengths, induced by different matter densities, are not negligible and should be accounted for.

$R_{AA,in}$ is then rescaled to the densities of corresponding $R_{AA,out}$, using eq. 61 and ratios presented in table 5. Recall, that for the moment *gluon density* n_g is considered as a proper density of scattering centres in QCD matter, i.e. $\kappa = \frac{3}{4}$ in eq. 62. The comparisons of density-scaled $R_{AA,in}$ with $R_{AA,out}$ are shown in fig. 34.

Although after density scaling $R_{AA,in/out}$ correspondance is slightly better, $R_{AA,in}$ is clearly overestimated, possibly due to scaled-up flow effects [48]: expanding medium causes a lower energy loss of a parton, thus the invariant charged particle yield (fig. 32) in AA collisions is shifted towards higher p_T values. This results in more particles of given momentum p_T , and thus higher R_{AA} . Moreover, as will be seen later, the energy loss for $\rho \propto \epsilon^{\frac{3}{4}}$ scaling, $\frac{\Delta p_T}{p_T}(L=0) \neq 0$, which clearly suggests that such a scaling does not work. Nevertheless, results from fig. 34 are consistent with density-unnormalized R_{AA} : by normalizing the densities, the magnitude of jet-quenching is scaled; however, the residual flow effects are not eliminated, and might still be present for more central cases. Yet it is rather interesting, that the magnitude is maintained.

Eventually, κ is tuned to see, if one can get a better match of $R_{AA,in/out}$. One finds that using $\kappa = \frac{1}{2}$ results in a very good agreement for all but the most peripheral centrality bin, see fig. 35. On the other hand, considering the large error bars for the most peripheral collisions, this set cannot be taken seriously.

The next step in the analysis is to normalize all the $R_{AA,in/out}$ to one common density ρ_k . To avoid scaling up the errors, the normalization is done to the lowest available density, $\rho_{70\%-80\%}$. Ratios of the densities, $C_i = \frac{\rho_i}{\rho_{70\%-80\%}}$, for all the centrality bins are given in fig. 36.

The scaled $R_{AA,in/out}$ are then plotted versus the characteristic lengths, $L_{in/out}$, see fig. 37. For all but the most peripheral collisions, $R_{AA,in/out}$ align into one curve and there are no discrete steps. One can therefore conclude that, for a given p_T in the framework of this analysis, the differences between the in- and out-of-plane nuclear modification factors are given *only* by the different lengths a parton has to traverse in QCD matter.

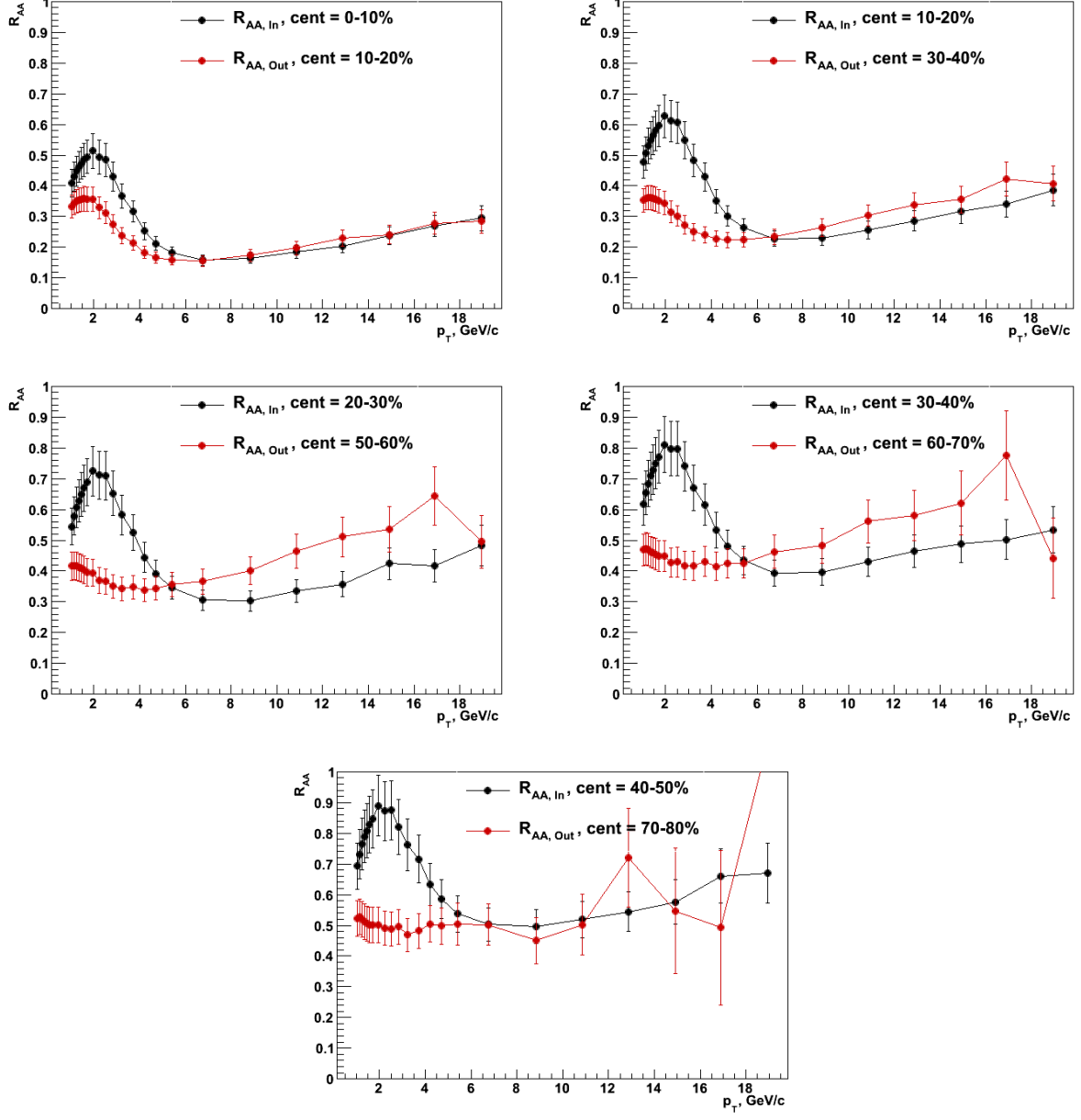


Figure 33: $R_{AA,in}$ and $R_{AA,out}$ vs. p_T for centrality sets, where $L_{in}^{low} \approx L_{out}^{high}$. One would expect $R_{AA,in}(p_T \gtrsim 10\text{GeV}) \sim R_{AA,out}(p_T \gtrsim 10\text{GeV})$.

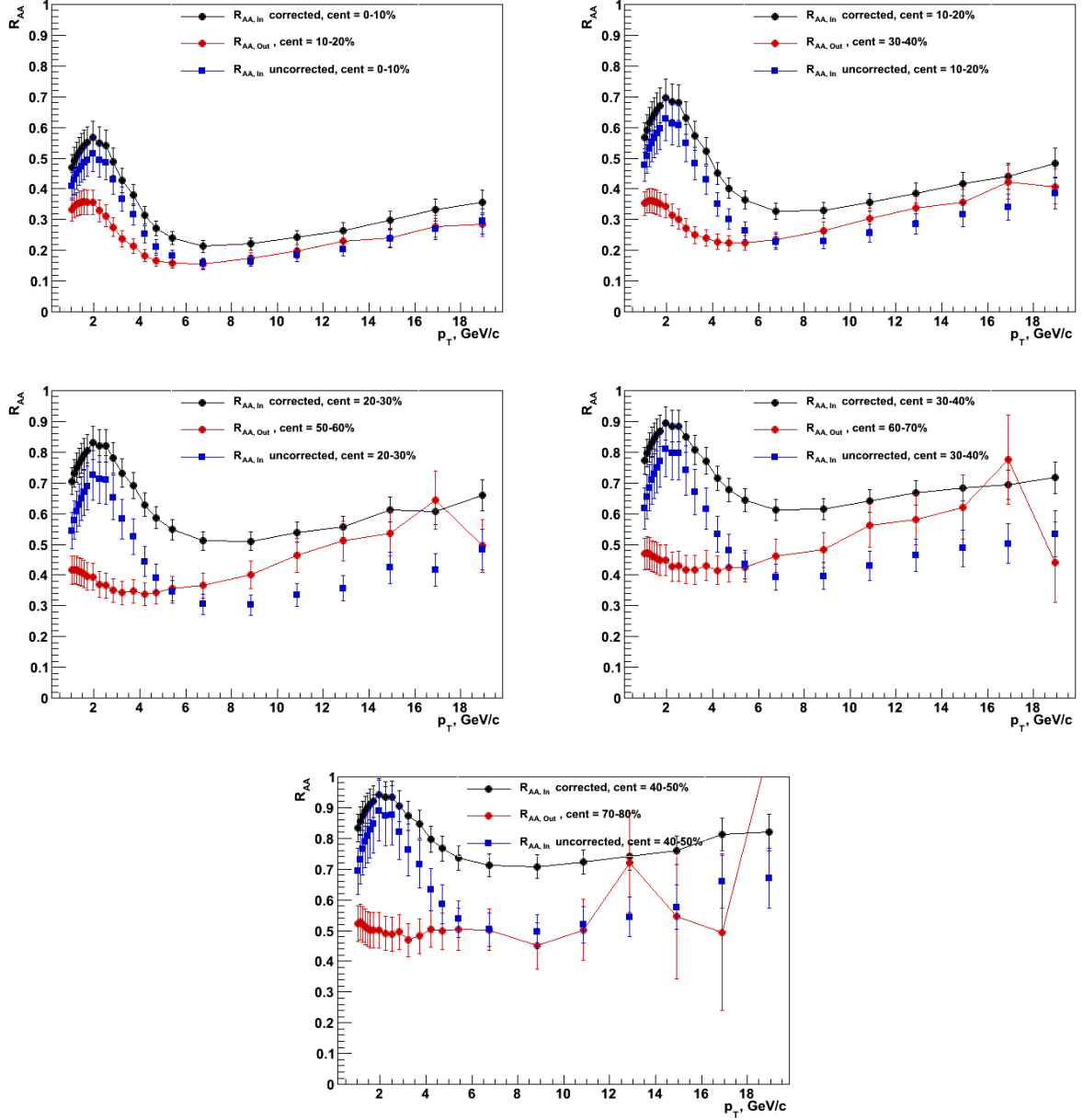


Figure 34: $R_{AA,in}$ and $R_{AA,out}$ vs. p_T for centrality sets, where $L_{in}^{low} \approx L_{out}^{high}$. Both density-corrected (black) and original (blue) $R_{AA,in}$ are shown. Gluon density n_g ($\kappa = \frac{3}{4}$) is assumed to be the proper scattering density.

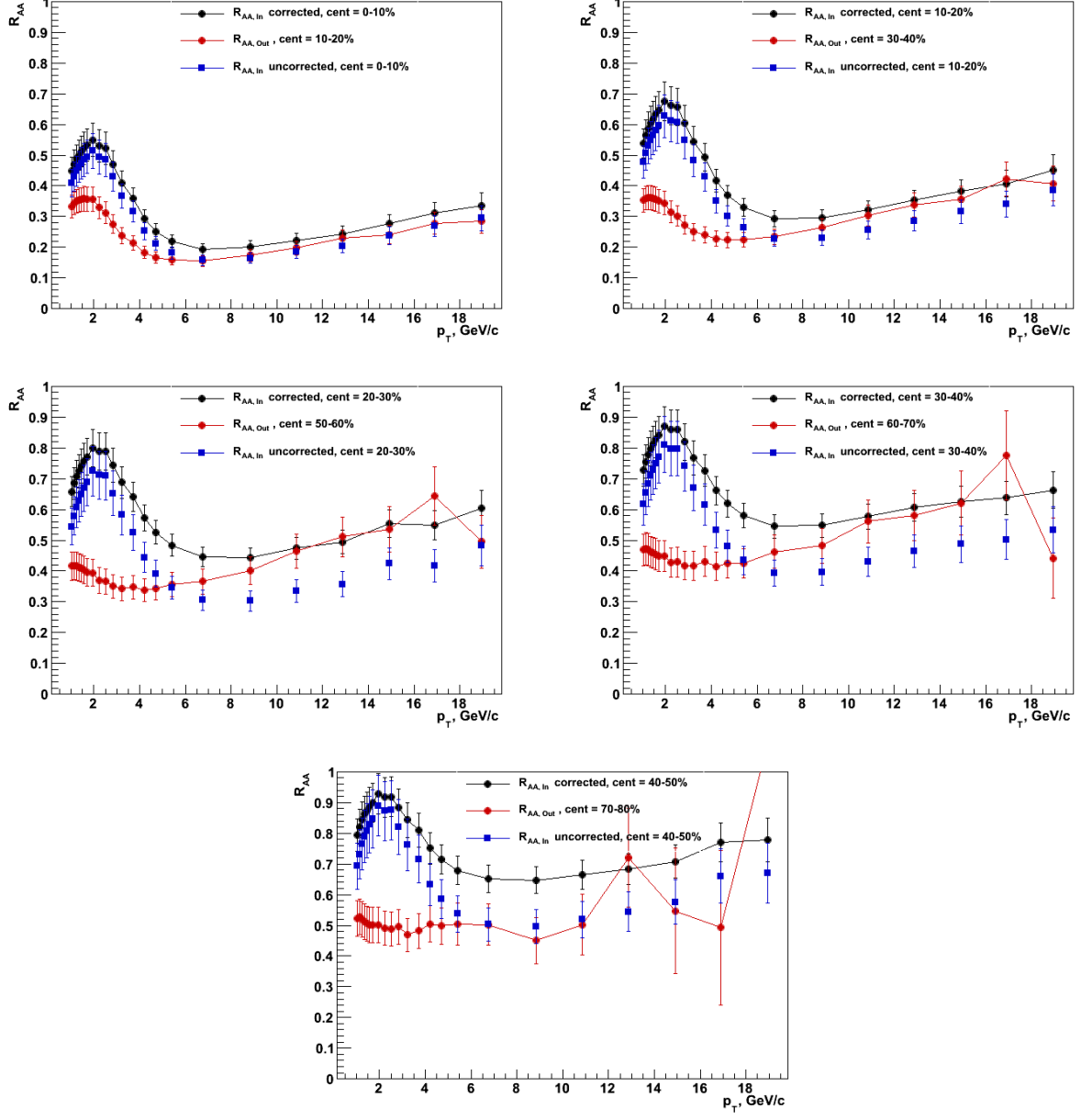


Figure 35: $R_{AA,in}$ and $R_{AA,out}$ vs. p_T for centrality sets, where $L_{in}^{low} \approx L_{out}^{high}$. Both density-corrected (black) and original (blue) $R_{AA,in}$ are shown. Scattering center density is assumed to be $\rho \propto \epsilon^{\frac{1}{2}}$.

Density ratios for PbPb and AuAu collisions

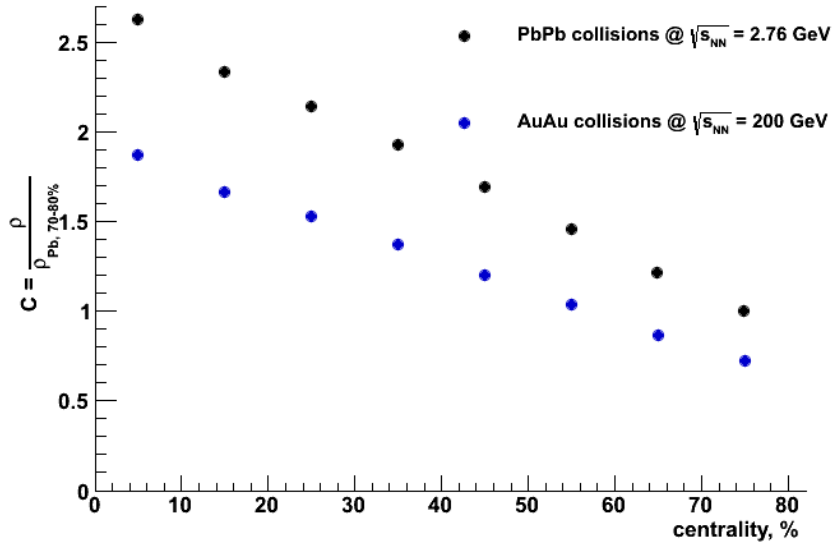


Figure 36: Relative scattering center density ratio for PbPb and AuAu collisions

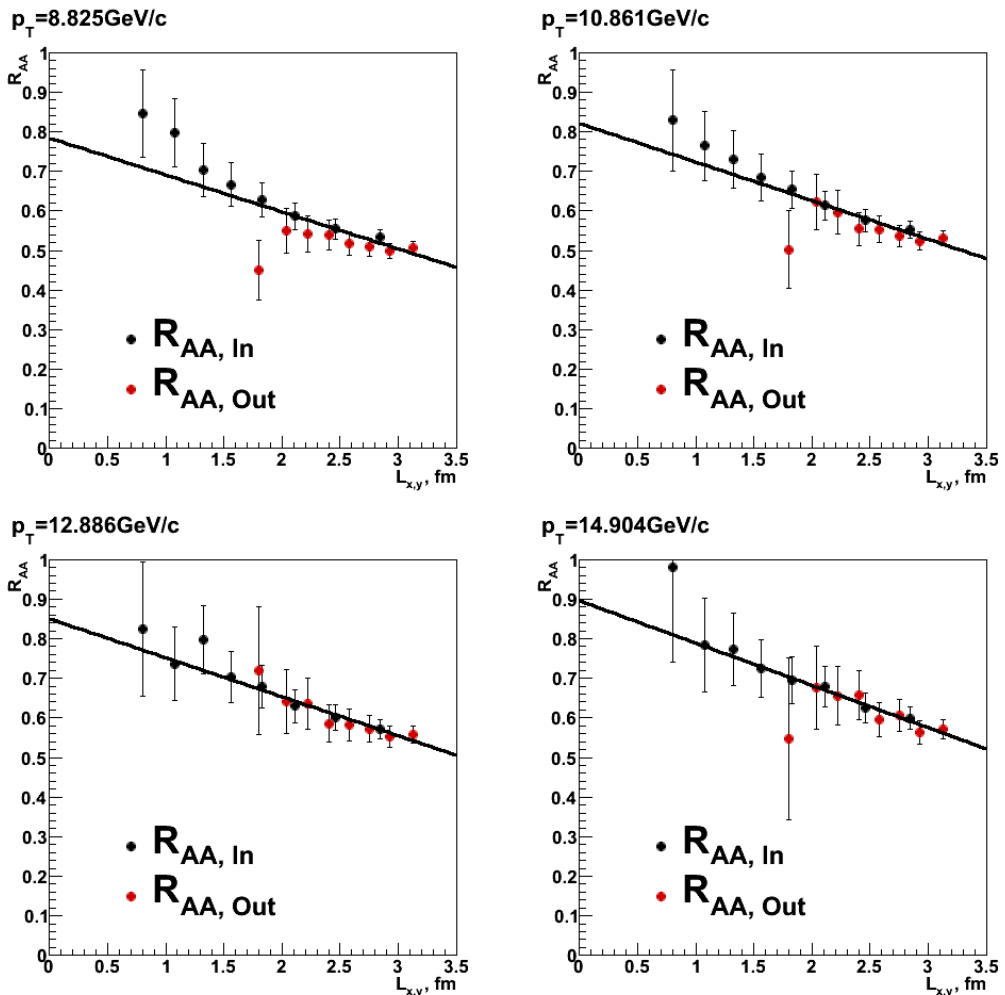


Figure 37: Scaled $R_{AA,in/out}$ vs. $L_{in/out}$ for several p_T bins. Solid black line is a linear fit to the data.

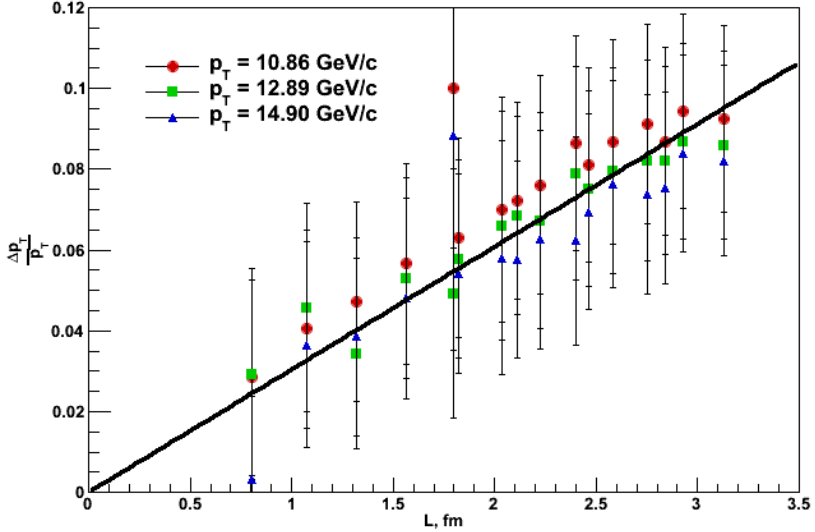


Figure 38: Relative radiative energy losses vs characteristic lengths for several p_T bins, scaled to density $\rho_{70\%-80\%}$. Solid black line shows a linear fit to the data.

Continuing, eq. 65 is used to calculate the relative radiative energy losses, see fig. 38. One can observe a linear $\frac{\Delta p_T}{p_T}(L)$ dependence, as opposed to the QCD prediction, L^2 (eq. 27). Furthermore, the linear fit $\frac{\Delta p_T}{p_T}(L=0) \approx 0$, which is very appealing. Moreover, one can check how this plot would look like if the QCD result was used instead. The relative energy losses with $\kappa = \frac{3}{4}$ for $p_T \approx 10.86 \text{ GeV}/c$ vs. L_{in} and L_{out} are given in fig. 39. In- and out-of-plane points are plotted explicitly to show a clear distinction of energy loss of a parton traveling in two directions. Such an angular dependence is physically reasonable only if the presence of flow is assumed; however, as discussed above, for $p_T \gtrsim 10 \text{ GeV}/c$ one would expect flow effects to be negligible if any.

Next, using the energy loss fit and eq. 70, the expected $R_{AA,in/out}$ for PbPb collisions is calculated and compared with the measured ones, see fig. 40.

Eventually, an attempt is made to rescale the calculations from PbPb to AuAu system colliding at $\sqrt{s_{NN}} = 200 \text{ GeV}$. Calculated $R_{AA,in/out}$ with comparison to the measured PHENIX data [43] are shown in the upper panel of fig. 41. A very good agreement between the measured and calculated data is found. Note that from equations 14 and 15, the calculation of $R_{AA,in}$ and $R_{AA,out}$ is equivalent to the calculation of R_{AA} and v_2 as long as higher orders of flow $v_{k>2}$ are neglected. Calculated R_{AA} with comparison to the measurement results are given in the lower panel of fig. 41.

Finally, the first steps of our analysis are re-traced. From eq. 70 one can see that R_{AA} scales with variable $Cf(L)$, where $f(L)$ is the energy loss curve. A proper matter-energy density relation was found to be $\rho \propto \epsilon^{\frac{1}{2}}$, and a linear radiative energy loss dependence on L was observed. The observed $R_{AA,in/out}$ scaling variable is then simply

$$\rho L = K_1 \epsilon^{\frac{1}{2}} L = K_2 \left(\frac{1}{L_{in} L_{out}} \frac{dN_{ch}}{d\eta} \right)^{\frac{1}{2}} L \quad (73)$$

where K_i are some proportionality constants, for simplicity set to $K_2 = 1$. This means that if there were two centrality bins with $(\rho L_{in})_c \approx (\rho L_{out})_p$, the measured $R_{AA,in}^c$ should be very similar to

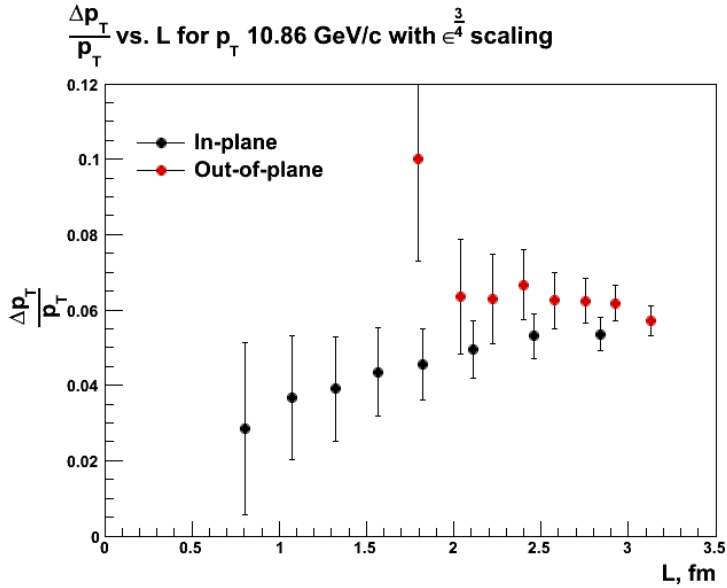


Figure 39: Relative radiative energy losses versus L_{in} and L_{out} for $p_T \approx 10.86\text{GeV}/c$ bin.

the measured $R_{AA,out}^p$. To check this, once again $\rho L_{in/out}$ is plotted versus centrality bins for PbPb, looking for sets with similar density-weighted characteristic lengths. Four sets are found, see fig. 42, for which $R_{AA,in}^c \approx R_{AA,out}^p$ is expected. The comparison of $R_{AA,in/out}$ for these centralities is shown in fig. 43.

For convenience, in fig. 44 the *unscaled* relative energy loss is plotted versus the scaling variable ρL , using the measured AuAu $R_{AA,in/out}$ to calculate $\left(\frac{\Delta p_T}{p_T}\right)_{AuAu}$. Seeing all the points falling onto one curve, one would also expect the measured R_{AA} to scale as ρL . However, from fig. 45 one can see that AuAu $R_{AA,in/out}$ are underestimated w.r.t. PbPb system. Is it possible to understand what happens?

If the scaling works, using eq. 64 one can write:

$$R_{AA,LHC} = (1 - aL)^{-\chi_{LHC}} \quad (74a)$$

$$R_{AA,RHIC} = (1 - aL)^{-\chi_{RHIC}} \quad (74b)$$

The powers χ_{LHC} and χ_{RHIC} obtained from invariant particle yield in pp collisions are not the same, hence, $R_{AA,LHC}$ and $R_{AA,RHIC}$ comparison is not equivalent. To get a proper comparison, different powers have to be accounted for, e.g.:

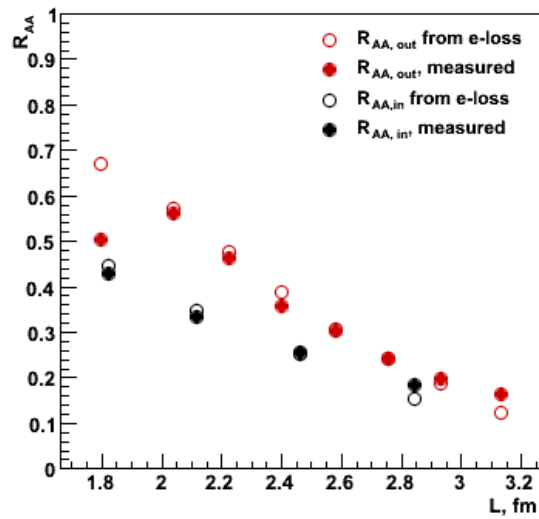
$$R_{AA,RHIC} \Rightarrow R_{AA,RHIC}^{\frac{\chi_{LHC}}{\chi_{RHIC}}} \quad (75)$$

Measured $R_{AA,in/out}$ for PbPb and $R_{AA,in/out}^\Lambda$ (with $\Lambda = \chi_{LHC}/\chi_{RHIC}$) for AuAu systems versus scaling variable ρL is plotted in fig. 46. Finding a very nice scaling, a fit is attempted:

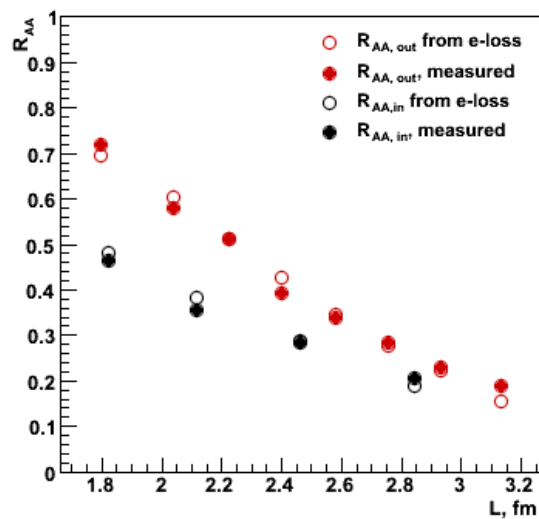
$$R_{AA} = (1 - ax)^{-\chi_{LHC}} \quad (76)$$

where $x = \epsilon^{\frac{1}{2}} L$ is the scaling variable, $\chi_{LHC} = -6.54$ is the power from pp invariant particle yield parametrization [41] and a is the proportionality constant – the only free parameter, accounting for energy loss and matter-energy density proportionality constants.

R_{AA} vs. L , $p_T = 10.861 \text{ GeV}/c$



R_{AA} vs. L , $p_T = 12.886 \text{ GeV}/c$



R_{AA} vs. L , $p_T = 14.904 \text{ GeV}/c$

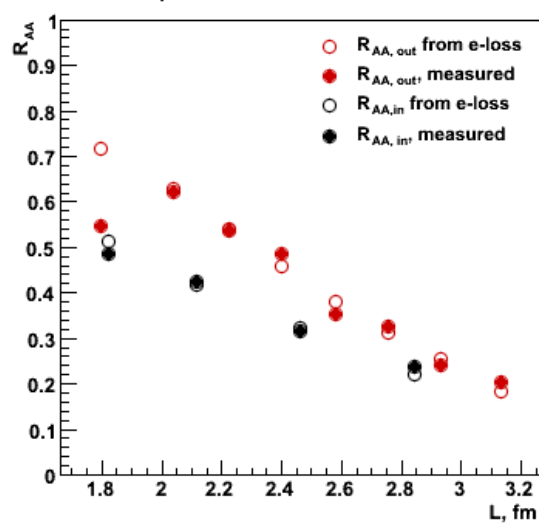
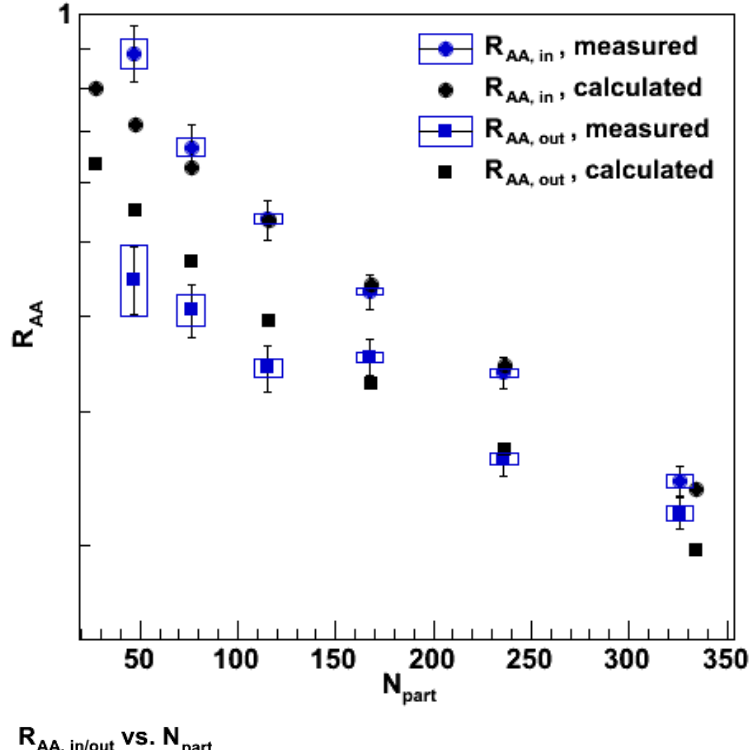


Figure 40: PbPb $R_{AA,in/out}$ calculated from e-loss fit (empty points) with comparison to the measured ones (solid points)

R_{AA} comparison



$R_{AA, in/out}$ vs. N_{part}

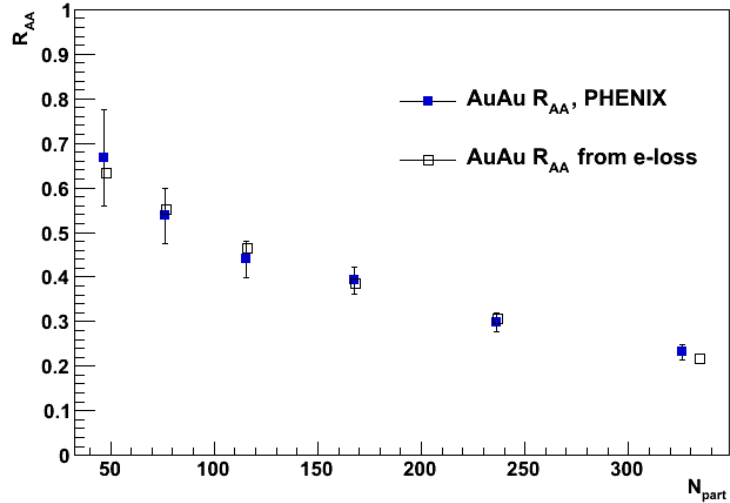


Figure 41: Calculated $R_{AA,in/out}$ for AuAu at $\sqrt{s} = 200\text{GeV}$ collisions with comparison to the measured ones by PHENIX (upper plot); calculated R_{AA} with comparison to the measured data for the same system [43]

$\sqrt{\epsilon}L$ vs cent.

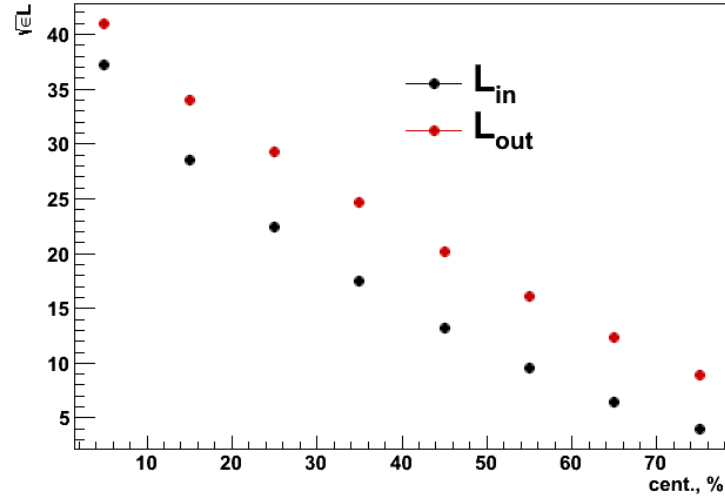


Figure 42: Density-weighted characteristic lengths vs. centrality. Density follows proportionality $\rho \propto \epsilon^{\frac{1}{2}}$.

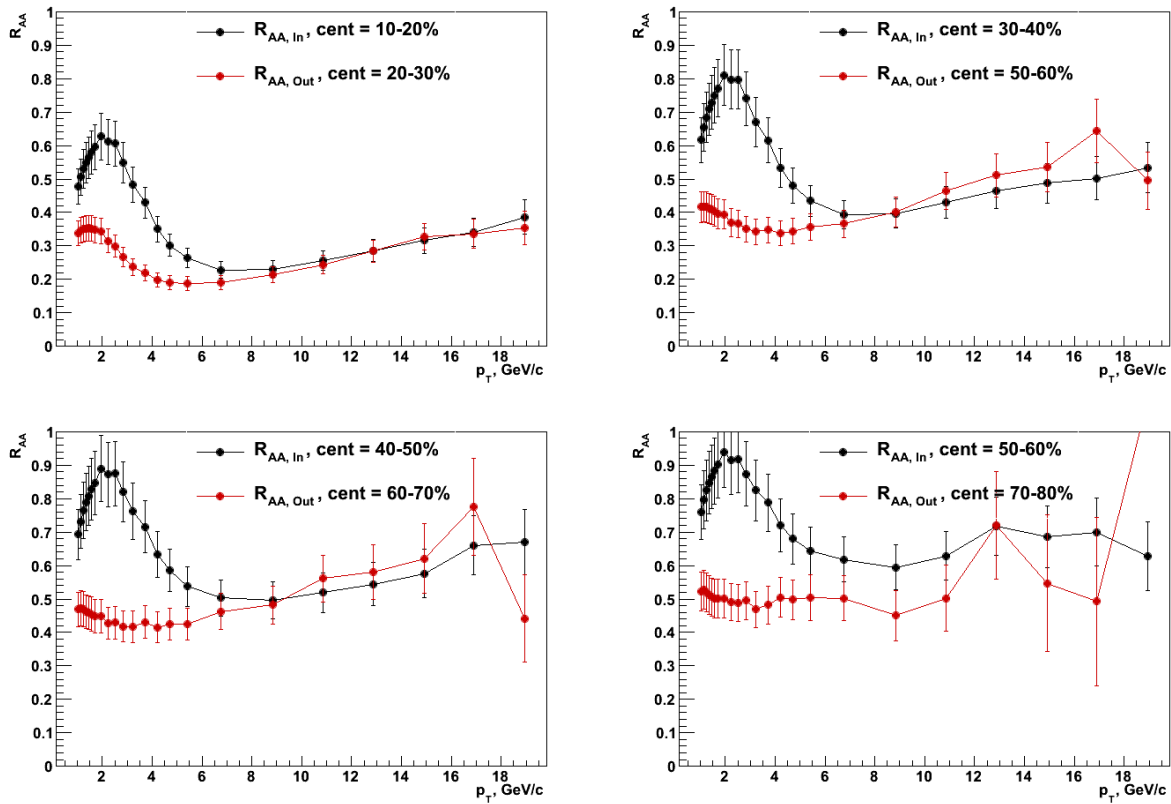


Figure 43: $R_{AA,in}^c$ and $R_{AA,out}^p$ comparison for centrality bin sets, where $(\rho L_{in})^c \approx (\rho L_{out})^p$ (PbPb collisions).

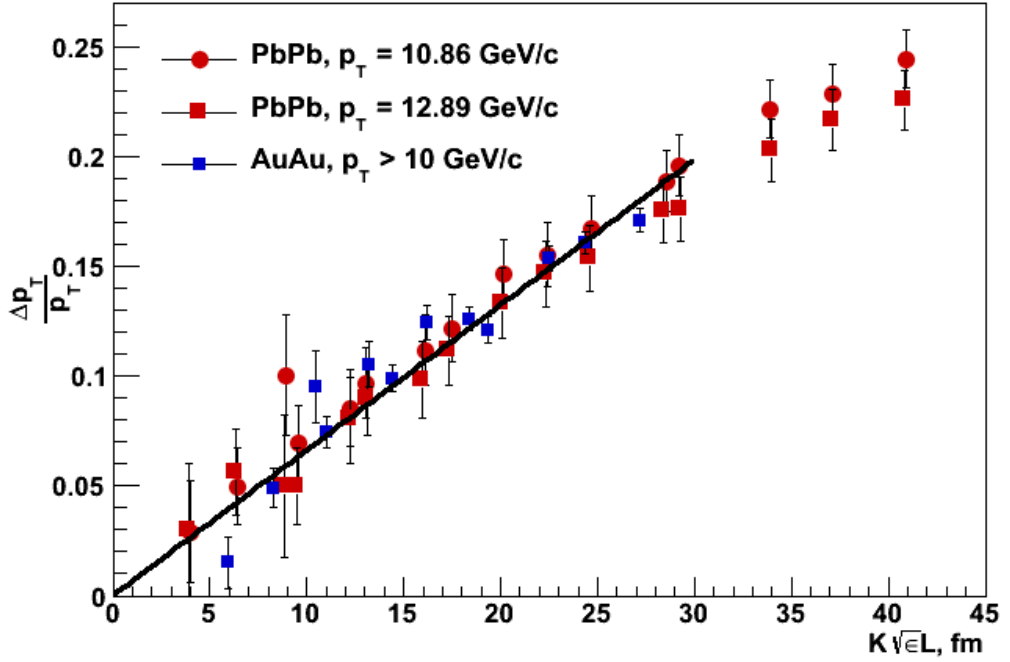


Figure 44: Relative radiative energy losses for AuAu and PbPb systems versus the scaling variable, $K\sqrt{\epsilon}L$. K is a proportionality constant, such that $K\sqrt{\epsilon}$ is dimensionless.

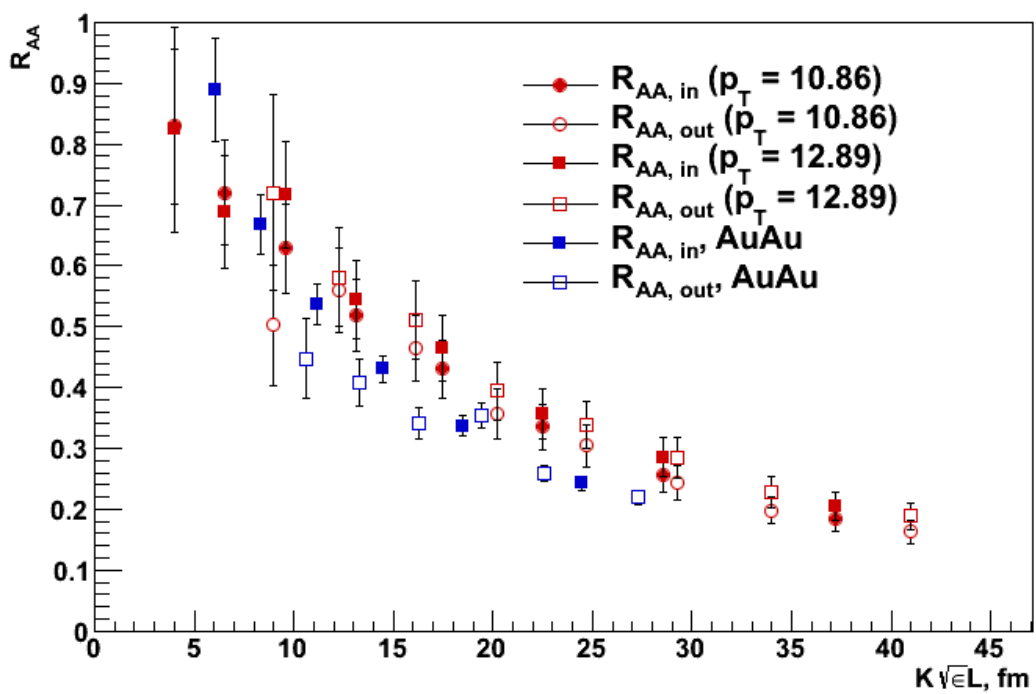


Figure 45: Measured $R_{AA,in/out}$ for PbPb and AuAu systems vs. $K\sqrt{\epsilon}L$. K is a proportionality constant, such that $K\sqrt{\epsilon}$ is dimensionless.

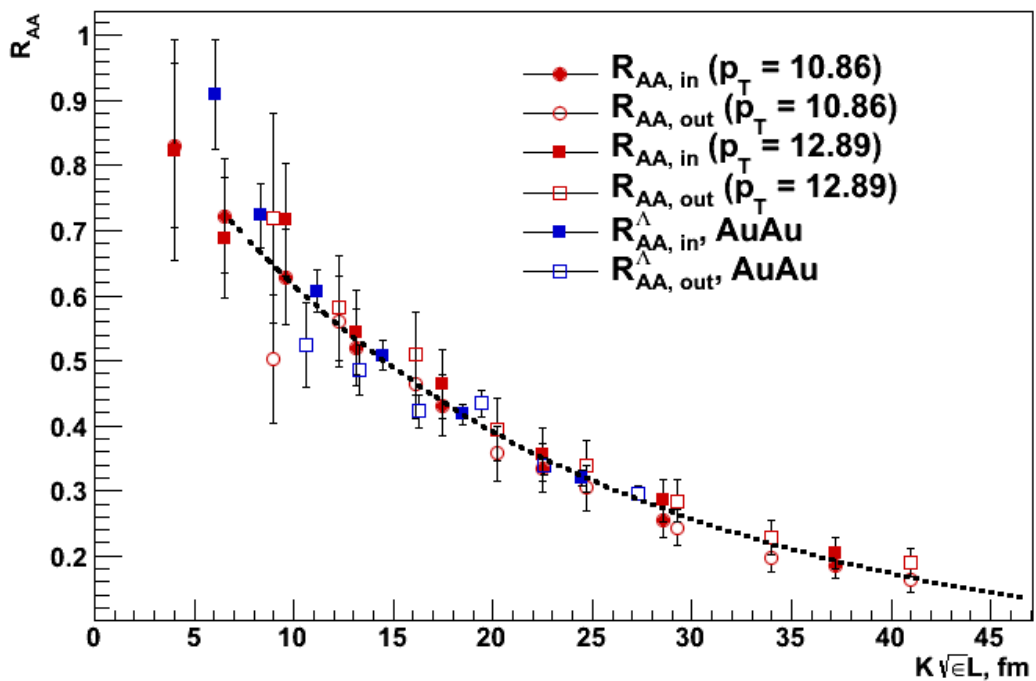


Figure 46: Measured $R_{AA,in/out}$ for PbPb and AuAu systems vs. $K\sqrt{\epsilon}L$, where K is a proportionality constant, such that $K\sqrt{\epsilon}$ is dimensionless. The black dashed line shows a fit of eq. 70 with $\chi = -6.54$ obtained from parametrizing the invariant charged particle yield in pp collisions at $\sqrt{s} = 2.76\text{GeV}$ [41].

8 Discussion

Comparing in- and out-of-plane nuclear modification factors for collisions having similar participant distribution profiles one finds a significant QCD matter density effect for the observables R_{AA} and v_2 . Assuming the gluon density n_g to be dominant in QGP, an attempt to scale down $R_{AA,in}$ to the density of $R_{AA,out}$ results in an overestimation of $R_{AA,in}$. This suggests that either the contribution of n_g to radiative energy loss is overestimated, or that there is a non-negligible contribution of flow that is scaled up.

A "proper" density relation $\rho \propto \epsilon^{\frac{1}{2}}$ has been found, using which it is possible to scale up $R_{AA,in}$ so that it becomes very similar to $R_{AA,out}$. This can be explained in terms of longitudinal expansion: for a central collision, a probe will go further, and thus the density decrease due to the longitudinal medium expansion will be bigger, than in peripheral collision. Hence it seems reasonable to use a lower effective density – as ϵ grows with centrality, one might see the $\sqrt{\epsilon}$ as an effective way to take it into account.

Contrary to the QCD prediction, the radiative energy loss seems to show a linear L dependence, instead of quadratic. In the presented framework, the matter density $\rho \propto \epsilon^{\frac{1}{2}} \propto T^2$, which then, combined with observed L dependence, reads:

$$\Delta E \propto T^2 L \quad (77)$$

Though this is the result that comes purely from this analysis, interestingly enough, the dimension of eq. 77 is the same as in eq. 27.

Having parametrized the energy loss curve, an attempt has been made to evaluate the expected values for quantities $R_{AA,in/out}$ (recall from equations 14 and 15, that the calculation of quantities $R_{AA,in/out}$ is equivalent to the calculation of R_{AA} and v_2). The calculations were successfully rescaled to AuAu system colliding at $\sqrt{s} = 200\text{GeV}$ – the obtained values agree with the measured data very well.

Considering the linear length-energy loss dependence and the new matter-energy density relation, the density-weighted characteristic lengths $\rho L \propto \left(\frac{1}{L_{in}L_{out}} \frac{dN_{ch}}{d\eta}\right)^{\frac{1}{2}} L$ were used to compare $R_{AA,in/out}$ for both AuAu and PbPb cases. This is a very solid check, as the *measured* R_{AA} is used – in this way all the possible sources of errors that might have been introduced by the simplifying assumptions are avoided. It is found that $R_{AA,in/out}$ can be parametrized as a function of $\rho L_{in/out}$ independently of the colliding system. An agreement of eq. 70 fit with the data shows a lot of support for this picture. This is a very appealing result, as it enables one to calculate both the nuclear modification factor and the asymmetry parameter v_2 using very few (measured) input parameters: inelastic pp scattering cross-section, invariant charged particle yield in pp collisions and charged particle yield $\frac{dN_{ch}}{d\eta}$ for heavy ion collisions of interest.

9 Conclusions

An attempt has been made to do a simple, model-independent analysis of data, trying to understand if there is an easy way of characterizing the nuclear modification factor R_{AA} and asymmetry coefficient v_2 .

Using a Glauber MC, mean free paths for partons created in PbPb collisions were extracted for 10% centrality bins from 0% up to 80%. By comparing 5 sets of centrality bins, where the participant profile in-plane (for more central collision) has a similar shape as the out-plane participant profile (for more peripheral collision), it was found that there is a distinct density effect: for more central collisions, higher density results in enhanced energy loss, which, in turn, reduces R_{AA} .

It is therefore necessary to account for different gluon densities. It was found that normalizing all the densities to that of 70%-80% centrality bin leads to an overestimation of R_{AA} , which could possibly be caused by the effects of the flow. Moreover, a proper matter–energy density relation was evaluated, which accounts for both density and flow effects and thus provides a transition from expanding to a stationary medium.

A naive picture is then used to estimate radiative energy loss for partons probing this medium. The resulting $\frac{dp_T}{p_T} = f(L)$ dependence is linear, and its dimension agrees with the QCD expectation.

Using the energy loss fit, the expected characteristics, R_{AA} and v_2 , were re-evaluated for PbPb collisions. They were found to be in a good agreement with the measured quantities.

Finally, using the obtained energy loss curve from LHC data, the calculations were rescaled to a AuAu system colliding at $\sqrt{s} = 200\text{GeV}/c$. The expected values observables, R_{AA} and v_2 , were successfully calculated, hence showing that it is possible to have these quantities parametrized by one universal relation, $\epsilon^{\frac{1}{2}}L$.

References

- [1] T. Renk, Phys. Rev. C **85** (2012) 044903 [arXiv:1112.2503 [hep-ph]].
- [2] <http://www.fnal.gov/pub/inquiring/matter/madeof/> (Last checked 17th May, 2013).
- [3] *Solar Energy Generation Theory Being Tested in Brookhaven Neutrino Experiment*, News from Brookhaven National Laboratory, 14 September, 1967.
- [4] [http://en.wikipedia.org/wiki/Chirality_\(physics\)](http://en.wikipedia.org/wiki/Chirality_(physics)) (Last checked 17th May, 2013).
- [5] http://en.wikipedia.org/wiki/Current_quark_mass (Last checked 4th June, 2013).
- [6] http://en.wikipedia.org/wiki/Constituent_quark (Last checked 4th June, 2013).
- [7] Gordon Kane, *Modern Elementary Particle Physics: the Fundamental Particles and Forces?* – Updated edition, ISBN 0-201-62460-5, (2009).
- [8] G. Aad *et al.* [ATLAS Collaboration], Phys. Lett. B **716** (2012) 1 [arXiv:1207.7214 [hep-ex]].
- [9] P. Skands, arXiv:1207.2389 [hep-ph].
- [10] B.R Martin and G. Shaw, *Particle Physics. Third edition*, ISBN 978-0-470-03293-0, (2008).
- [11] <http://ps-div.web.cern.ch/ps-div/PSComplex/CERNAcc.html> (Last checked 10 June, 2013)
- [12] ATLAS Collaboration, JINST, vol 3 (2008), p. S08003.
- [13] G. Aad *et al.* [ATLAS Collaboration], Phys. Lett. B **707** (2012) 330 [arXiv:1108.6018 [hep-ex]].
- [14] <http://en.wikipedia.org/wiki/Pseudorapidity> (Last checked 17 May, 2013).
- [15] Alexandru Florin Dobrin, Doctors dissertation: *R-hadron Searches and Charged Pion Spectra at High Transverse Momentum in Proton-Proton Collisions at the LHC using the ALICE Detector*, (October 2010).
- [16] Tuva Richert, Master's Thesis: *K_s^0 , Λ , and $\bar{\Lambda}$ p_T spectra in pp collisions at $\sqrt{s} = 7$ TeV, measured with ALICE experiment at LHC*, (August 2011).
- [17] <http://aliceinfo.cern.ch/Public/en/Chapter2/Chap2Experiment-en.html> (Last checked 17 May, 2013).
- [18] http://en.wikipedia.org/wiki/Plum_pudding_model (Last checked 17 May, 2013).
- [19] http://en.wikipedia.org/wiki/Relativistic_nuclear_collisions (Last checked 11 June, 2013).
- [20] http://en.wikipedia.org/wiki/Neutron_star (Last checked 17 May, 2013).
- [21] D. d'Enterria, "Jet quenching", arXiv:0902.2011 [nucl-ex].
- [22] J. Gosset *et al.*, Phys. Rev. C bf 16 (1977), p. 629-657

- [23] S. Nagamiya *et al.*, Phys. Rev. C **24** (1981), p. 971-1003.
- [24] H. A. Gustafsson *et al.*, Phys. Rev. Lett. **52** (1984), p. 1590-1593.
- [25] Wojciech Florkowski, *Phenomenology of Ultra-Relativistic Heavy-Ion Collisions*, ISBN-13 978-981-4280-66-2 (2010).
- [26] P. Bozek and I. Wyskiel, Phys. Rev. C **81** (2010) 054902 [arXiv:1002.4999 [nucl-th]].
- [27] B. Alver and G. Roland, Phys. Rev. C **81** (2010) 054905 [Erratum-ibid. C **82** (2010) 039903] [arXiv:1003.0194 [nucl-th]].
- [28] P. Christiansen, *The highest man-made temperature*, Institute Colloquium at Fysicum in Lund (2012)
- [29] P. Gros, Doctorss dissertation: *Identifying charged hadrons on the relativistic rise using the ALICE TPC at LHC*, (June 2011).
- [30] A. Peshier, Phys. Rev. Lett. **97**, 212301 (2006).
- [31] R. K. Ellis, W. J. Stirling and B. R. Webber, *QCD and collider physics*, Camb. Monogr. Part. Phys. Nucl. Phys. Cosmol. 8, 1 (1996).
- [32] Yuri L. Dokshitzer, *Basics of Colour Dynamics and QCD Parton Evolution*, Universit Paris-VI, Paris (2001).
- [33] S. Peigne and A. V. Smilga, Phys. Usp. **52** (2009) 659 [Usp. Fiz. Nauk **179** (2009) 697] [arXiv:0810.5702 [hep-ph]].
- [34] K. Zapp, G. Ingelman, J. Rathsman and J. Stachel, Phys. Lett. B **637** (2006) 179 [hep-ph/0512300].
- [35] J. D. Bjorken, FERMILAB-PUB-82-059-T (1982).
- [36] Stphane Peign, Andr Peshier, Phys. Rev. D **77**, 114017 (2008).
- [37] J. D. Bjorken, Phys. Rev. D **27** (1983), p. 140-151.
- [38] M. L. Miller, K. Reygers, S. J. Sanders and P. Steinberg, Ann. Rev. Nucl. Part. Sci. **57** (2007) 205 [nucl-ex/0701025].
- [39] <https://twiki.cern.ch/twiki/bin/view/Main/LHCGlauberBaseline> (Last checked 17 May, 2013).
- [40] B. Abelev *et al.* [ALICE Collaboration], Phys. Lett. B **720** (2013) 52 [arXiv:1208.2711 [hep-ex]].
- [41] S. Chatrchyan *et al.* [CMS Collaboration], Eur. Phys. J. C **72** (2012) 1945 [arXiv:1202.2554 [nucl-ex]].
- [42] A. Adare *et al.* [PHENIX Collaboration], Phys. Rev. D **76** (2007) 051106 [arXiv:0704.3599 [hep-ex]].

- [43] A. Adare *et al.* [PHENIX Collaboration], Phys. Rev. Lett. **105**, 142301 (2010).
- [44] B. Alver, M. Baker, C. Loizides and P. Steinberg, [arXiv:0805.4411 [nucl-ex]].
- [45] K. Aamodt *et al.* [ALICE Collaboration], Phys. Rev. Lett. **106** (2011) 032301 [arXiv:1012.1657 [nucl-ex]].
- [46] D. G. d'Enterria, [arXiv:nucl-ex/0302016].
- [47] K. Reygers, *Glauber Monte-Carlo Calculations for Au+Au Collisions at $\sqrt{s_{NN}} = 200\text{GeV}$* (February 2003).
- [48] T. Renk, H. Holopainen, U. Heinz and C. Shen, Phys. Rev. C **83** (2011) 014910 [arXiv:1010.1635 [hep-ph]].

A Summary of Terms and Acronyms

AA – Short for a general nucleus-nucleus system

ALICE – A Large Heavy Ion Experiment

ATLAS – A Toroidal LHC Apparatus

CMS – Compact Muon Solenoid

FCal – Forward Calorimeter

FMD – Forward Multiplicity Detector

ID - Inner Detector

IROC – Inner Read-out Chamber

ITS – Inner Tracking System

LHC – Large Hadron Collider

LHCb – LHC Beauty Experiment

MWPC – Multiwire Projection Chamber

OROC – Outer Read-out Chamber

PID – Particle Identification

(p)QCD – Perturbative Quantum Chromodynamics

QGP – Quark Gluon Plasma

R_{AA} – Nuclear Modification Factor

RHIC – Relativistic Heavy Ion Collider

RP – Reaction Plane

SCT – Semiconductor Microstrip Tracker

SM – Standard Model

SPD – Silicon Pixel Detector

TPC – Time Projection Chamber

v_2 – Elliptic flow/assymetry coefficient

ZDC – Zero Degree Calorimeter

B Impact parameter, $\langle N_{part} \rangle$ and $\langle N_{bin} \rangle$ results from the Glauber Monte Carlo simulation

Table 8: Impact parameter, $\langle N_{part} \rangle$ and $\langle N_{bin} \rangle$ results from Glauber Monte Carlo for PbPb collisions at $\sqrt{s_{NN}} = 2.76\text{TeV}$

Centrality	Impact parameter, fm	$\langle N_{part} \rangle$	$\langle N_{bin} \rangle$
0% - 10%	0 - 4.93	362.7	1507.5
10% - 20%	4.93 - 6.99	262.7	922.2
20% - 30%	6.99 - 8.54	187.9	562.1
30% - 40%	8.54 - 9.87	130.6	324.4
40% - 50%	9.87 - 11.03	86.8	174.5
50% - 60%	11.03 - 12.06	54.3	86.1
60% - 70%	12.06 - 13.04	31.3	39.6
70% - 80%	13.04 - 13.96	16.2	16.1

Table 9: Impact parameter, $\langle N_{part} \rangle$ and $\langle N_{bin} \rangle$ results from Glauber Monte Carlo for AuAu collisions at $\sqrt{s_{NN}} = 200\text{GeV}$

Centrality	Impact parameter, fm	$\langle N_{part} \rangle$	$\langle N_{bin} \rangle$
0% - 10%	0.01 - 4.65	334.2	967.1
10% - 20%	4.65 - 6.60	236.9	602.5
20% - 30%	6.60 - 8.08	168.1	374.6
30% - 40%	8.08 - 9.32	116.1	222.0
40% - 50%	9.32 - 10.41	76.7	122.9
50% - 60%	10.41 - 11.42	47.8	62.9
60% - 70%	11.42 - 12.31	27.6	29.7
70% - 80%	12.31 - 13.18	14.5	12.8

C p_T and R_{AA} data used in analysis

Table 10: Measured $p_{T,ATLAS}$, $v_{2,ATLAS}$, $R_{AA,ALICE}$ and calculated $R_{AA,in}$ and $R_{AA,out}$ for 0% - 10% centrality bin

$p_{T,ATLAS}$, GeV/c	$v_{2,ATLAS}$	$R_{AA,ALICE}$	$R_{AA,in}$	$R_{AA,out}$
1.05	0.047	0.374	0.409 ± 0.045	0.338 ± 0.037
1.15	0.051	0.391	0.431 ± 0.047	0.352 ± 0.038
1.25	0.054	0.404	0.448 ± 0.049	0.360 ± 0.039
1.35	0.057	0.414	0.461 ± 0.051	0.367 ± 0.040
1.45	0.060	0.423	0.473 ± 0.052	0.372 ± 0.041
1.55	0.063	0.431	0.484 ± 0.054	0.377 ± 0.042
1.69	0.066	0.437	0.495 ± 0.055	0.379 ± 0.042
1.93	0.072	0.448	0.513 ± 0.057	0.383 ± 0.043
2.23	0.079	0.426	0.493 ± 0.055	0.358 ± 0.040
2.54	0.085	0.414	0.485 ± 0.054	0.343 ± 0.038
2.84	0.089	0.364	0.429 ± 0.048	0.299 ± 0.033
3.21	0.092	0.310	0.367 ± 0.041	0.253 ± 0.028
3.71	0.091	0.268	0.317 ± 0.035	0.220 ± 0.024
4.22	0.088	0.215	0.253 ± 0.028	0.177 ± 0.019
4.72	0.079	0.183	0.212 ± 0.023	0.154 ± 0.017
5.41	0.067	0.160	0.182 ± 0.020	0.139 ± 0.015
6.75	0.050	0.143	0.157 ± 0.017	0.129 ± 0.014
8.82	0.039	0.153	0.165 ± 0.018	0.141 ± 0.016
10.86	0.032	0.174	0.184 ± 0.021	0.163 ± 0.018
12.89	0.020	0.197	0.205 ± 0.024	0.189 ± 0.022
14.90	0.036	0.221	0.237 ± 0.029	0.205 ± 0.025
16.91	0.027	0.256	0.269 ± 0.035	0.242 ± 0.031
18.93	0.023	0.282	0.294 ± 0.040	0.269 ± 0.037

Table 11: Measured $p_{T,ATLAS}$, $v_{2,ATLAS}$, $R_{AA,ALICE}$ and calculated $R_{AA,in}$ and $R_{AA,out}$ for 10% - 20% centrality bin

$p_{T,ATLAS}$, GeV/c	$v_{2,ATLAS}$	$R_{AA,ALICE}$	$R_{AA,in}$	$R_{AA,out}$
1.05	0.089	0.405	0.477 ± 0.052	0.333 ± 0.036
1.15	0.096	0.424	0.505 ± 0.055	0.343 ± 0.037
1.25	0.102	0.440	0.529 ± 0.058	0.350 ± 0.038
1.35	0.108	0.451	0.548 ± 0.060	0.354 ± 0.039
1.45	0.113	0.460	0.564 ± 0.062	0.355 ± 0.039
1.55	0.119	0.469	0.580 ± 0.065	0.358 ± 0.040
1.69	0.126	0.476	0.595 ± 0.066	0.356 ± 0.040
1.93	0.137	0.492	0.627 ± 0.070	0.357 ± 0.040
2.23	0.150	0.470	0.611 ± 0.068	0.329 ± 0.037
2.54	0.160	0.460	0.606 ± 0.067	0.313 ± 0.035
2.84	0.167	0.412	0.550 ± 0.061	0.275 ± 0.030
3.21	0.171	0.360	0.483 ± 0.053	0.237 ± 0.026
3.72	0.168	0.321	0.429 ± 0.047	0.213 ± 0.023
4.22	0.157	0.267	0.351 ± 0.038	0.183 ± 0.020
4.72	0.144	0.234	0.302 ± 0.033	0.167 ± 0.018
5.41	0.123	0.211	0.263 ± 0.029	0.159 ± 0.017
6.75	0.094	0.191	0.227 ± 0.025	0.155 ± 0.017
8.82	0.070	0.202	0.230 ± 0.025	0.174 ± 0.019
10.85	0.064	0.226	0.255 ± 0.028	0.198 ± 0.022
12.88	0.055	0.257	0.285 ± 0.033	0.229 ± 0.026
14.89	0.067	0.278	0.316 ± 0.038	0.241 ± 0.029
16.91	0.051	0.309	0.340 ± 0.043	0.278 ± 0.036
18.91	0.076	0.335	0.386 ± 0.052	0.284 ± 0.039

Table 12: Measured $p_{T,ATLAS}$, $v_{2,ATLAS}$, $R_{AA,ALICE}$ and calculated $R_{AA,in}$ and $R_{AA,out}$ for 20% - 30% centrality bin

$p_{T,ATLAS}$, GeV/c	$v_{2,ATLAS}$	$R_{AA,ALICE}$	$R_{AA,in}$	$R_{AA,out}$
1.05	0.117	0.441	0.545 ± 0.059	0.338 ± 0.037
1.15	0.126	0.463	0.579 ± 0.063	0.346 ± 0.038
1.25	0.134	0.478	0.606 ± 0.066	0.350 ± 0.038
1.35	0.141	0.490	0.629 ± 0.069	0.352 ± 0.039
1.45	0.148	0.501	0.649 ± 0.071	0.352 ± 0.039
1.55	0.155	0.511	0.669 ± 0.075	0.352 ± 0.039
1.69	0.164	0.517	0.688 ± 0.077	0.347 ± 0.039
1.93	0.178	0.534	0.725 ± 0.081	0.344 ± 0.038
2.24	0.193	0.513	0.711 ± 0.079	0.315 ± 0.035
2.54	0.203	0.505	0.710 ± 0.079	0.300 ± 0.033
2.84	0.210	0.460	0.653 ± 0.072	0.267 ± 0.030
3.21	0.211	0.409	0.582 ± 0.064	0.236 ± 0.026
3.72	0.205	0.372	0.525 ± 0.058	0.219 ± 0.024
4.22	0.191	0.321	0.444 ± 0.048	0.198 ± 0.022
4.72	0.174	0.290	0.391 ± 0.043	0.189 ± 0.021
5.41	0.149	0.266	0.346 ± 0.038	0.187 ± 0.020
6.75	0.117	0.247	0.305 ± 0.033	0.189 ± 0.021
8.82	0.085	0.258	0.303 ± 0.033	0.214 ± 0.024
10.86	0.079	0.289	0.335 ± 0.037	0.243 ± 0.027
12.88	0.056	0.321	0.356 ± 0.041	0.285 ± 0.033
14.89	0.065	0.375	0.424 ± 0.051	0.327 ± 0.040
16.90	0.054	0.376	0.417 ± 0.053	0.336 ± 0.043
18.92	0.077	0.418	0.483 ± 0.066	0.354 ± 0.049

Table 13: Measured $p_{T,ATLAS}$, $v_{2,ATLAS}$, $R_{AA,ALICE}$ and calculated $R_{AA,in}$ and $R_{AA,out}$ for 30% - 40% centrality bin

$p_{T,ATLAS}$, GeV/c	$v_{2,ATLAS}$	$R_{AA,ALICE}$	$R_{AA,in}$	$R_{AA,out}$
1.05	0.136	0.485	0.616 ± 0.067	0.353 ± 0.038
1.15	0.145	0.507	0.654 ± 0.071	0.360 ± 0.039
1.25	0.154	0.523	0.684 ± 0.075	0.362 ± 0.040
1.35	0.162	0.535	0.709 ± 0.078	0.361 ± 0.040
1.45	0.170	0.544	0.729 ± 0.080	0.359 ± 0.039
1.55	0.178	0.553	0.750 ± 0.084	0.356 ± 0.040
1.69	0.188	0.560	0.771 ± 0.086	0.350 ± 0.039
1.93	0.202	0.578	0.811 ± 0.090	0.344 ± 0.038
2.24	0.216	0.556	0.797 ± 0.088	0.315 ± 0.035
2.54	0.226	0.549	0.797 ± 0.088	0.302 ± 0.033
2.84	0.230	0.507	0.740 ± 0.082	0.273 ± 0.030
3.21	0.229	0.460	0.670 ± 0.074	0.250 ± 0.027
3.72	0.219	0.428	0.615 ± 0.067	0.241 ± 0.026
4.22	0.201	0.380	0.532 ± 0.058	0.227 ± 0.025
4.72	0.182	0.352	0.480 ± 0.052	0.224 ± 0.024
5.42	0.159	0.329	0.434 ± 0.047	0.224 ± 0.024
6.75	0.127	0.314	0.393 ± 0.043	0.234 ± 0.026
8.81	0.100	0.330	0.397 ± 0.044	0.264 ± 0.029
10.85	0.086	0.367	0.430 ± 0.048	0.304 ± 0.034
12.88	0.078	0.401	0.464 ± 0.054	0.338 ± 0.039
14.89	0.079	0.421	0.487 ± 0.060	0.355 ± 0.044
16.91	0.043	0.462	0.502 ± 0.065	0.423 ± 0.055
18.93	0.067	0.471	0.534 ± 0.074	0.408 ± 0.058

Table 14: Measured $p_{T,ATLAS}$, $v_{2,ATLAS}$, $R_{AA,ALICE}$ and calculated $R_{AA,in}$ and $R_{AA,out}$ for 40% - 50% centrality bin

$p_{T,ATLAS}$, GeV/c	$v_{2,ATLAS}$	$R_{AA,ALICE}$	$R_{AA,in}$	$R_{AA,out}$
1.05	0.146	0.537	0.693 ± 0.075	0.380 ± 0.041
1.15	0.155	0.558	0.731 ± 0.080	0.385 ± 0.042
1.25	0.165	0.575	0.765 ± 0.084	0.386 ± 0.042
1.35	0.173	0.587	0.790 ± 0.087	0.384 ± 0.042
1.45	0.181	0.593	0.808 ± 0.089	0.378 ± 0.042
1.55	0.188	0.601	0.828 ± 0.092	0.375 ± 0.042
1.69	0.198	0.606	0.847 ± 0.094	0.366 ± 0.041
1.93	0.211	0.626	0.890 ± 0.099	0.361 ± 0.040
2.24	0.223	0.603	0.872 ± 0.097	0.334 ± 0.037
2.54	0.229	0.600	0.874 ± 0.097	0.325 ± 0.036
2.84	0.231	0.561	0.820 ± 0.091	0.302 ± 0.034
3.22	0.226	0.525	0.762 ± 0.084	0.287 ± 0.032
3.72	0.214	0.502	0.716 ± 0.078	0.287 ± 0.032
4.22	0.198	0.454	0.633 ± 0.069	0.274 ± 0.030
4.73	0.178	0.431	0.585 ± 0.064	0.277 ± 0.030
5.42	0.156	0.409	0.538 ± 0.059	0.281 ± 0.031
6.75	0.125	0.402	0.503 ± 0.055	0.302 ± 0.033
8.81	0.093	0.419	0.496 ± 0.055	0.341 ± 0.038
10.85	0.092	0.438	0.519 ± 0.059	0.357 ± 0.041
12.87	0.080	0.469	0.544 ± 0.065	0.394 ± 0.048
14.90	0.043	0.530	0.576 ± 0.073	0.484 ± 0.062
16.90	0.056	0.593	0.660 ± 0.089	0.526 ± 0.072
18.91	0.049	0.611	0.671 ± 0.098	0.551 ± 0.082

Table 15: Measured $p_{T,ATLAS}$, $v_{2,ATLAS}$, $R_{AA,ALICE}$ and calculated $R_{AA,in}$ and $R_{AA,out}$ for 50% - 60% centrality bin

$p_{T,ATLAS}$, GeV/c	$v_{2,ATLAS}$	$R_{AA,ALICE}$	$R_{AA,in}$	$R_{AA,out}$
1.05	0.146	0.588	0.760 ± 0.083	0.416 ± 0.045
1.15	0.156	0.607	0.796 ± 0.087	0.417 ± 0.046
1.25	0.165	0.620	0.825 ± 0.091	0.416 ± 0.046
1.35	0.173	0.630	0.847 ± 0.093	0.412 ± 0.045
1.45	0.179	0.637	0.866 ± 0.095	0.409 ± 0.045
1.55	0.186	0.644	0.883 ± 0.099	0.404 ± 0.045
1.69	0.195	0.649	0.902 ± 0.101	0.397 ± 0.044
1.93	0.204	0.666	0.938 ± 0.105	0.394 ± 0.044
2.24	0.212	0.642	0.915 ± 0.102	0.369 ± 0.041
2.54	0.215	0.643	0.919 ± 0.102	0.366 ± 0.041
2.84	0.214	0.612	0.874 ± 0.097	0.350 ± 0.039
3.22	0.207	0.584	0.825 ± 0.091	0.342 ± 0.038
3.72	0.194	0.568	0.788 ± 0.087	0.348 ± 0.038
4.22	0.181	0.529	0.721 ± 0.079	0.337 ± 0.037
4.73	0.164	0.512	0.680 ± 0.075	0.344 ± 0.038
5.42	0.144	0.500	0.643 ± 0.071	0.356 ± 0.039
6.75	0.128	0.492	0.619 ± 0.068	0.366 ± 0.041
8.81	0.098	0.497	0.594 ± 0.066	0.400 ± 0.045
10.85	0.075	0.546	0.628 ± 0.072	0.464 ± 0.054
12.87	0.084	0.614	0.717 ± 0.087	0.511 ± 0.064
14.88	0.061	0.610	0.685 ± 0.092	0.535 ± 0.074
16.91	0.021	0.672	0.700 ± 0.102	0.645 ± 0.095
18.92	0.059	0.561	0.627 ± 0.103	0.496 ± 0.086

Table 16: Measured $p_{T,ATLAS}$, $v_{2,ATLAS}$, $R_{AA,ALICE}$ and calculated $R_{AA,in}$ and $R_{AA,out}$ for 60% - 70% centrality bin

$p_{T,ATLAS}$, GeV/c	$v_{2,ATLAS}$	$R_{AA,ALICE}$	$R_{AA,in}$	$R_{AA,out}$
1.05	0.136	0.645	0.821 ± 0.090	0.469 ± 0.051
1.15	0.144	0.664	0.856 ± 0.094	0.472 ± 0.052
1.25	0.151	0.673	0.877 ± 0.097	0.470 ± 0.052
1.35	0.161	0.680	0.899 ± 0.100	0.462 ± 0.051
1.45	0.165	0.686	0.913 ± 0.101	0.459 ± 0.051
1.55	0.171	0.691	0.927 ± 0.104	0.455 ± 0.051
1.69	0.177	0.693	0.937 ± 0.106	0.448 ± 0.051
1.93	0.184	0.710	0.972 ± 0.109	0.448 ± 0.051
2.24	0.189	0.688	0.947 ± 0.106	0.428 ± 0.048
2.54	0.190	0.691	0.953 ± 0.106	0.429 ± 0.048
2.84	0.186	0.666	0.913 ± 0.102	0.418 ± 0.047
3.22	0.179	0.650	0.883 ± 0.098	0.417 ± 0.047
3.72	0.169	0.651	0.870 ± 0.096	0.431 ± 0.048
4.22	0.165	0.620	0.825 ± 0.092	0.416 ± 0.047
4.73	0.151	0.609	0.792 ± 0.088	0.425 ± 0.047
5.42	0.139	0.590	0.753 ± 0.083	0.426 ± 0.047
6.75	0.109	0.592	0.721 ± 0.082	0.463 ± 0.054
8.82	0.112	0.620	0.759 ± 0.087	0.482 ± 0.057
10.84	0.062	0.641	0.721 ± 0.087	0.561 ± 0.070
12.87	0.042	0.635	0.689 ± 0.093	0.581 ± 0.081
14.88	0.045	0.683	0.744 ± 0.118	0.621 ± 0.104
16.90	-0.012	0.757	0.738 ± 0.140	0.776 ± 0.144
18.88	0.181	0.693	0.943 ± 0.189	0.442 ± 0.131

Table 17: Measured $p_{T,ATLAS}$, $v_{2,ATLAS}$, $R_{AA,ALICE}$ and calculated $R_{AA,in}$ and $R_{AA,out}$ for 70% - 80% centrality bin

$p_{T,ATLAS}$, GeV/c	$v_{2,ATLAS}$	$R_{AA,ALICE}$	$R_{AA,in}$	$R_{AA,out}$
1.05	0.118	0.684	0.846 ± 0.093	0.523 ± 0.058
1.15	0.123	0.699	0.872 ± 0.096	0.527 ± 0.058
1.25	0.132	0.706	0.892 ± 0.099	0.519 ± 0.058
1.35	0.140	0.711	0.909 ± 0.101	0.512 ± 0.057
1.45	0.144	0.710	0.915 ± 0.102	0.505 ± 0.057
1.55	0.150	0.715	0.930 ± 0.105	0.501 ± 0.057
1.69	0.150	0.717	0.933 ± 0.105	0.501 ± 0.057
1.94	0.155	0.726	0.951 ± 0.107	0.501 ± 0.057
2.24	0.159	0.718	0.947 ± 0.106	0.490 ± 0.055
2.54	0.165	0.728	0.968 ± 0.109	0.488 ± 0.056
2.84	0.156	0.721	0.946 ± 0.106	0.496 ± 0.056
3.22	0.162	0.692	0.916 ± 0.102	0.468 ± 0.053
3.72	0.156	0.701	0.920 ± 0.104	0.482 ± 0.057
4.22	0.130	0.683	0.861 ± 0.097	0.505 ± 0.059
4.73	0.128	0.669	0.841 ± 0.096	0.498 ± 0.059
5.42	0.126	0.674	0.844 ± 0.102	0.504 ± 0.069
6.75	0.127	0.674	0.845 ± 0.102	0.503 ± 0.068
8.80	0.152	0.648	0.845 ± 0.110	0.450 ± 0.075
10.86	0.123	0.666	0.829 ± 0.127	0.502 ± 0.099
12.86	0.034	0.772	0.824 ± 0.169	0.720 ± 0.161
14.84	0.142	0.763	0.980 ± 0.241	0.547 ± 0.205
16.89	0.134	0.672	0.852 ± 0.278	0.492 ± 0.252
18.94	-0.350	0.643	0.193 ± 0.312	1.093 ± 0.383